Species-specific features of ion channel localization in parvalbumin interneurons in the human and mouse neocortex

Ph.D. dissertation

Emőke Bakos

Supervisors:

Dr. Karri Lamsa

Dr. Viktor Szegedi

Ph.D. School in Biology
Department of Physiology, Anatomy and Neuroscience
Faculty of Science and Informatics
University of Szeged

Hungarian Centre of Excellence for Molecular Medicine

Szeged

2026

CONTENTS

List of abbreviations

AIS	axon initial segment
AHP	afterhyperpolarization
AP	action potential
APLP1	amyloid precursor-like proteins
CM	capacitance
DTXK	dendrotoxin-K
EPSC	excitatory postsynaptic current
EPSP	excitatory postsynaptic potential
FAIS	immunofluorescence intensity average in the AIS
Fpre	pre-AIS axon segment
GABA	gamma-aminobutyric acid
HCN	hyperpolarization-activated cyclic nucleotide-gated channel
Ih	hyperpolarization-activated current
IPSP	inhibitory postsynaptic potential
IQR	interquartile range
KIR	inward rectifier potassium channel
KV	voltage-gated potassium channel
NAV	voltage-gated sodium channel
PB	phosphate buffer
PC	pyramidal cell
Pvalb	parvalbumin-expressing
Rin	input resistance
rRin	input rectification ratio
TBS	Tris-buffered saline
TBST	TBS containing 0.X% Triton-X

TPM	transcripts per million
Vm	membrane potential
ZD7288	HCN blocker

Introduction

Microcircuit-Level Evolution in the Mammalian Neocortex

Multiple interacting processes, including increases in brain size, cortical folding, and the refinement of microcircuitry within the neocortex, shape the evolution of the mammalian brain. These transformations are largely driven by genetic and epigenetic modifications, including duplications and alterations in regulatory sequences that influence neuronal development and plasticity (Castillo-Morales et al., 2016; Kaas et al., 2013). As a result, species-specific expansions in cortical mantle volume and grey matter have developed, accompanied by increasingly complex microcircuit configurations.

Among these evolutionary changes, the neocortex stands out as a key innovation. Its six-layered structure supports advanced cognitive functions such as perception, reasoning, and decision-making (Barton, 2007; Castillo-Morales et al., 2016). Although the basic microcircuit motifs are conserved across mammals, their functional sophistication has diversified, reflecting adaptations to ecological and behavioral demands (Defelipe, 2011; Lewitus et al., 2013; Rakic, 2009). These changes are mirrored in both structural and molecular features of cortical circuits, with evidence suggesting that evolutionary pressures—including metabolic efficiency and environmental complexity—have shaped the architecture of the neocortex (Rogers et al., 2010).

Genetic variation plays a central role in modulating the composition and connectivity of cortical neurons. Across species, alterations in gene expression have contributed to distinct cortical organizations that underpin adaptive cognitive traits. The development of compartmentalized microcircuits has enabled parallel processing, rapid integration of information, and enhanced behavioral flexibility (Ghosh & Jessberger, 2013; Innocenti & Price, 2005). Furthermore, the neocortex's layered structure represents a fundamental evolutionary shift, facilitating specialized intra- and interlaminar communication and enabling the emergence of high-order processing capabilities (Kaas, 2013).

Increased neuronal density in some cortical areas correlates with enhanced cognitive capacity, particularly in species with larger brains, such as primates (Miller et al., 2019). Recent findings also highlight the role of molecular evolution in shaping cortical structure. For example,

accelerated evolution of adhesion molecules such as amyloid precursor-like proteins (APLP1) appears to have supported the development of synaptic complexity and the establishment of the neocortex's layered structure (Onodera et al., 2021). These insights emphasize the integrated role of genetic, molecular, and structural changes in driving neocortical specialization.

Taken together, the neocortex is a good example of a convergent outcome of evolutionary pressures shaping neural systems. Its expansion, folding, and microcircuit diversification reflect the interplay between genetic innovations and adaptive demands, ultimately enabling the emergence of sophisticated cognitive capabilities characteristic of mammals.

Divergence in Neocortical Neuron Functions: Genetic and Electrophysiological Differences Between Humans and Mice

Comparative analyses of neocortical neurons across mammalian species have uncovered key evolutionary differences in cellular identity, ion channel expression, and circuit function. With the advent of high-resolution techniques such as single-cell RNA sequencing, it has become increasingly clear that while many cortical neuron types are conserved across species, their molecular profiles and functional properties can diverge significantly. These differences are especially pronounced in GABAergic (gamma-aminobutyric acid) interneurons, which exhibit species-specific transcriptional signatures, ion channel expression, and morphological features (Hodge et al., 2019; Wang et al., 2022).

Among these interneurons, divergence in gene expression patterns reveals evolutionary adaptations that have altered neuronal function and connectivity. For instance, human GABAergic neurons express unique combinations of transcription factors and exhibit broader diversity in interneuron subtypes compared to their murine counterparts (Raju et al., 2018). Such differences are not merely genetic but extend to ion channel composition, which influences electrophysiological properties, including membrane excitability, firing dynamics, and synaptic integration (Hu et al., 2019; Poorthuis et al., 2018).

Although rodent models have long been central to neuroscience research, accumulating evidence demonstrates that even subtle differences in ion channel distribution or dendritic architecture can lead to great differences in circuit-level behavior between species (Campagnola et al., 2022; Eyal et al., 2016). For example, studies using human cortical tissue resected during

neurosurgery have shown functional distinctions in excitability, signal integration, and plasticity compared to rodent neurons (Galakhova et al., 2022; Lourenco & Bacci, 2017).

One striking example of molecular divergence involves the calcium-binding protein secretagogin, which is expressed in developing human GABAergic neurons but absent in mice. Its presence correlates with increased neurite complexity, suggesting enhanced roles in cortical integration and plasticity (Raju et al., 2018). Furthermore, the enriched expression of certain GABAergic subtypes in the human neocortex points toward an evolutionarily expanded inhibitory repertoire tailored for higher-order cognitive demands (Radonjic et al., 2014).

Differences in ion channel distribution further contribute to species-specific neuronal dynamics. For instance, human supragranular pyramidal neurons exhibit stronger hyperpolarization-activated cyclic nucleotide-gated (HCN) channel activity than those in mice, especially in deeper cortical layers (Kalmbach et al., 2018). These differences affect intrinsic excitability and the precision of spike timing, with implications for cognitive processes such as memory encoding and theta rhythm generation (Rich et al., 2021).

Taken together, these findings highlight the necessity of studying human neurons directly to understand the principles governing cortical function and dysfunction. Differences in gene regulation, ion channel composition, and interneuron diversity are not merely interspecies curiosities but reflect fundamental adaptations with significant implications for cognition, behavior, and disease modeling. Appreciating this divergence would be critical for translational neuroscience and for the development of therapeutic strategies against human psychiatric disorders.

Parvalbumin-Expressing Interneurons: Central Inhibitory Elements in the Mammalian Neocortex

Parvalbumin (Pvalb)-expressing interneurons are a core component of cortical inhibitory circuits and are among the most functionally specialized neuron types in the mammalian neocortex. Characterized by their fast-spiking behavior and ability to precisely regulate the timing and strength of pyramidal cell activity, Pvalb interneurons are essential for maintaining excitatory-inhibitory balance and supporting high-frequency network oscillations.

These interneurons are critically involved in regulating cortical excitability, synaptic plasticity, and the temporal precision of action potentials (Chen W, 1996; Wang et al., 2016). Their rapid membrane kinetics and dense perisomatic innervation of pyramidal neurons allow them to exert powerful inhibitory control, thereby shaping neuronal output and contributing to cognitive functions such as attention, working memory, and sensory integration (Jiang et al., 2012; Molnar et al., 2008).

Despite a shared core identity, Pvalb interneurons display species-specific differences in ion channel expression, firing properties, and morphology. Studies have shown that human fast-spiking interneurons exhibit subtle but functionally relevant distinctions in axonal arborization, synaptic integration, and ion channel kinetics compared to their rodent counterparts (Molnar et al., 2016; Poorthuis et al., 2018; Szegedi et al., 2020). These differences are thought to support the greater computational demands of the human cortex and reflect evolutionary refinements of inhibitory control mechanisms.

One of the most striking properties of Pvalb interneurons is their ability to fire at extremely high frequencies without significant frequency adaptation. In humans, these cells can sustain firing rates exceeding 300 Hz, supporting temporally precise inhibition that enhances cortical processing and synchronization (Wang et al., 2016). This capacity is enabled by a unique constellation of ion channels, particularly those located at the axon initial segment (AIS), such as Nav1.6 sodium channels and Kv1-type potassium channels, which collectively regulate action potential initiation, timing, and recovery (Goldberg et al., 2008; Kole et al., 2007).

Moreover, Pvalb interneurons contribute to the modulation of cortical dynamics through activity-dependent plasticity at their glutamatergic inputs. These synaptic modifications are essential for adapting inhibitory strength in response to changing network states and learning demands (Szegedi et al., 2016). Their connectivity patterns, particularly the dense innervation of local pyramidal cells, position them as key regulators of circuit output and oscillatory synchrony.

In summary, parvalbumin-expressing interneurons represent a fundamental inhibitory class within the neocortex, whose unique physiological properties and circuit roles are shaped by species-specific adaptations. Understanding their molecular composition, electrophysiological

profiles, and synaptic dynamics offers critical insights into the cellular basis of cortical computation and the evolutionary forces that have shaped mammalian brain function.

Ion Channel Specialization in Parvalbumin Interneurons: Molecular Determinants of Fast-Spiking Excitability

The unique physiological properties of Pvalb interneurons are fundamentally shaped by their distinct repertoire of ion channels, which confer rapid membrane responsiveness, high-frequency firing, and precise synaptic integration. These ion channels are critical for regulating action potential (AP) threshold, timing, and recovery, thereby supporting the functional role of Pvalb interneurons in maintaining cortical stability and information processing (Markram et al., 2004; Tremblay et al., 2016).

Among the most influential of these channels are **hyperpolarization-activated cyclic nucleotide-gated (HCN)** channels, **voltage-gated sodium (Nav1)** and **potassium (Kv1)** channels, , and **inward rectifier potassium (Kir)** channels. Together, they orchestrate the intrinsic excitability and firing dynamics that distinguish fast-spiking interneurons from other neuronal populations.

HCN Channels (Hyperpolarization-Activated Cyclic Nucleotide-Gated Channels)

HCN channels mediate the **Ih current**, which becomes active at subthreshold voltages and contributes to membrane potential stability and resonance properties. In Pvalb interneurons, HCN channels support persistent firing by facilitating membrane depolarization following hyperpolarization, thereby influencing synaptic responsiveness and excitatory-inhibitory balance (Nusser, 2009; Shah, 2014).While HCN1 and HCN2 isoforms are expressed in both humans and rodents, electrophysiological studies reveal species-specific differences in their localization and functional impact. In human neocortical neurons, HCN currents are more pronounced at the soma, enhancing EPSP-spike (excitatory postsynaptic potential) coupling and temporal fidelity (Guet-McCreight et al., 2023). In contrast, rodent Pvalb neurons predominantly express HCN channels in axonal compartments, suggesting divergent roles in firing modulation and neurotransmitter release (Nusser, 2009; Roth & Hu, 2020).

Kir Channels (Inward Rectifier Potassium Channels)

Kir channels regulate membrane excitability by stabilizing the resting membrane potential and shunting subthreshold excitatory inputs. These channels are activated during hyperpolarized states and play a key role in setting the excitability threshold of Pvalb neurons (Goldberg et al., 2011; Hibino et al., 2010). In rodents, Kir channels provide strong inhibition at membrane potentials negative to rest, dampening spontaneous firing and enhancing input selectivity. However, their precise roles in human Pvalb interneurons remain less well characterized, highlighting the need for further comparative studies using human tissue (Anderson et al., 2021).

Nav1.6 Channels (Voltage-gated Sodium Channels)

Voltage-gated sodium channels, particularly the **Nav1.6 isoform**, are densely clustered at the axon initial segment (AIS), where they are essential for action potential initiation. Nav1.6 channels exhibit rapid activation and recovery kinetics, enabling Pvalb interneurons to sustain high-frequency firing without accommodation (Lorincz & Nusser, 2008; Sun et al., 2013). Their distribution and density shape the AP threshold and are closely linked to the geometry of the AIS. In human neurons, small differences in AIS structure and Nav1.6 expression contribute to lower AP thresholds compared to mouse neurons, supporting increased responsiveness and computational precision (Lorincz & Nusser, 2008).

Kv1 Channels (Voltage-gated Potassium Channels)

Kv1-type potassium channels, especially **Kv1.1** and **Kv1.2**, are enriched in the AIS and govern repolarization dynamics and interspike intervals. These channels act as subthreshold modulators of excitability, curbing excessive depolarization and ensuring temporal precision in firing (Gu & Barry, 2011; Kole et al., 2007). The functional specialization of Kv1 subtypes allows for improved control of spike timing and gain modulation(Goldberg et al., 2008; Gu & Barry, 2011; Kole et al., 2007).

Collectively, the concerted action of these ion channels underpins the fast-spiking phenotype of Pvalb interneurons and shapes their role in neocortical computation. Differences in ion channel expression, localization, and kinetics between species point to evolutionary adaptations that optimize interneuron performance for species-specific cortical demands.

The Axon Initial Segment: Structural and Functional Specialization for Action Potential Initiation

The axon initial segment (AIS) is a highly specialized neuronal domain that serves as the principal site of AP initiation. This region, typically located at the proximal axon just distal to the soma, is characterized by a high density of voltage-gated ion channels and a unique cytoskeletal architecture that enables the integration of synaptic inputs and trigger precise neuronal output. In fast-spiking interneurons, the AIS plays a critical role in establishing the low AP thresholds and high temporal precision required for rapid and reliable inhibitory control.

The spatial arrangement of the AIS—its length, position relative to the soma, and biophysical features—significantly influences neuronal excitability. An AIS positioned closer to the soma is more affected by somatodendritic membrane capacitance and axial resistance, while a more distal AIS is electrically more isolated, boosting its capacity to respond independently to depolarizing currents. However, this isolation also causes increased charge dissipation along the axon, which may require stronger depolarization to reach the threshold (Goethals & Brette, 2020; Leterrier, 2018). Therefore, AIS location and shape represent a trade-off between excitability and electrical compartmentalization, finely adjusted for each neuron type and species, and likely serving as a substrate for plasticity mechanisms.

Species-specific variations in AIS structure and ion channel distribution have important implications for cortical function. In particular, studies have shown that human Pvalb interneurons exhibit a **lower action potential threshold** than their rodent counterparts, a property which might be linked to differences in AIS morphology and Nav1.6 channel density (Lorincz & Nusser, 2008). These adaptations support more sensitive and temporally precise responses to excitatory inputs, probably reflecting the heightened computational demands of the human cortex.

The AIS is enriched with several key ion channels, including **Nav1.6** sodium channels and **Kv1** potassium channels. Nav1.6 facilitates rapid depolarization necessary for AP initiation, while Kv1 channels regulate repolarization and influence firing threshold and frequency. The interaction between these channels governs the precise biophysical properties required for fast and efficient spike generation (Goldberg et al., 2008; Gu & Barry, 2011; Kole et al., 2007).

The molecular scaffolding that anchors these ion channels is equally critical. The cytoskeletal protein **βIV-spectrin**, in complex with **ankyrin-G**, plays a central role in maintaining AIS integrity. βIV-spectrin organizes the periodic cytoskeletal lattice and anchors voltage-gated channels, ensuring their stable localization and function (Jones & Svitkina, 2016; Leterrier, 2018). Loss of ankyrin-G disrupts AIS assembly, impairs channel clustering, and elevates firing thresholds, thereby compromising neuronal output (Winckler, 1999).

Differences in AIS composition and molecular organization across species suggest that its structure has undergone evolutionary tuning to match circuit-level requirements. In humans, longer or more distally located AISs may confer enhanced excitability and dynamic range, contributing to advanced integrative functions in neocortical networks (M. C. Inda et al., 2006). This specialization is particularly relevant in fast-spiking interneurons, where the precision of inhibitory timing is critical for shaping cortical rhythms and supporting cognition.

In summary, the AIS is a dynamic and evolutionarily adaptable structure that integrates ion channel distribution, cytoskeletal architecture, and biophysical constraints to regulate neuronal firing. Understanding species-specific differences in AIS organization is essential for decoding how intrinsic excitability contributes to the complexity of cortical computations and for interpreting interspecies variability in both normal and pathological brain states.

Evolutionary and Translational Significance of Species-Specific Neuronal Specializations

The discovery of substantial molecular and functional differences in neuronal properties between humans and commonly used laboratory species, such as mice and rats, has significant implications for both basic neuroscience and translational research. Although rodent models have been instrumental in uncovering fundamental mechanisms of brain function, increasing evidence reveals that key features of human cortical neurons — including their morphology, ion channel composition, and electrophysiological properties — have diverged in ways that may impact the interpretation and applicability of animal data (Campagnola et al., 2022; Kalmbach et al., 2018; Rich et al., 2021).

This divergence is particularly relevant for **parvalbumin interneurons**, which are key regulators of excitatory-inhibitory balance and are targeted in a range of neurological and

psychiatric disorders. Many pharmacological treatments developed in rodents have failed in human trials, in part due to species-specific differences in neuronal function and circuit architecture. As such, a deeper understanding of how Pvalb interneurons differ across species, from gene expression to AIS structure and ion channel dynamics, is essential for refining disease models and identifying effective therapeutic targets.

The observation that human Pvalb interneurons have a lower action potential threshold, along with broader and more complex arborization patterns, underscores an evolutionary trajectory favoring enhanced temporal precision and inhibitory control. These adaptations likely support the expanded cortical territories and cognitive capacities seen in primates and humans.

Molecular differences in ion channel expression — particularly in **HCN**, **Nav1.6**, **Kv1**, and **Kir** families — may reflect adaptive responses to the metabolic and computational demands imposed by a larger and more interconnected neocortex. Evolutionary tuning of these channels, combined with structural refinements such as AIS positioning and βIV–spectrin–mediated cytoskeletal organization, suggests that interneuron excitability has been optimized differently across species to match ecological and cognitive requirements.

The ability to study these differences using **surgically resected human brain tissue** offers a unique opportunity to bridge the gap between animal models and human neurobiology. Such tissue provides not only direct insight into human-specific neuronal features but also a foundation for building accurate models of brain disorders.

In conclusion, comparative studies of neocortical microcircuits — particularly those focusing on fast-spiking inhibitory interneurons — reveal an intricate evolutionary narrative of divergence and specialization. Understanding how these cellular properties have been shaped across species offers essential insights into the principles of brain evolution and paves the way for more precise and effective approaches in neuroscience research and clinical intervention.

Aims

The overarching goal of this doctoral research was to characterize the molecular, anatomical, and electrophysiological properties of homologous interneuron types — specifically, parvalbumin-expressing fast-spiking basket cells — in the human and mouse neocortex. By examining conserved neuron classes across species, the study aimed to identify human-specific adaptations at the protein, genetic, and microcircuit levels.

The specific research questions addressed include:

1. **HCN Channel Localization and Function**
   How does the subcellular distribution of hyperpolarization-activated cyclic nucleotide-gated (HCN) channels, particularly at the soma versus dendrites, differ between species? What are the electrophysiological consequences of this divergence?
2. **Kir Channel Regulation of Excitability**
   How does higher baseline input resistance in human Pvalb interneurons influence the functional effect of Kir (inward rectifier potassium) channel activation compared to mouse cells? Are there differences in the expression levels or membrane localization of Kir3.1 and Kir3.2 between species?
3. **Axon Initial Segment (AIS) Specialization**
   Can interspecies differences in AIS length, position, and ion channel composition account for variations in action potential thresholds and inhibitory control?

To address these aims, I contributed to the morphological visualization of neurons characterized by electrophysiology, confirmed their parvalbumin expression, and performed immunohistochemical staining using various markers. These preparations were imaged via confocal microscopy, followed by quantitative analysis in collaboration with Dr. Ádám Tiszlavicz.

Materials and Methods

Ethics statement and licenses

All procedures were approved by the University of Szeged Ethics Committee and Regional Human Investigation Review Board (ref. 75/2014) and conducted in accordance with the tenets of the Declaration of Helsinki. Written informed consent for studies on excised human cortical tissue was obtained from all patients prior to surgery. Tissue obtained from underage patients was provided with agreement from a parent or guardian.

Human brain slices

Neocortical slices were prepared from samples of frontal, temporal, or other cortex removed for the surgical treatment of deep-brain targets. Patients ranged from 20 to 82 years of age, and samples were acquired from both the left and right hemispheres of males and females. Anesthesia was induced with intravenous midazolam (0.03 mg/kg) and fentanyl (1 to 2 μg/kg) following bolus intravenous injection of propofol (1 to 2 mg/kg). Patients also received 0.5 mg/kg rocuronium to facilitate endotracheal intubation. Patients were ventilated with a 1:2 O_2/N_2O mixture during surgery, and anesthesia was maintained with sevoflurane. Following surgery, the resected tissue blocks were immediately immersed in an ice-cold solution containing (in mM) 130 NaCl, 3.5 KCl, 1 NaH_2PO_4, 24 $NaHCO_3$, 1 $CaCl_2$, 3 $MgSO_4$, and 10 D(+)-glucose aerated with 95% O_2/5% CO_2 within a glass container. The container was then placed on ice inside a thermally isolated box and immediately transported from the operating room to the electrophysiology laboratory with continuous 95% O_2/5% CO_2 aeration. Slices of 350 μm thickness were prepared from the tissue block using a vibrating blade microtome (Microm HM 650 V) and then incubated at 22˚C to 24˚C for 1 h in slicing solution. The slicing solution was gradually replaced with a recording solution (180 mL) using a pump (6 mL/min). The contents of the recording solution were identical to the slicing solution except that it contained 3mM $CaCl_2$ and 1.5 mM $MgSO_4$.

Mouse brain slices

Transversal slices (350 μm) were prepared from the somatosensory and frontal cortices of 5–7-week-old heterozygous B6.129P2-Pvalbtm1(cre)Arbr/J mice (stock 017320, B6 PVALBcre line, Jackson Laboratory, Bar Harbor, ME, USA) crossed with the Ai9 reporter line to express the

tdTomato fluorophore in Pvalb GABAergic neurons to assist in cell selection. Cell identity was tentatively confirmed electrophysiologically by fast spike kinetics and high-frequency non-accommodating firing in response to 500-ms suprathreshold depolarizing pulses (Szegedi et al., 2017).

Drug

The HCN channel blocker ZD7288, $BaCl_2$, dendrotoxin-K (DTXK) (Merck/Sigma-Aldrich) were diluted in physiological extracellular solution and applied by wash-in.

Electrophysiological recordings and data analysis

Recordings were performed in a submerged chamber perfused at 8 mL/min with recording solution maintained at 36˚C to 37˚C. Cells were patched under visual guidance using infrared differential interference contrast video microscopy and a water-immersion 20× objective with additional zoom (up to 4×). All cells experiments were performed within 30 min from entering to whole cell mode. Micropipettes (5 to 8MΩ) for whole-cell patch-clamp recording were filled with intracellular solution containing (in mM) 126 K-gluconate, 8 NaCl, 4 ATP-Mg, 0.3 Na_2–GTP, 10 HEPES, and 10 phosphocreatine (pH 7.0 to 7.2; 300 mOsm) and supplemented with 0.3% (w/v) biocytin for subsequent staining with Alexa 488–conjugated streptavidin. Recordings were performed with a Multiclamp 700B amplifier (Axon Instruments) and lowpass filtered at a 6 to 8 kHz cutoff frequency (Bessel filter). Series resistance and pipette capacitance were compensated in current-clamp mode, and pipette capacitance was compensated in voltage-clamp mode. In voltage-clamp recordings, the effect of access resistance (measured first in current-clamp) on the nominal clamping potential reading was calculated and corrected during data analysis. The resting membrane potential (Em) was recorded starting 1 to 3 min after patch rupture. Membrane potential values were not corrected for liquid junction potential error. The somatic leakage conductance (Gleak) was measured in voltage-clamp mode as the ratio of evoked current to voltage step amplitude (−10 mV for 10 ms) according to Ohm's law as follows: Gleak (nS) = clamping current amplitude at the end of the voltage step (pA)/voltage-clamp step amplitude (mV). Somatic input resistance was measured in current-clamp mode by measuring the current required to hyperpolarize the membrane to −90 mV peak potential (250 to 500 ms) from −70 mV. Somatic tau values were measured in the current–clamp mode for depolarizing (+10 mV) Vm steps (250–500 ms) from −70

mV. The AP firing threshold was measured in the dV/dt per Vm phase plots as the Vm at which the AP initial rise speed reaches 10 mV/ms (Li et al., 2014; René Wilbers et al., 2023). All parameters were measured from at least five traces. Outside-out somatic membrane recordings were conducted after whole-cell recordings by retracting the pipette under visual guidance using a microscope-associated camera. Bridge balance was set during experiments. Sag amplitudes were calculated from at least 5 steps in each configuration. Data were acquired using Clampex software (Axon Instruments), digitized at 35–50 kHz, and analyzed offline using pClamp (version 10.5, Axon Instruments), Spike2 (version 8.1, Cambridge Electronic Design, Milton, UK), OriginPro (version 9.5, OriginLab Corporation, Northampton, MA, USA), and SigmaPlot (version 14, Grafiti, Palo Alto, CA, USA).

Single-cell model

The program used in the simulations was written by Attila Szucs in Delphi language (Hernath et al., 2019; Szabo et al., 2021). My superviser, Karri Lamsa, and my college Adam Tiszlavicz, constructed a model neuron incorporating electrophysiological parameters derived from experimental findings to assess the effects of somatic HCN channels on the input–out responses of basket cells. The three-compartmental model neuron including cylindrical dendritic and axonal compartments was based on the formalism described previously (Szucs et al., 2017). The model consisted of a somatic compartment in addition to one axonal and one dendritic cable compartment, both 200 μm in length and 1.2 μm in diameter. Cable parameters were axon longitudinal resistance = 1.0MΩ per μm and capacitance = 12 fF/μm^2 for both the axon and dendrite (also referred to as the "primary dendrite"). The somatic compartment had an ohmic resistance of 400MΩ, capacitance of 12 pF, and the leakage current reversal potential of −62 mV. In addition, the model incorporated 5 voltage-dependent currents: transient Na^+ current, delayed rectifying K^+ current (Kd), HCN current, slowly activating M-type K^+ current, and inward-rectifying K^+ current (Kir). Parameters such as rheobase and voltage sag were chosen to replicate basic response properties and adjusted using experimental data to attain the best match with recorded voltage traces. All intrinsic voltage-dependent currents were calculated according to the Eq 1:

$$I_i = g_i m_i^p h_i (E_i - V),$$

where *i* represents the individual current type, *gi* is the maximal conductance of the current, *mi* is the activation variable, *p* is the exponent of the activation term, *hi* is the inactivation variable (either first-order or absent), and *Ei* is the reversal potential. Activation (*m*) and inactivation (*h*) kinetics were modeled according to the Eq 2:

$$\frac{dx}{dt} = \frac{x_\infty(V) - x}{\tau_x(V)} \ ,$$

where x represents m or h, and voltage-dependent steady-state activation and inactivation are described by the sigmoid function Eq 3:

$$x_\infty(V) = \frac{1}{2} + \frac{1}{2}\tanh\left(\frac{V - V_{x,\frac{1}{2}}}{V_{x,sl}}\right).$$

The midpoint $V_{x,1/2}$ and slope $V_{x,sl}$ parameters of the sigmoids and the other kinetic parameters are shown in S2 Table. Time constants (τ) of activation and inactivation were modeled as bell-shaped functions of the membrane potential (V) according to the Eq 4:

$$\tau_x(V) = \left(\tau_{x,max} - \tau_{x,min}\right)\left[1 - \tanh\left(\frac{V - V_{\tau x,\frac{1}{2}}}{V_{\tau x,sl}}\right)^2\right] + \tau_{x,min} \ .$$

The voltage-dependent Na^+, and K^+ Kd- and M-currents were assigned to the axonal and somatic compartments, while the HCN and Kir currents were included in the somatic and dendritic compartments. The model was tested using a current-step protocol matching the one used for biological neurons (0.5 s duration current steps starting at −100 pA and increasing in increments of +20 pA). Membrane resistance, time constant, voltage sag, and other parameters were calculated from the voltage responses and compared to those observed in representative human basket cell. In addition to the intrinsic voltage-dependent currents, we included a chemical GABAergic autaptic connection from the axon to the somatic compartment of the model as autaptic inhibition is a regular feature of human L2/3 neocortical Pvalb interneurons and has a clear impact on the hyperpolarizing phase of action potential waveform (Szegedi et al., 2020). The parameters of the autaptic connection were as follows: conductance = 2.5 nS, conductance onset delay to action potential peak = 1 ms; time to peak = 0.8 ms; current decay time constant = 10 ms; activation

threshold = −32 mV; slope of the activation function = 20 mV; reversal potential of the autaptic current = −72 mV.

Autaptic current was described using a first-order kinetics of transmitter release as defined in Eq 5:

$$I_{syn} = g_{syn}S\,(E_{syn} - V),$$

where S is the instantaneous autaptic activation term yielding the following differential Eq 6:

$$\frac{dS}{dt} = \frac{S_\infty(V_{pre}) - S}{\tau_{syn}\left(1 - S_\infty(V_{pre})\right)} \quad .$$

The steady-date autaptic activation term depends on the cell membrane potential as defined in Eq7:

$$S_\infty(V_{pre}) = \tanh\left(\frac{V_{pre} - V_{th}}{V_{slope}}\right)$$

when $V_{pre} > V_{th}$. Otherwise $S_\infty(V_{pre}) = 0$. The term V_{pre} denotes the membrane potential of the axon cable.

The three-compartmental model neuron, including its cylindrical dendritic and axonal compartments, was based on the previously described formalism. The model consisted of a somatic compartment, axonal compartment, and dendritic cable compartment. The axon was 140 µm in length long and 0.8 µm in diameter, and the dendrite was 200 µm in length and 1 µm in diameter. The cable parameters were as follows: axon Ra = from 0.8 to 1.1 MΩ·µm and axon Cm = 6 fF/µm^2. Cm was 2-fold higher for the dendrite (12 fF/µm^2) than for the axon. The ohmic resistance of the somatic compartment was 700 MΩ, and Cm of the somatic compartment was 25 pF. The leakage reversal potential was set to −68 mV. Parameters such as the rheobase and voltage sag were chosen to replicate the basic response properties and were carefully adjusted using the experimental data to attain the best match between the simulated and recorded voltage traces.

Statistics

In the Research Study I the results are presented as median with lower to upper quartile range (IQR) unless stated otherwise. Statistical significance was evaluated by Mann–Whitney U test, Wilcoxon signed-rank test, or ANOVA on Ranks (Kruskal–Wallis H test) as indicated using Sigma Plot. Correlations were tested using Pearson's or Spearman Rank Order method. A $P < 0.05$ was considered significant for tests. Parametric distribution was confirmed with the Shapiro–Wilk test as $P > 0.05$.

In the Research Study II the data were presented as the median and interquartile range. Statistical significance was tested using the Mann–Whitney U test, ANOVA on ranks (Kruskal–Wallis H test) with Dunn's *post hoc* pairwise test, or one-way MANOVA with Bonferroni's *post hoc* test to assess differences between multiple samples. Associativity and correlations were tested using the Spearman rank order method. Tests were performed using SigmaPlot 15. Inset symbols and icons were prepared from premade icons and templates using BioRender's web-based free software (https://www.biorender.com).

In the Research Study III the results are presented as medians and IQRs. Statistical comparisons were performed using the Student's t-test, the Mann–Whitney U test, Wilcoxon signed-rank test with Bonferroni correction, ANOVA on ranks (Kruskal–Wallis H test) with Dunn's post hoc pairwise test, or PERMANOVA and the Mann–Whitney U test with Bonferroni correction. Proportions were compared using the chi-squared test with Benjamini–Hochberg adjustment at a 5% significance level. Correlations were assessed using Spearman's rank-order method.

Tissue fixation and cell visualization

Cells filled with biocytin from whole-cell patch-clamp recording were visualized using either Alexa 488–conjugated streptavidin (1:1,000) or Cy3-conjugated streptavidin (1:1,000) (both from Jackson ImmunoResearch). After recording, slices were immediately fixed in a solution containing 4% paraformaldehyde and 15% picric acid in 0.1Mphosphate buffer (PB; pH = 7.4) at 4˚C for at least 12 h and then stored at 4˚C in 0.1MPB containing 0.05% sodium azide as a preservative. All slices were embedded in 20% gelatin and further cut into 60-µm thick sections in ice-cold PB using a vibratome (VT1000S, Leica Microsystems, Wetzlar, Germany). After sectioning, they were rinsed in 0.1MPB (3 × 10 min), cryoprotected in 10% to 20% sucrose solution

in 0.1MPB, flash-frozen in liquid nitrogen, and thawed in 0.1MPB. Slice sections were then incubated in 0.1MTris-buffered saline (TBS; pH 7.4) containing fluorophore-conjugated streptavidin for 2.5 h at 22˚C to 24˚C. After washing with 0.1MPB (3 × 10 min), the sections were covered in Vectashield mounting medium (Vector Laboratories, Burlingame, CA, USA), placed under coverslips, and examined under an epifluorescence microscope at 20 to 60× magnification (Leica DM 5000 B).

Conversion of selected cells to DAB and anatomical reconstruction

Sections (60-µm thick) used for single-cell reconstruction were further incubated in a solution of conjugated avidin-biotin horseradish peroxidase (ABC; 1:300; Vector Labs) in TBS (pH = 7.4) at 4˚C overnight. The enzyme reaction was visualized by the glucose oxidase-DAB-nickel method using 303-diaminobenzidine tetrahydrochloride (0.05%) as the chromogen and 0.01% H_2O_2 as the oxidant. Sections were further treated with 1% OsO_4 in 0.1MPB. After several washes in distilled water, sections were stained with 1% uranyl acetate, dehydrated in an ascending series of ethanol concentrations, infiltrated with epoxy resin (Durcupan) overnight, and embedded on glass slides. Light microscopic reconstructions were conducted using the Neurolucida system with a 100× objective (Olympus BX51, Olympus UPlanFI). Images were collapsed in the z-axis for illustration.

Immunohistochemistry

Free-floating sections were washed three times in TBS containing 0.3% Triton-X (TBST) for 1 h at 20-24°C. They were then moved to a blocking solution consisting of 20% horse serum in TBST. The sections were treated with 1 mg/mL pepsin (catalog #S3002; Dako, Glostrup, Denmark) in 1 M HCl with 0.1 M PB at 37°C for 5-6 min and then washed in 0.1 M PB. All sections were incubated in primary antibodies diluted in TBST over three nights at 4°C followed by the appropriate fluorochrome-conjugated secondary antibody solution (2% blocking serum in TBST) overnight at 4°C. The sections were first washed in TBST (thrice for 15 min each), washed in 0.1 M PB (twice for 10 min each), and finally mounted on glass slides with Vectashield mounting medium (Vector Laboratories, Burlingame, CA, USA). The following primary antibodies were used for immunostaining of brain sections: mouse anti-pv (1:500, Swant, Switzerland, www.swant.com, clone: 235); rabbit anti-HCN1 (1: 500, MyBioSource), rabbit anti-HCN2 (1: 500,

MyBioSource), rabbit anti-KV3.1 (1:500, Synaptic Systems, www.sysy.com), goat anti-pvalb (1:1000, PVG-213, Swant, Burgdorf, Switzerland); mouse anti-spectrin beta-4 (1:100, Invitrogen, Thermo Fisher Scientific, Waltham, MA, USA), rabbit anti-Nav1.6 (SCN8A, 1:300, Alomone Labs, Jerusalem, Israel); rabbit anti-Kv1.1 (KCNA1, 1:100, Alomone Labs), and rabbit anti-Kv1.2 (KCNA2 APC-010, 1:100, Alomone Labs), rabbit Anti-GIRK1 polyclonal (Kir3.1) (1:200, Alomone Labs, Jerusalem, Isreal), rabbit Anti-GIRK2 antibody monoclonal (Kir3.2) (1:200, Abcam, www.abcam.com). Immunolabeling was visualized for confocal microscopy using the following secondary antibodies: DAM Alexa 488–conjugated donkey anti-mouse (1:400, Jackson ImmunoResearch, www.jacksonimmuno.com) or DAM Cy3-conjugate donkey anti-mouse (1:400, Jackson ImmunoResearch). For dSTORM, secondary antibodies were DARb Alexa 647 donkey anti-rabbit (1:500, Abcam, www.abcam.com) and DaRb CF568 (1:500, Biotium). DARb Cy3-conjugate donkey anti-rabbit (1:400, Jackson ImmunoResearch), and DaGt A647-conjugate donkey anti-goat (1:200, Thermo Fisher Scientific). The immunoreactions were evaluated first using an epifluorescence microscope (Leica DM 5000 B) and then a laser scanning confocal microscope (Nikon Eclipse Ti-E).

Confocal microscopy

Confocal images were captured using a Nikon C2+ confocal scan head attached to a Nikon Eclipse Ti-E microscope equipped with a high NA objective (Nikon CFI Apo TIRF 100XC Oil, NA = 1.49). The setup and data acquisition process were controlled by Nikon NIS-Elements 5.02 software, and images were postprocessed in MATLAB. The Nikon Laser Unit was used to set the wavelength and power of the following applied lasers: Sapphire 488 LP-200 (Pmax = 200 mW, Coherent, Santa Clara, CA, USA) for 488 nm excitation; Cobolt Jive (Pmax = 300 mW, Cobolt, Kassel, Germany) for 561 nm excitation; 2RU-VFL-P-300-647-B1 (Pmax = 300 mW, MPB Communications, Montreal, Canada) for 647 nm excitation.

In Research Study II-III, the examination of the brain slices labeled for immunofluorescence were acquired using a Leica Stellaris 8 laser-scanning confocal microscope (Leica Microsystems. Biomarker Kft. Budapest, Hungary) with 499-, 554-, and 649-nm lasers for excitation of the fluorophores. The utilized emission filters for these lasers were 504–553, 559–654, and 654–750 nm, respectively. Z-stack images were taken using a HC PL APO CS2 63×/1.40 oil immersion objective in a unidirectional scanning mode.

Line analysis of immunofluorescence intensity

Immunofluorescence images of Pvalb-expressing neurons, as well as fluorophore-labeled HCN1, HCN2, and Kv3.1 channels were captured using a Leica Stellaris-8 confocal microscope system, with special care to avoid pixel saturation. Images were then analyzed offline using LAS X Life Science Microscope Software. Briefly, an analysis template with six radial fluorescence measuring lines was positioned on an individual Pvalb-immunopositive cell soma so that the template center was approximately at the soma center and the end of each measuring line (length 8 μm, 15 pixels per μm) extended to the extracellular space. Thus, each line read pixellevel fluorescence intensity from the soma center to the edge (border of the extracellular space in two dimensions). The lines were positioned symmetrically at 60˚ angles. Fluorescent signals from Pvalb immunoreactivity in human cells and genetically encoded tdTomato in mouse cells were used to define the intracellular region. Intracellular signals from line analysis are likely to originate from both cytoplasm and nucleus since we were not able to clearly discriminate these subcellular regions. For analysis, the membrane zone was defined exactly as a 1-μm-wide region with midpoint where Pvalb (or tdTomato) fluorescence intensity reached half maximum (measured between 20% and 80% of signal minimum and maximum amplitude), while the extracellular region was defined from immediately outside this membrane zone. For measurement of fluorescence intensity values in each cell, readings from the six lines were first aligned and averaged as demonstrated in Fig 4A–D, Fig 6F-G. Average fluorescence intensity values for labeled HCN1 and HCN2 channels used to calculate ratios in Fig 4 and Fig 6 were collected from 3-μm, 1-μm, and 1-μm line lengths across intracellular, membrane zone, and extracellular regions, respectively.

In the Kir project the confocal immunofluorescence microscopy images of neurons were analyzed using ImageJ (US National Institutes of Health, Bethesda, MD, USA). To determine the edge and centroid of the cell soma, the images were segmented by adjusting the threshold of the Pvalb immunofluorescence signal. This was followed by removing small, unrelated particles and closing the soma segment if necessary. Segmentation was performed using the IsoData thresholding method, also known as iterative intermeans (10.1109/TSMC.1978.4310039). A straight line of selected length was then drawn at equal angular intervals. Intensity profiles for both Kir3.1 or Kir3.2 and Pvalb immunofluorescence channels were acquired along each line (from outside to inside the cell). Segments extending from the centroid of soma to the distal end of each

line were aligned by the alleged extracellular membrane location (defined by the appearance of Pvalb immunofluorescence signal in line analysis. Means, upper and lower quartiles were calculated for each position along the lines and normalized to the maximum average.

Twenty-four measurement lines, each with 50 pixels per micrometer, were placed on a cell soma so that all lines projected radially from the soma center to the extracellular space. Immunofluorescence intensity for Pvalb (Cy5) and one of the three ion channels (Cy3) was measured along the lines in a single-plane confocal microscopic image of the cell soma. The extracellular membrane location was defined by the Pvalb signal onset when moving from the extracellular to the intracellular direction within the line analysis. This point was marked as 0 and defined as follows: (average extracellular fluorescence pixel value minus average intracellular fluorescence pixel value)/2. In the pooled analysis, all lines were aligned at the 0-point. The fluorescence signal for ion channels was averaged from the extracellular space (-3.0 to -0.5 μm from the 0-point) and used as a reference signal for the rest of the line. The average extracellular site signal for each cell was subtracted from the line pixels at the membrane (-0.5 to +0.5 μm from the 0-point) and the pixels in the intracellular cytoplasm (+0.5 to +1.5 μm from the 0-point). Extracellular cite fluorescence intensity was similar between species (Kv1.1, $p=0.06$, $n=31$ and 31; Kv1.2, $p=0.835$, $n= 32$ and 59) (Mann-Whitney U-test). The intracellular cite measurement was taken from the vicinity of the extracellular membrane to capture the cytoplasm and avoid the nucleus. (The nucleus was not visualized in the immunostainings to determine when the intracellular line moves from the cytoplasmic site into the nucleus.) Medians and upper and lower quartiles were calculated for each position along the lines. In each cell, the average extracellular site signal (from 24 lines) was also used as a reference for pixels in the axon. The pixels of the axonal line for ion channel fluorescence intensity had the same average subtracted as the extracellular lines of the cell. Fluorescence measurement line in the axon had 50 pixels per μm. To analyze AIS immunofluorescence in z-stack images, we used an in-house macro of ImageJ software (US National Institutes of Health, Bethesda, MD, USA) and a custom-made script (Ollion et al., 2013) developed by Dr. Adam Tiszlavicz to determine the length and proximal and terminal points of the AIS (visualized by beta-IV-spectrin immunoreaction) using the Euclidean distance formula by manually marking the points. We measured the fluorescence intensity profiles along the axon following a polyline of the connected points to establish the entire fluorescence signal line for the immunofluorophore signals. The AIS lengths were normalized (expressed as 10 bins) to the

proximal and terminal distances because of the different lengths of the AIS, and the intensity was normalized to the maximum and minimum values of the binned data. The immunoreaction intensity of the ion channel was measured in parallel with Pvalb (Cy5) and beta-IV-spectrin (Alexa 488) in the Cy3 fluorescence channel. The immunofluorescence values of axonal data pixels were referenced to the average extracellular site intensity of each cell, using the same reference as for radial line pixels.

dStorm microscopy

The dStorm microscopy measurements were made by Bálint H. Kovács. Super-resolution dSTORM measurements were performed on a custom-made inverted microscope based on a Nikon Eclipse Ti-E frame with an oil immersion objective (Nikon CFI Apo TIRF 100XC Oil, NA = 1.49). Epifluorescence illumination was applied at an excitation wavelength of 647 nm. The laser intensity was set to 2 to 4 kW/cm^2 on the sample plane and controlled via an acousto-optic tunable filter. An additional laser (405 nm, Pmax = 60 mW; Nichia) was used for reactivation. A filter set from Semrock (including a Di03-R405/488/561/635-t1-25 × 36 BrightLine quad-edge super-resolution/TIRF dichroic beam-splitter and FF01-446/523/600/677-25 BrightLine quad-band bandpass filter, and an additional AHF 690/70 Hemission filter) was inserted into the microscope to separate excitation from emission wavelengths. Images of individual fluorescent dye molecules were captured by an Andor iXon3 897 BV EMCCD camera (512 × 512 pixels with 16 μm pixel size) with the following acquisition parameters: exposure time = 20 ms; EM gain = 200; temperature = −75˚C. Typically, between 20,000 and 25,000 frames were captured from a single region of interest. The Nikon Perfect Focus System was used to keep the sample in focus during measurements. High-resolution images were reconstructed with the rainSTORM localization software (http://laser.cheng.cam.ac.uk/wiki/index.php/Resources). Spatial drift introduced by either mechanical movement or thermal effects was analyzed and reduced using an autocorrelation-based blind drift correction algorithm. Background autofluorescence was calculated as the weighted moving average of neighboring pixel values and subtracted from each frame before the localization step. Using this subtraction method, pixel values within the noise level carried more weight because they do not belong to a fluorescent burst of a switching fluorophore. The detected localizations were filtered based on the fitting parameters (e.g., sigma values, residue, and intensity). The pixel size of the final pixelized super-resolution images (typically 20 nm) was set

based on the localization precision and localization density. The dSTORM experiments were conducted in a GLOX switching buffer, and the sample was mounted onto a microscope slide. The imaging buffer was an aqueous solution diluted in PBS containing the GluOx enzymatic oxygen scavenging system, 2,000 U/mL glucose oxidase (Sigma-Aldrich, catalog number: G2133-50KU), 40,000 U/mL catalase (Sigma-Aldrich, catalog number: C100), 25 mM potassium chloride (Sigma-Aldrich, catalog number: 204439), 22 mM tris(hydroxymethyl)aminomethane (Sigma-Aldrich, catalog number: T5941), 4mM tris(2-carboxyethyl)phosphine (TCEP) (Sigma-Aldrich, catalog number: C4706) with 4% (w/v) glucose (Sigma-Aldrich, catalog number: 49139), and 100 mM β-mercaptoethylamine (MEA) (Sigma-Aldrich, catalog number: M6500). The final pH was set to 7.4.

Nucleus collection for patch-sequencing

We collected the nuclei of cells that exhibited the fast-spiking phenotype. Before collecting the data, we made sure to thoroughly clean all surfaces, equipment, and materials by wiping them with DNA AWAY™ (Thermo Fisher Scientific) and RNaseZap™ (Sigma-Aldrich, St. Louis, MO, USA). We cleaned the perfusion with 50 mL of 70% ethanol. After the electrophysiological recording, we centered the pipette on the soma and applied a constant small negative pressure to start extracting the cytosol. This helped attract the nucleus to the tip of the pipette. We maintained the negative pressure and slowly retracted the pipette while monitoring the pipette seal. Once the nucleus was visible on the pipette tip, we increased the speed to remove the pipette from the slice. We then removed the pipette containing the internal solution, cytosol, and nucleus from the pipette holder and expelled its contents into a 0.2-mL tight-lock PCR tube (TubeOne, StarLab, Hamburg, Germany). The tube contained 2 µL of lysis buffer consisting of 0.8% Triton X-100 (Sigma-Aldrich) and 1 U/µL RNase inhibitor (Takara, Kyoto, Japan). The internal solution comprised the following components: 110 mM K-gluconate (Sigma-Aldrich), 4 mM KCl solution, RNase-free (Invitrogen), 10 mM HEPES solution (Sigma-Aldrich), 1 mM ATP-Mg (Sigma-Aldrich), 0.3 mM GTP-Na (Sigma-Aldrich), 10 mM sodium phosphocreatine (Sigma-Aldrich), 0.2 mM EGTA (Sigma-Aldrich), 20 µg/mL RNA-grade glycogen solution (Thermo Fisher Scientific), and 0.5 U/µL RNase inhibitor (Takara). We then spun down the resultant sample (approximately 4.0 µL) for 2 s and placed it on dry ice. Finally, we stored the sample at −80°C until in-tube reverse transcription.

cDNA amplification and library construction

To prepare the libraries, we used a protocol based on the SmartSeq2 procedure (Hennig et al., 2018; Picelli et al., 2014). Briefly, cDNA was generated and amplified by 24 PCR cycles for all samples, including the negative controls. We augmented the cDNA to add indexes and adapter sequences, pooled them equimolarly, and then sequenced our samples on the Illumina MiSeq platform (Illumina, San Diego, CA, USA) with a 50 single-end read mode. Each sample was sequenced to around 1–2 million reads.

Sequencing data processing

The study used 66-base paired-end reads that were aligned to GRCh38 using the annotation GTF file (GRCh38_r93) retrieved from Ensembl. Sequence alignment was performed using STAR v2.7.11a (Dobin et al., 2013). The default parameters were used with the following arguments: --soloType SmartSeq --soloUMIdedup Exact --soloStrand Unstranded --soloFeatures GeneFull. Full gene counts, including intron and exon counts, produced by STAR were used to calculate the TPM values, which were used for subsequent analyses.

Identification of Pvalb neurons based on single-nucleus transcriptomics analysis

The transcriptomic data of individual cells were uploaded to the Allen Institute neuron type identification system to categorize neocortex neuron types by the genes expressed (Allen Institute for Brain Science, 2024, MapMyCells, available from https://knowledge.brain-map.org/mapmycells/process/ (RRID:SCR_024672)), allowing Pvalb neuron identification in cells in which PVALB/Pvalb expression was below the detection limit. This algorithm uses a set of marker genes to predict the cluster/supertype of the cells based on their corresponding single-nucleus dataset.

For human samples, the Seattle Alzheimer's Disease Brain Cell Atlas reference taxonomy was used with the Deep Generative Mapping algorithm, whereas mouse cells were classified using the 10X Whole Mouse Brain reference taxonomy with the hierarchical mapping algorithm. Only cells classified as Pvalb neurons at $p > 0.9$ were included in further analysis (supertype_bootstrapping_probability). Our single-nucleus gene expression data from human

samples highly correlated with the Allen Institute high-resolution database of specific Pvalb neuron subtypes (subclass correlation coefficient > 0.5 with the 10X Whole Human Brain dataset using the correlation mapping algorithm).

Results

We investigated the electrophysiological properties of fast-spiking basket cells in layer 2/3 of the human neocortex using somatic whole-cell patch-clamp recordings. Cells were identified based on narrow action potentials, narrow axonal current and minimal spike frequency adaptation. *Post hoc* visualization via biocytin labeling confirmed the morphology and Pvalb expression through immunohistochemistry or patch-sequencing (Fig 1A1-A2). Recordings were primarily obtained from frontal and temporal cortices, with additional data from other neocortical regions. For interspecies comparison, fast-spiking Pvalb neurons were also recorded in the frontal and parietal cortex of pvCre-tdTomato mice (Fig 1A3-A4).

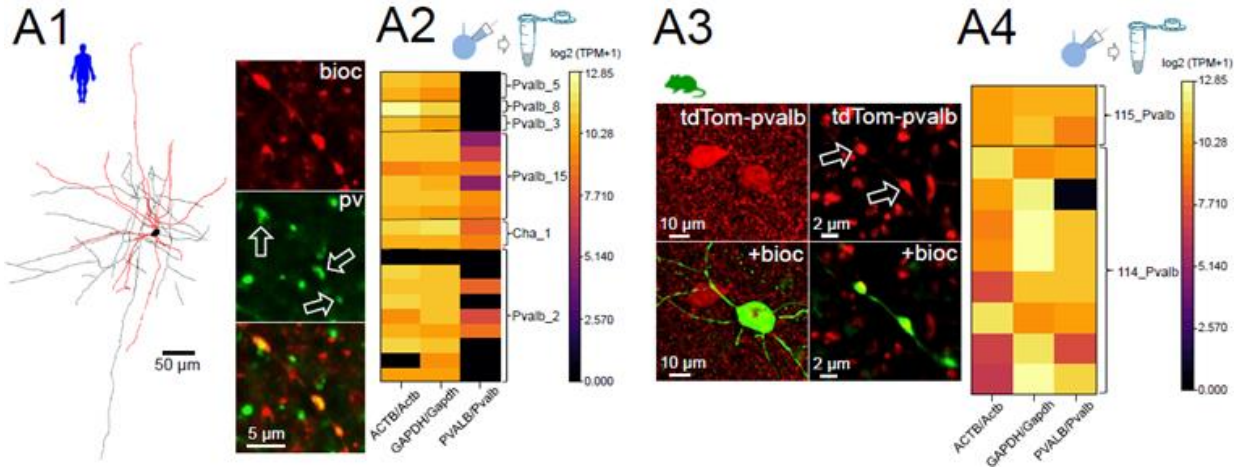

Figure 1. (A) Identification of Pvalb interneurons in human and mouse neocortex layer 2/3. (A1) Left: Most of the recorded cells were filled with biocytin for post hoc visualization of their structure with streptavidin fluorophore. The cells were analyzed for the neuronal marker parvalbumin by fluorescence immunohistochemistry. Left: Visualized human Pvalb neuron after biocytin filling. Right: Confocal fluorescence images showing Pvalb-immunopositive axon boutons of the same cell. (A2) Alternatively, cells were analyzed for Pvalb mRNAs by patch sequencing. The ordinate shows Pvalb neuron subtypes identified by their gene expression using the Allen Institute Neocortical Neuron Type Identification System. (A3) Mouse Pvalb neurons were identified using a genetic fluorophore in Pvalb neurons. (A4) Cells were patch-sequenced and analyzed for Pvalb expression. The ordinate shows the mouse Pvalb neuron subtypes as identified by the Allen Institute Neuron Type Identification System.

Somatic HCN Channels speed up Spike Generation (Research study I)

This study compared the electrophysiological properties of fast-spiking GABAergic basket cells in the human and mouse neocortex. Human Pvalb basket cells exhibit strong somatic HCN channel activity, which is either absent or weak in rodents. HCN channels have been shown to depolarize the resting membrane potential, accelerate membrane potential dynamics, and reduce the delay between excitatory postsynaptic potentials (EPSPs) and action potential generation. Human, but not mouse cells, show a distinctive somatic sag potential characteristic of HCN channel activation, confirmed through pharmacological blockade experiments. By using immunofluorescence staining, it was found that human Pvalb basket cells abundantly express HCN1 and HCN2 channels in their soma membrane, whereas these channels are sparse in mouse basket cell somata. These differences enable human cells to achieve input-output performance comparable to that of mouse cells, despite their inherently slower baseline dynamics. The findings of the study indicate that somatic HCN channels significantly enhance the speed of membrane potential kinetics in human basket cells, as also supported by computational modelling.

Human, but not mouse basket cells have a robust HCN-mediated sag potential

Whole-cell current-clamp recordings from human fast spiking cell somas revealed a significant membrane potential drop at the onset of hyperpolarization from -70 mV to -90 mV (step duration: 250-500 ms) (Fig. 2A). In contrast, similar voltage steps did not elicit a significant somatic hyperpolarization-induced membrane potential sag in the majority of mouse fast spiking Pvalb cells (Fig. 2B). The voltage sag in human fast-spiking interneurons was blocked by the HCN channel antagonist ZD7288 (10 μM) ($P < 0.001$ using Wilcoxon signed-rank test, $n = 24$). This was measured by changing the membrane potential from −70 mV to −90 mV (Fig. 2C). Furthermore, drug wash-in (over a period of 3–5 minutes) was associated with a significant hyperpolarising shift from a median resting potential (Em) of −62.0 mV (IQR, −55 to −67.25 mV) to −68.75 mV (IQR, −56.50 to −74.25 mV), for a median shift of −6.75 mV (IQR, −2.8 to 9.0 mV; $P = 0.004$ by Wilcoxon signed-rank test) ($n = 22$). In contrast, the treatment of mouse fast-spiking Pvalb cells with ZD7288 ($n = 11$) did not change Em (median before treatment = −71 mV; IQR, −54 to −74 mV; median after treatment = −72 mV; IQR, −60 to −78 mV; $P = 0.148$ by Wilcoxon signed-rank

test). These results suggest somatic HCN expression is a distinguishing feature of human Pvalb interneurons. These results are in line with the findings of previous studies showing axonal HCN expression in rodent neocortical Pvalb cells (Albertson et al., 2017; Goldberg et al., 2011; Yang et al., 2018).

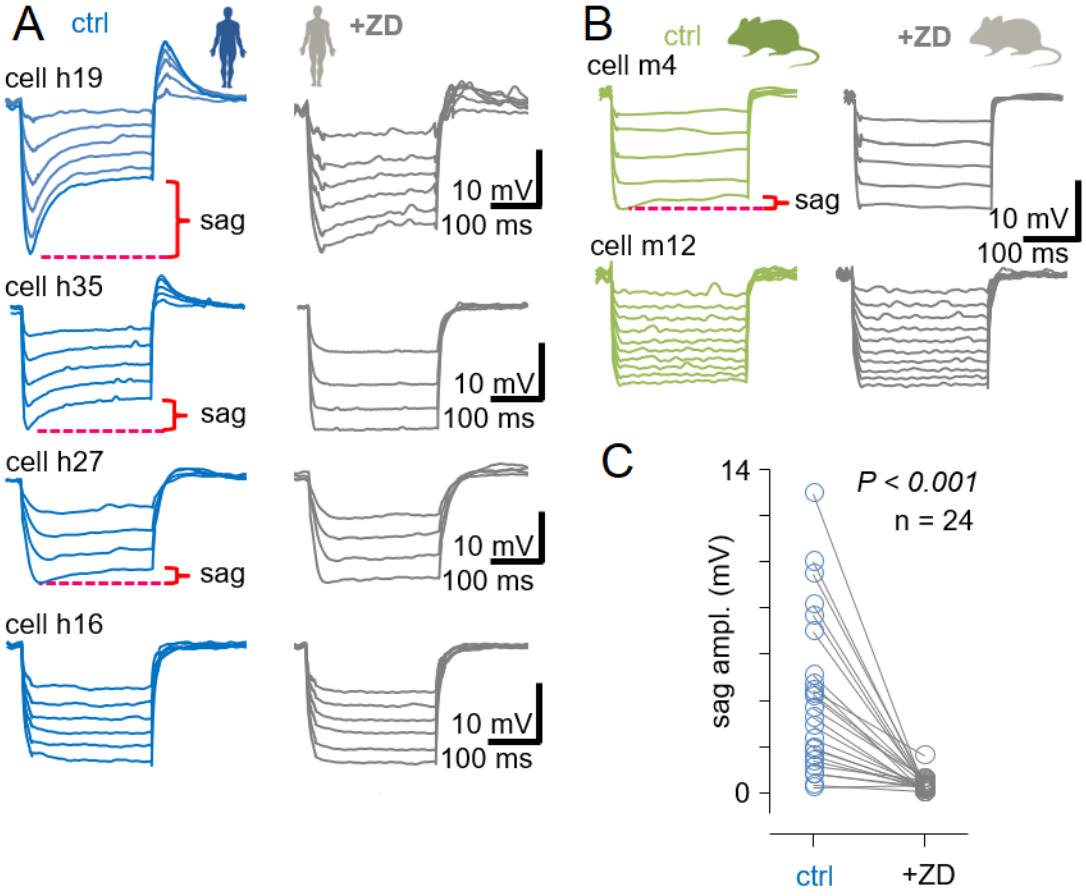

Figure 2. Human, but not mouse fast-spiking basket cells show a strong somatic HCN channel-mediated sag potential. (A) Somatic sag potentials recorded from human fast-spiking Pvalb interneurons, membrane potential responses to hyperpolarising current steps delivered from −70 mV. The traces that reach a peak potential of -90 mV show the hyperpolarisation-activated sag potential in three of the four sample neurons in normal conditions (blue traces). Gray traces show the same cells' responses when they were exposed to ZD7288. Red markings indicate the amplitude of the sag potential. (B) Membrane potential traces from two types of mouse Pvalb neurons. The green traces show the control conditions and the gray traces show the conditions where the neurons were exposed to ZD7288. Note that Cell m4 shows a small sag. (C) Summary of ZD7288 effect on sag amplitude recorded from 24 human Pvalb cells.

We then examined the potential associations between this hyperpolarisation-evoked sag and the patients' clinicodemographic data. Our findings revealed no significant association between sag

amplitude and age from 20 to 82 years (R = 0.139, P = 0.25 by Pearson's correlation for sag amplitude versus age, n = 72) (Fig. 3A). The cortical area also did not show a correlation with sag amplitude. A robust sag was identified in fast-spiking cells from the frontal cortex (n = 35), the temporal cortex (n = 24), and other cortical regions (n = 13), including the occipital, parietal, and paraventricular areas (P = 0.13, using analysis of variance (ANOVA) on ranks) (Fig. 3B). Furthermore, sag amplitude exhibited no significant differences between sexes (female n = 46, male n = 26, P = 0.34, Mann–Whitney U test) or between left and right cerebral hemispheres (left n = 20, right n = 49, P = 0.43 using Mann–Whitney U test). Sag amplitudes did not vary according to primary diagnosis for neurosurgical procedures, with robust sag amplitudes observed in tissues resected for tumour (n = 47), hydrocephalus (n = 14), aneurysm (n = 6), and other conditions (n = 5) (P = 0.35 using ANOVA on ranks) (Fig. 3C). These findings suggest the presence of a constitutive and universal sag in the soma of human fast-spiking cortical basket cells of all ages.

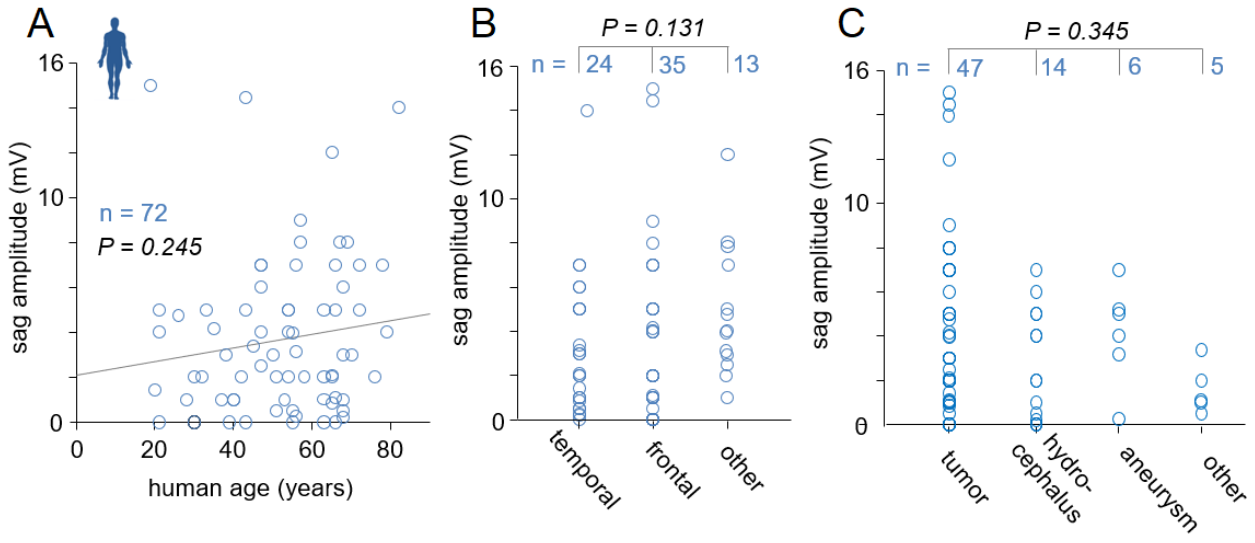

Figure 3. The correlation between sag amplitude and the clinical and demographic data of the patient. (A) The sag potential in human fast-spiking basket cells is seen at all ages from 20 to 82 years. (B) There is also no correlation between sag amplitude and brain area and (C) diagnoses.

HCN channels are expressed on the somata of human cells, but not in mouse cells

Double immunofluorescence staining was performed with parvalbumin (Pvalb) and HCN1 or HCN2 antibodies. Pvalb, as a marker protein is widely used for identifying fast-spiking interneurons in the neocortex (Hu et al., 2014; Krienen et al., 2020; Rudy et al., 2011). We studied HCN1 or HCN2, the two dominant HCN channel isoforms. By using confocal microscopy, we observed strong HCN1 and HCN2 immunoreactivity on the soma membrane of human but not mouse Pvalb cells (Fig. 4A-D). Subsequently, a quantitative analysis was conducted on HCN and cell marker immunoreactivity, using confocal images based on radial immunofluorescence intensity measurement lines (Fig. 4A1-D1). Each line quantified Pvalb cell-associated fluorophore emission from immunolabeled HCN1 or HCN2 channels over a distance of 8 μm from the cell soma centre to the extracellular space (Fig. 4A2-D2). A total of 2340 lines were analysed from 390 human and mouse Pvalb cells. Human fast-spiking interneurons exhibited intense Pvalb immunofluorescence in the soma, whereas mouse cells exhibited intense somatic emission from tdTomato, the transgenic fluorophore driven by the Pvalb promoter. In both cell types, the intracellular emission was found to originate from the nucleus and cytoplasm. In line with the analysis of the membrane, the plasma membrane appeared as a narrow zone in which the Pvalb (or tdTomato) fluorescence signal rapidly disappeared (Fig. 4A2, A3, D2 and D3). The immunofluorescence intensities of the HCN1 and HCN2 channels, as well as the intracellular marker signal, were measured and subsequently quantified in the cytoplasm, at the somatic membrane zone, and in the extracellular space (defined by the absence of intracellular signal). The measurement process is illustrated in Figure 4A3-D3. Radial pattern line analysis of HCN1 and HCN2 expression by human Pvalb cells is demonstrated in Fig. 4A1–A3 and B1–B3, whereas the results for mice are presented in Fig. 4C1–2C3 and D1–2D3.

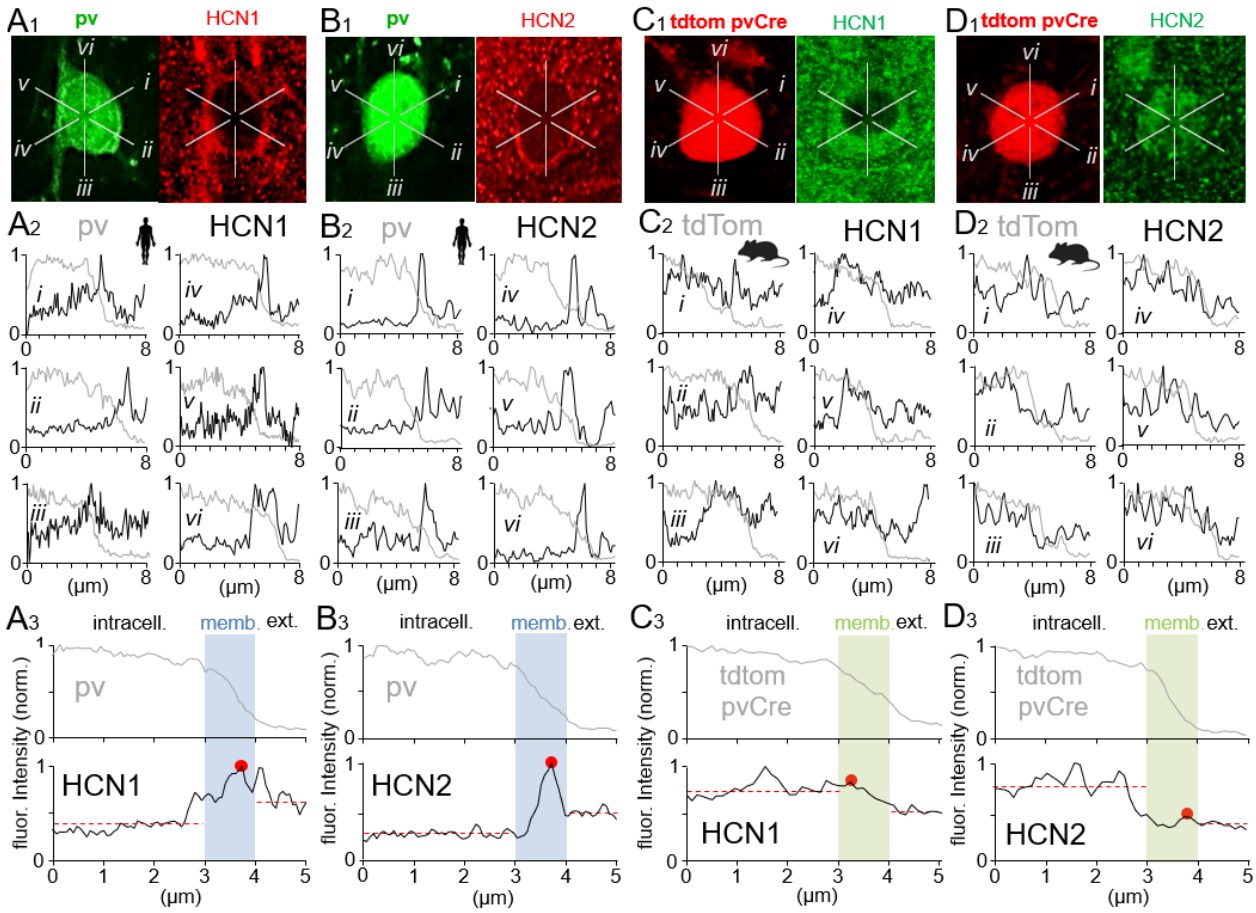

Figure 4. HCN1 and HCN2 channel localization at somatic cell membrane of human is stronger than mouse Pvalb cells. Panels A-D present analogous experiments in human with HCN1 (A1–3) and HCN2 (B1–3), and mouse with HCN1 (C1–3) and HCN2 (D1–3) stainings. (A1, B1) Confocal immunofluorescence image of a basket cell in human neocortex L2/3 with Pvalb labeled using Alexa 488 as the fluorophore and HCN1 and HCN2 using Cy3 as the fluorophore. Immunofluorescence intensity was measured along six 8-µm long radial lines (i to vi). (A2, B2) Immunofluorescence intensity (ordinate) from Pvalb (gray line) and HCN1/HCN2 (black line) measured along lines i to vi starting from the cell soma center (left) and crossing the soma plasma membrane to the extracellular space (right). (A3, B3) Average Pvalb (top) and HCN1/HCN2 (bottom) immunofluorescence signals along the six measurement lines for the cell shown in A,B1–2. Lines are aligned to the midpoint of the plasma membrane zone, which is marked by a shaded blue background. The plasma membrane zone is defined as a 1 µm-wide region at the point where the plasma membrane signal descends. (C1, D1) Confocal fluorescence image of a Pvalb-positive (pvCre-tdTom) mouse basket cell immunostained for HCN1 and HCN2 using Alexa 488 as the fluorophore. (C2, D2) Line analysis of a mouse Pvalb cell expressing tdTomato and also immunostained for HCN1/HCN2 showing the absence of a clear HCN1/HCN2 immunofluorescence peak within the plasma membrane zone. (C3, D3) Averaged line analyses of Pvalb-associated fluorescent signals (top) and HCN1/HCN2 immunofluorescence (bottom) for the cell shown in C,D1-2. The plasma membrane zone is indicated by green background.

The immunofluorescence intensity of human Pvalb cell HCN1 (in units) increased 3.42-fold (IQR, 2.56- to 4.78-fold) at the cell soma membrane zone in comparison to the extracellular space, and a 2.25-fold (IQR, 1.77- to 2.65-fold) higher than that in the cell soma intracellular space (n = 720 lines in 120 cells sampled from 8 patient tissue samples, 15 cells per sample) (Fig. 5A). In a similar manner, HCN2 immunofluorescence intensity was 5.22-fold (IQR, 4.01- to 6.56-fold) higher at the membrane zone than that in the extracellular space and 2.74-fold (IQR, 2.42- to 3.18-fold) higher than that in the soma intracellular space (n = 540 lines in 90 cells sampled from 6 patient tissue samples, 15 cells per sample) (Fig. 5B).

In contrast, mouse Pvalb cells exhibited increased HCN1 and HCN2 immunofluorescence signals at the soma plasma membrane in comparison to those in the extracellular space (HCN1 median = 1.51-fold; IQR, 1.41- to 1.68-fold; HCN2 median = 1.58-fold; IQR, 1.43- to 1.83-fold; n = 540 and 540 lines in 90 cells sampled from 6 mouse tissue samples, 15 cells per sample). However, the intensities observed in the mouse soma membrane (compared to the extracellular) were significantly weaker than those measured in the human soma membrane zone (n = 90 and 120, $P < 0.001$ and < 0.001, respectively, using the Mann–Whitney U test) (Fig. 5A-B). Mouse Pvalb cells also exhibited stronger HCN1 and HCN2 signals in the somatic intracellular space than human Pvalb cells. The plasma membrane intensity of HCN1 and HCN2 emission reached 0.70-fold (IQR, 0. 65- to 0.75-fold) and 0.63-fold (IQR, 0.56- to 0.73-fold), respectively, of that of the intracellular somatic space (Fig. 5A-B).

As illustrated in Figure 5C, statistical analyses were performed to compare the immunofluorescence intensities of HCN1 and HCN2 between species, both within the membrane and extracellular space. Using the analysis of variance (ANOVA) on ranks with Dunn's post hoc pairwise test, a statistically significant difference ($P < 0.001$) was identified between species for membrane versus extracellular space measurements. A similar result was observed for membrane versus intracellular space measurements, where again a statistically significant difference ($P < 0.001$) was identified between species using the same statistical tests.

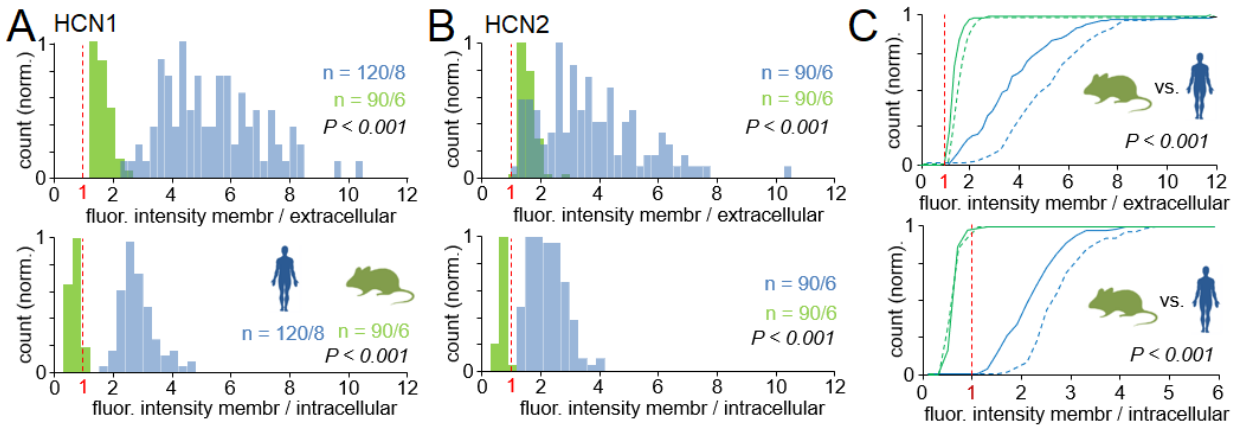

Figure 5. Histograms summarizing HCN1 and HCN2 immunofluorescence intensity levels at the soma plasma membrane for 390 Pvalb cells. The bin size has been set to 0.25. (A) The top image displays the HCN1 immunofluorescence intensity at the plasma membrane zone in comparison to the extracellular space for human (blue bars) and mouse Pvalb-expressing basket cells (green). The bottom image depicts the HCN1 immunofluorescence intensity at the soma plasma membrane compared to the intracellular space. (B) The top image illustrates the HCN2 immunofluorescence intensity ratio at the cell membrane zone versus the extracellular space for human (blue bars) and mouse Pvalb-expressing basket cells (green). The bottom image provides additional information on HCN2 immunofluorescence intensity at the cell membrane versus intracellular space. The ratio of 1 at the abscissa is indicated in red and with a vertical dotted line. (C) HCN1 and HCN2 immunofluorescence localization results for Pvalb cells for both species. The top image shows a summary of the measurements of the membrane versus extracellular site in human (blue line) and mouse (green line) for HCN1 (solid line) and HCN2 (dotted line). The bottom image shows HCN1 and HCN2 immunofluorescence intensity measured at the cell membrane versus intracellular space.

In addition, the definition of the cell membrane zone used for analysing the immunofluorescence intensity of HCN1 and HCN2 was validated by examining the localisation of Kv3.1 potassium channels. It is well established that these channels are also enriched at the somatic membrane of fast-spiking Pvalb neurons (Goldberg et al., 2011; Jing Du, 1996; T.F. Freund, 1996). As illustrated in Figures 6 A and B, immunoreactivity patterns for Kv3.1 were determined based on fluorescence intensity line analysis of human and mouse Pvalb cells, respectively. In both human and mouse Pvalb cells, Kv3.1 immunofluorescence was localised to a narrow zone at the edge of the intracellular Pvalb fluorescence signal.

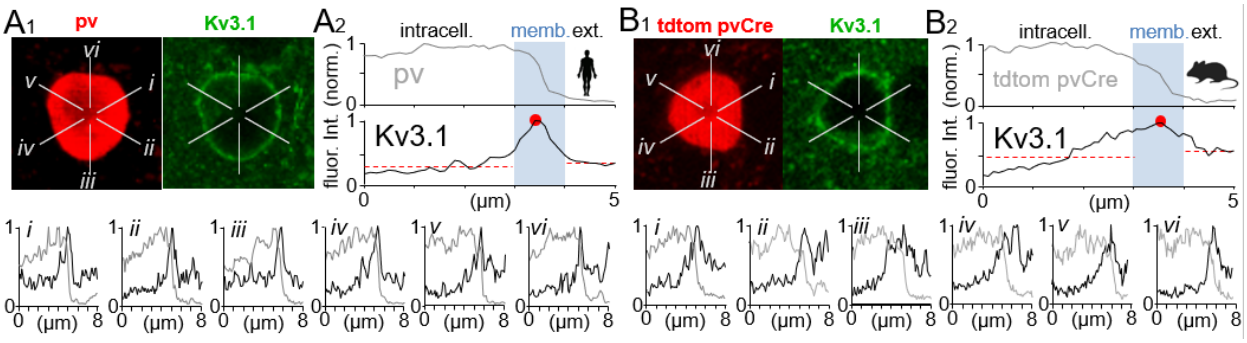

Figure 6. The plasma membrane zone was verified in human (A) and mouse (B) images by immunofluorescence labeling for Kv3.1 potassium channels, which are characteristically enriched at the somatic membrane. (A1) Top: Confocal immunofluorescence image of Pvalb immunoreactivity in a human L2/3 cell (where Cy3 is the fluorophore), costained for Kv3.1 (where Alexa 488 is the fluorophore). Immunofluorescence intensity was measured along radial lines i-vi. Bottom: Line analysis of lines i-vi for Pvalb and Kv3.1 immunofluorescence. (A2) Average of line analyses from A1. (B1) Top: Confocal fluorescence image of a mouse basket cell showing fluorescence signals from Pvalb (pvCre-tdTomato) and Kv3.1 (Alexa Fluor 488). Also shown are radially patterned intensity measurement lines i-vi. The bottom image displays the line analyses (i-vi) and B2) average of aligned fluorescence intensity traces, showing the Kv3.1 signal peak at the plasma membrane zone.

dSTORM super-resolution microscopy reveals HCN channels

To provide further evidence that the immunofluorescence signals of HCN originate from the membrane surface, the localisation of the immunofluorescence was investigated in selected tissue sections from humans and mice using appropriate antibodies and the dSTORM super-resolution technique, which achieves a spatial resolution of less than 0.1 µm for fluorophore signal analysis. These dSTORM immunofluorescence images showed antibody binding (fluorescent signals) concentrated in a narrow layer around the cell body of human Pvalb neurons and a clear contrast between apparent cell membrane areas and both extra- and intracellular spaces for HCN1 (Fig. 7A1-A2), HCN2 (Fig. 7B1-B2) and Kv3.1 (Fig. 7C1-C2). Nevertheless, similar images of mouse Pvalb cells showed areas of punctate HCN1 and HCN2 fluorophore signal distributed throughout the cell body rather than at the soma membrane, likely reflecting clusters within the cytoplasm (Varga et al., 2008). Figures 7 D and E show dSTORM images of typical mouse Pvalb cells in which there is no clear immunofluorescence signal contrast between the apparent membrane areas and both the extra- and intracellular spaces for HCN1 (Fig. 7D1-D2) and HCN2 (Fig. 7E1-E2). By contrast, dSTORM imaging of Kv3.1 immunoreactivity in mouse tissue revealed fluorophore molecules concentrated in a narrow layer around the Pvalb cell body in apparent

extracellular membrane spaces (Fig. 7F1-F2), similar to Kv3.1 immunoreactivity in human Pvalb cells.

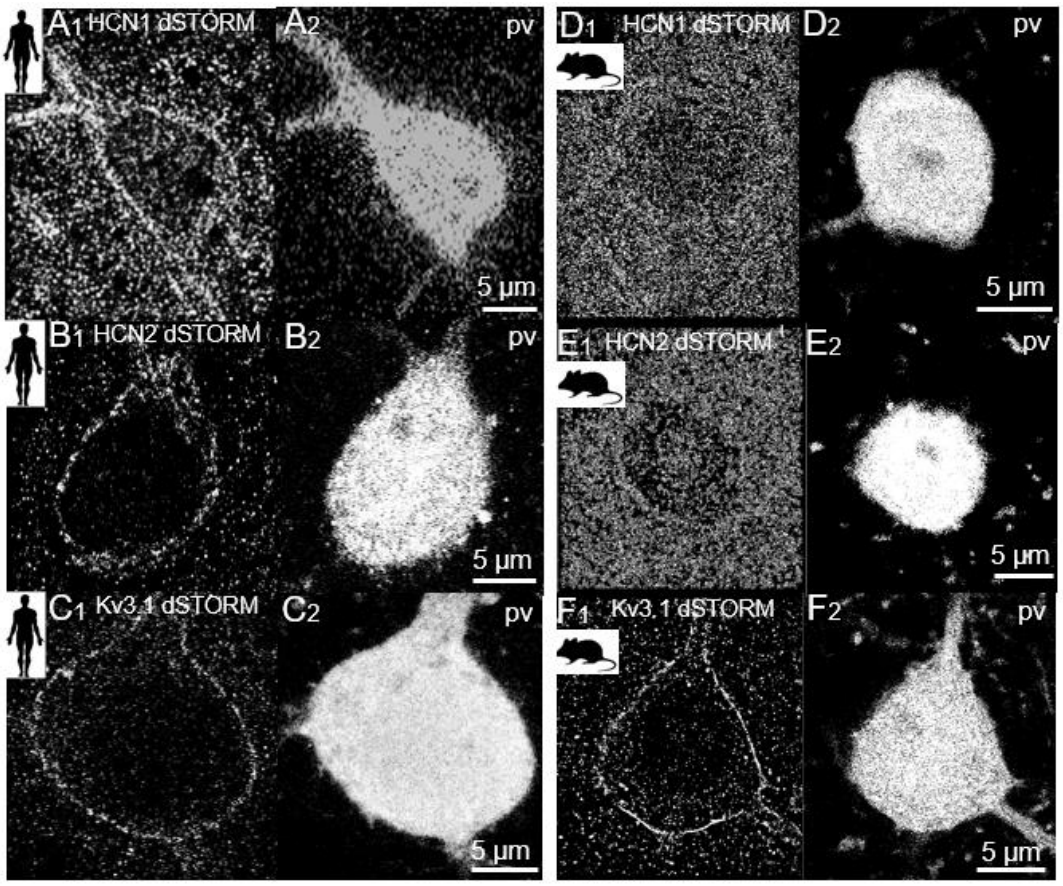

Figure 7. Somatic HCN1, HCN2 and Kv3.1 channels in human and mouse Pvalb interneurons visualised by dSTORM super-resolution immunofluorescence microscopy. (A-C) dSTORM super-resolution images showing high-resolution immunofluorescence labelling of HCN1, HCN2 and Kv3.1 channels in human Pvalb cells. Pvalb immunoreactivity is shown in paired confocal images. (A) dSTORM image of HCN1 immunolabeling (A1) using Alexa 647 as fluorophore paired with confocal image of Pvalb immunoreactivity (A2) using Cy3 as fluorophore. (B) dSTORM image of HCN2 immunolabel (B1) using Alexa 647 as fluorophore paired with confocal image of Pvalb immunoreactivity (B2) using Cy3 as fluorophore. (C) dSTORM image of Kv3.1 potassium channel immunostaining using CF568 fluorophore (C1) paired with confocal image of Pvalb immunoreactivity using Alexa 488 fluorophore (C2). (D-E) Mouse Pvalb cell with weak or absent HCN1 or HCN2 immunofluorescence at the cell soma membrane. dSTORM images of HCN1 (D1) and HCN2 (E1) immunoreactivity using Alexa 647 fluorophore are paired with confocal images of Pvalb-associated fluorescence (tdTomato) (D2 and E2). (F) dSTORM image of Kv3.1 immunolabel (F1) with Alexa 647 fluorophore coupled with confocal image of Pvalb-associated intracellular fluorescent signal (F2).

The Model Cell Shows the Significance of the HCN Channel in Human Neurons

In order to provide theoretical support for the functional importance of HCN channel activity in human cortical basket cells, a model neuron was constructed with a somatic compartment, primary dendrite, and axon (Ratkai et al., 2021). The axonal and dendritic cable compartments were designed with a length of 200 μm and a diameter of 1.2 μm. The model cell incorporated a persistent non-inactivating leak current in all compartments, along with standard Hodgkin–Huxley-type spike-generating Na^+ and K^+ conductances, and a slowly activating M-type K^+ current in axonal and somatic compartments. The M-type K^+ current exhibited a reproducible gradual increase in interspike interval, analogous to that observed in biological neurons, during positive current steps up to +40 pA (Fig. 8A1 and 8B1). It was also found that somatic and dendritic compartments contained HCN currents and inward-rectifying K^+ currents (Kir) (Hammack et al., 2007; Hazra et al., 2011). The Kir conductance replicated the decreased input resistance that was observed during the application of hyperpolarising currents from −20 to −100 pA in the presence of ZD7288 (Fig. 8A2 and 8B2). The assumption was made that 65% of the sag amplitude in the soma was mediated by local HCN channels, as indicated via our outside-out experiments, whereas the remaining 35% was generated in the model by conductance of HCN channels (gHCN) localized at the primary dendrite. The model parameters were set based on the real responses of sample cell h35 (Fig. 8A1–8A3), a fast-spiking basket cell showing a 5-mV sag during hyperpolarisation to −90 mV from -70 mV. These responses were then simulated (Fig. 8B1–8B3) in order to obtain current–voltage relationships (both passive and active) as well as sag amplitude, kinetics, and voltage dependence. These were matched to the responses of cell h35 under both baseline conditions and in the presence of ZD7288. Indeed, these simulations reproduced the membrane potential changes, firing responses to depolarizing current steps, sag amplitude voltage dependence, and rebound firing following hyperpolarizing steps observed in cell h35 (Fig. 8A1 and 8B1). The simulation demonstrated that the activation of gHCN, which is responsible for the somatic voltage sag as previously described, also results in a depolarising shift of Em by 5 mV (Fig. 8A1, 8B1, and 8C1–8C4). Subsequently, an investigation was conducted into the contribution of gHCN to spike generation by EPSC input, generated by a synaptic glutamatergic-type conductance (0.5 nS to 20 nS), at the soma. As with our dynamic clamp experiments, this generated

EPSPs to produce the shortest spike delay close to 3 ms (Fig. 8C). Large monosynaptic EPSCs with conductances between 5 and 15 nS have been reported in L2/3 human basket cells (Molnar et al., 2008; Szegedi et al., 2017; Szegedi et al., 2016), and the EPSP–spike responses evoked in this conductance range were sensitive to perisomatic gHCN. The simulation results demonstrated that perisomatic gHCN reduces the EPSC amplitude required to elicit spiking at the resting membrane potential (Fig. 8C) when gradually increased from 0 nS to partial somatic gHCN (50% of that measured in cell h35), physiological (100% of that measured from cell h35), and up to 150%. The effect of physiological HCN activity is indicated by the difference in response between Fig 8C1 (total absence of gHCN in cell h35) and Fig 8C3 (simulation replicating physiological gHCN as shown in Fig 8A1 and 8B1). Finally, it was found that the simulated EPSC-to-spike delay became progressively shorter as the somatic gHCN was increased from 0% to 50%, 100%, and 150% of the real somatic gHCN value at the soma of cell h35 (Fig. 8C1–8C4).

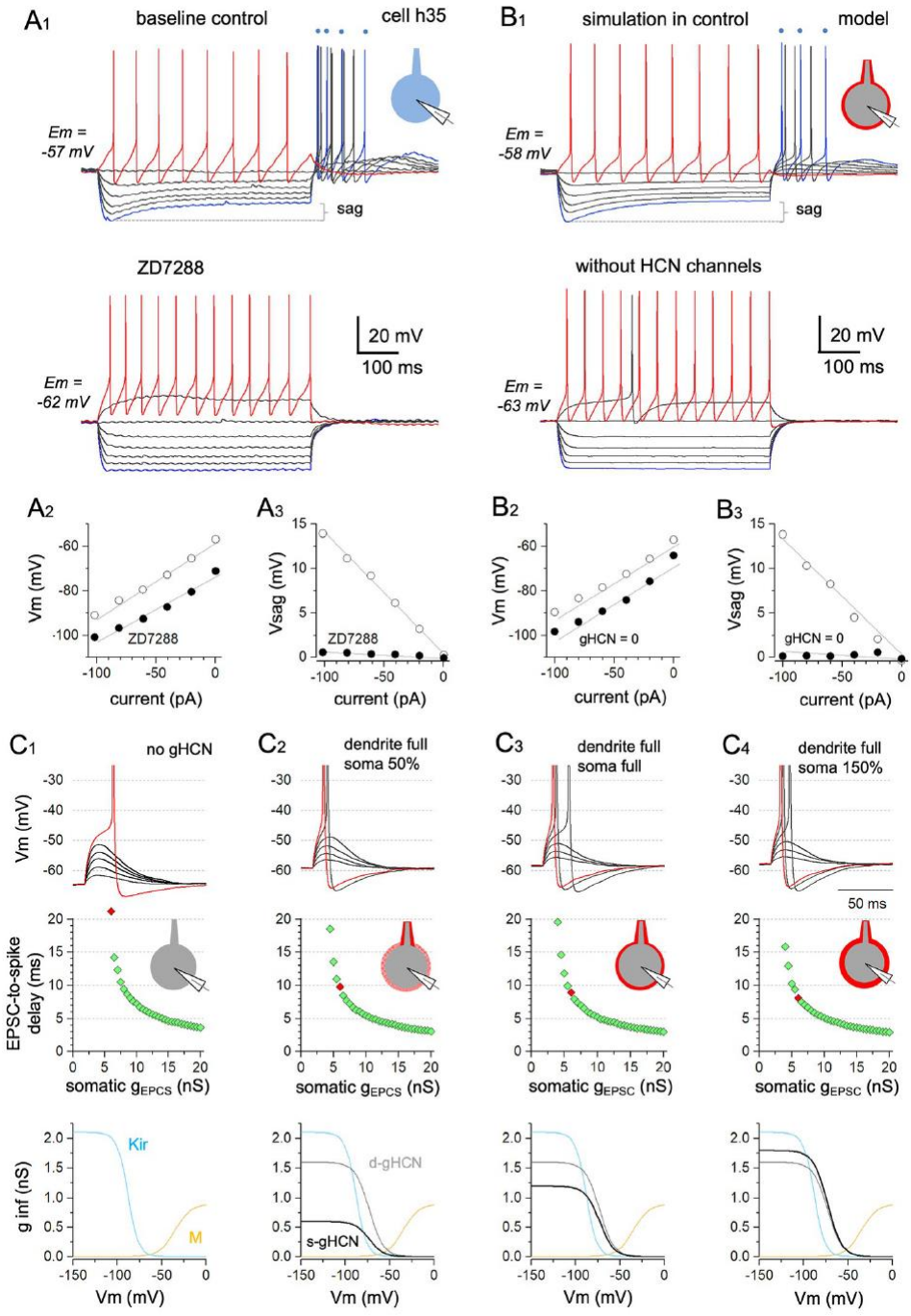

Figure 8. Computational modeling reveals how perisomatic HCN conductance modulates excitability and input–output function in human basket cells. (A) Electrophysiological recordings from human fast-spiking interneuron h35. (A1) Responses to 500-ms current steps from −100 pA (blue) to +20 pA (red) at resting membrane potential (Em = −57 mV); ZD7288 abolishes sag and rebound firing at Em = −62 mV (blue dots mark rebound spikes). Inset: schematic of whole-cell recording. (A2) Peak hyperpolarization (Vm) plotted against step amplitude before (open) and after ZD7288 (solid). (A3) Sag amplitude (Vsag) at baseline (open) and after ZD7288

(black) across increasing hyperpolarizing steps. (B) Biophysical model of h35 replicates sag and rebound (top); removing HCN abolishes both (bottom) and shifts Em negatively. Inset: model schematic. (B2) Peak Vm vs. current for soma and 200 µm dendrite with physiological gHCN (open) or gHCN = 0 nS (black). (B3) Sag amplitude with and without gHCN at soma and dendrite. (C1) EPSPs and EPSP-spikes at gHCN = 0. Top: EPSPs evoked by 1–6 nS EPSC at −62 mV; AP generated at 6 nS (red). Middle: Spike delay (EPSC-to-spike) plotted vs. gEPSC (0.5–20 nS); red dot = 6 nS. Inset: EPSC simulation schematic. Bottom: Activation curves for M-current (brown) and Kir (blue). (C2) Model with full dendritic and 50% somatic gHCN. Top: APs evoked at 5 and 6 nS EPSC (red) at Em = −59 mV. Middle: Spike delay vs. gEPSC (red dot = 6 nS). Bottom: M-, Kir-, and HCN activation curves for soma (black) and dendrite (gray). (C3) Model with full somatic and dendritic gHCN. Top: APs triggered at 6 nS (red) from Em = −58 mV. Middle: Spike delay vs. gEPSC; red dot = 6 nS.Bottom: Activation of M-, Kir-, and HCN currents with full gHCN in both compartments. (C4) Model with full dendritic and 150% somatic gHCN. Top: APs triggered at 6 nS (red) from Em = −57 mV.
Middle: Spike delay vs. gEPSC (red dot = 6 nS). Bottom: M-, Kir-, and HCN activation curves with enhanced somatic gHCN.

Kir Channels Regulate Subthreshold Excitability (Research study II)

While neurons in the mammalian brain are largely similar, species-specific specializations exist, particularly in the neocortex, which governs complex brain functions. In humans, neocortical inhibitory interneurons have higher excitability than in rodents due to reduced passive ion leakage. However, the role of voltage-gated ion channels in regulating human interneuron excitability remains unclear. In rodents, parvalbumin-expressing (Pvalb) neurons, rely on Kir potassium channels to regulate excitability by lowering membrane resistance below the action potential (AP) threshold (Platkiewicz & Brette, 2010). However, Kir channel function in human Pvalb neurons is largely unexplored. Using whole-cell patch-clamp recordings on human and mouse neocortex slices, we have found that Kir channels similarly control subthreshold membrane resistance in both species. Despite homo sapiens neurons having higher absolute resistance, Kir activation proportionally reduces input resistance in both humans and mice. Molecular and imaging analyses confirmed the presence of Kir3.1 and Kir3.2 channels in Pvalb neurons of both species. A computational model based on whole-cell recordings demonstrated how somatic Kir currents regulate input excitability in humans and mice.

The input rectification ratio is similar in human and mouse

To characterize the voltage dependence of input resistance, we applied square-pulse current steps (250-500 ms) at -70 mV in whole-cell current clamp mode to depolarize and hyperpolarize

the membrane potential with voltage steps. We then systematically measured somatic input resistance (Rin) at steps to -60 mV, -80 mV, and -90 mV. The results of the human and mouse cell recordings are illustrated in Fig. 9A1-4. A significant increase in Rin at all membrane potentials was observed in human neurons compared to mouse cells (MANOVA). The Rin values for human Pvalb neurons at -60 mV, -80 mV, and -90 mV were 291.9 ± 206.1 MΩ, 256.2 ± 183.4 MΩ, and 238.8 ± 171.8 MΩ, respectively (n = 34 cells). In the case of mouse Pvalb neurons, the Rin value was found to be 135.2 ± 53.3 MΩ at -60 mV, 115.5 ± 44.5 MΩ at -80 mV, and 103.1 ± 40.8 MΩ at -90 mV (n = 25) (Fig. 9B1). However, human and mouse Pvalb neurons exhibited a comparable proportional decrease in Rin following hyperpolarisation of the membrane potential. The Rin decreased in human Pvalb cells at -90 mV in comparison with Rin at -60 mV by 18.2%, and in mouse by 23.8%. This resulted in an input rectification ratio (rRin) of -90 mV/-60 mV of 0.77 ± 0.09 in human and 0.81 ± 0.08 in mouse, with no difference between the species (human n=32, mouse n=25, p=0.404, Mann-Whitney U test) (Fig. 9B2). Furthermore, Rin values in the same cells were tested by applying only negative current steps (up to -90 mV) at -60 mV to achieve a Rin drop of 19.3% with rRin -90mV/-70 mV of 0.81 ± 0.08 in human and 22.6% with rRin 90mV/-70 mV of 0.80 ± 0.07 in mouse (human n=31, mouse n=22, p=0.745, Mann-Whitney U test) (Fig. 9B2). Experiments were performed in the presence of an Ih current blocker (ZD, 10 μM) (Szegedi et al., 2023). The r_{Rin} did not show any association with the initial input resistance level in human cells (r=0.195, p=0.294, n=32) but mouse the cells with higher Rin also showed stronger Rin rectification r_{Rin} (r=-0.685, p<0.001, n=25) (Spearman correlation test) (Fig.9C). The results show that r_{Rin} is similar in human and mouse neurons despite the human neurons have consistently higher Rin. In addition, the input resistance drop by hyperpolarization was similar in human Pvalb neurons with high or low input resistance.

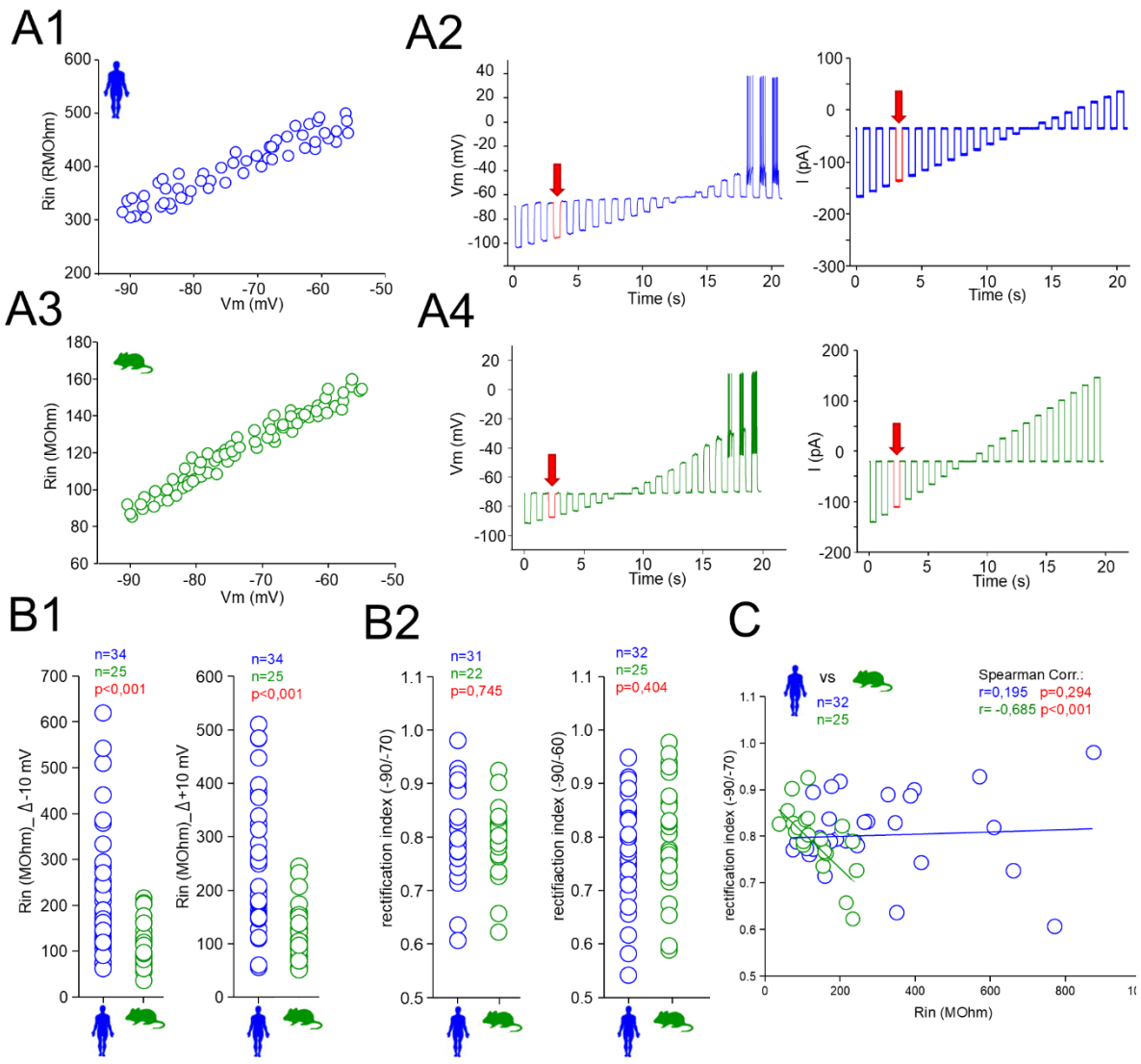

Figure 9. Human and mouse Pvalb neurons show an identical decrease in input excitability by membrane potential hyperpolarization, despite their different input resistance. (A1) Rin at different Vm in human cell. (A2) Left: Vm was depolarized or hyperpolarized to different Vm values at rest (-60 mV) by square pulse current steps (right). One step (-100 pA) is highlighted in red and indicated by an arrow to show the change in Vm. (A3) Rin at different Vm in a mouse Pvalb neuron. (A4) Vm responses to current pulses in a mouse neuron. (B1) Rin measured by -10 mV (left) or +10 mV (right) voltage steps at -60 mV membrane potential in human and mouse Pvalb neurons. (B2) The rectification ratio of Rin (rRin) measured at -60 mV resting potential for the ratio -90 mV/-70 mV (left) or at -70 mV for the ratio -90 mV/-60 mV Rin (right) are similar in human and mouse Pvalb neurons. (C) The rectification ratio of Pvalb cell input resistance (rRin) is not associated with input resistance (Rin) in human neurons, but shows a correlation in mouse.

Input Resistance Rectification is Generated by Kir Channels

We investigated the mechanism by which Kir channels regulate the input resistance associated with membrane potential hyperpolarisation in Pvalb neurons. The application of barium (Ba^{2+}, 100 µM) into the extracellular solution resulted in a reduction of the voltage dependence of Rin in both species: The rRin in human cells changed from 0.78 ± 0.02 (measured in the control baseline) to 0.88 ± 0.05 in the presence of Ba^{2+} (10 min wash-in) by suppression of the Rin drop in hyperpolarizing potentials (n = 7, p = 0.022, Wilcoxon test) (Fig. 10A1-2). A similar effect was observed in mouse Pvalb cells, where barium reduced rRin from 0.81 ± 0.02 (control baseline) to 0.90 ± 0.06 (n = 9, p = 0.009, Wilcoxon test) (Fig. 10C1-2). The effect of barium on rRin was found to be similar in human and mouse Pvalb neurons (p=0.673, Mann-Whitney U-test).

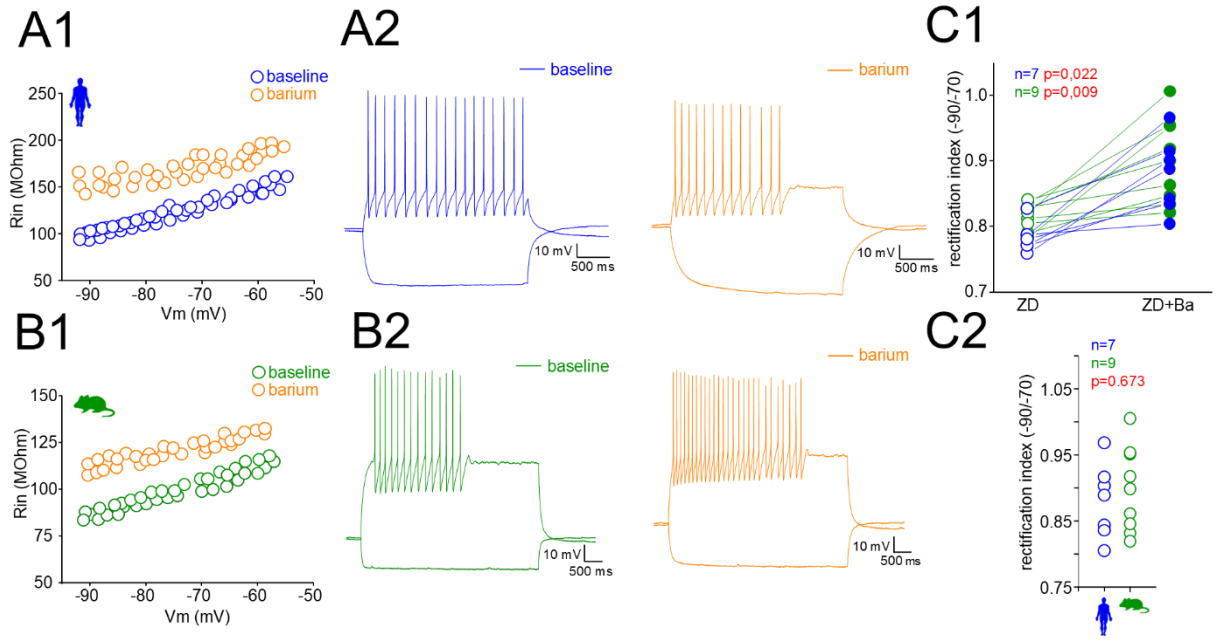

Figure 10. Pvalb cell input resistance drop by hyperpolarization is reduced by barium in human and mouse. (A) Extracellular barium (Ba^{2+}, 100 µM) suppresses the decrease of Rin by Vm hyperpolarization (A1) Input resistance (Rin) of human Pvalb neuron measured at different Vm under control baseline conditions and in the presence of extracellular Ba^{2+} (10 min). (A2) Vm steps in control baseline conditions and in the presence of Ba^{2+}. (B1) Mouse Pvalb neuron Rin at different Vm in control baseline conditions and with Ba^{2+}, and (B2) traces showing Vm steps in both conditions. (C1) Plot presenting Input rectification ratio (rRin) in human (blue) and mouse (green) Pvalb neurons under control baseline conditions and following exposure to Ba2+. rRin was similarly increased by Ba2+ in human and mouse. (C2) Plot shows rRin in the presence of Ba2+ in the human and mouse.

Human and mouse Pvalb neurons express Kir3.1 and Kir3.2 mRNA

We used patch-sequencing to examine mRNA levels (transcripts per million, TPM) for genes encoding Kir potassium channel types in human and mouse Pvalb neurons (Bakos et al., 2025). Amongst the 15 distinct KCNJ genes (KCNJ1-KCNJ16, except KCNJ7) that encode Kir potassium channels, the results of the patch-sequencing procedure in human cells (n=21) demonstrated that the mRNA levels for KCNJ3 and KCNJ6 genes, which encode Kir3.1 and Kir3.2, respectively, were the most robust (Fig. 11A). Furthermore, mRNA levels of Kir3.1 and Kir3.2 were also observed in mouse Pvalb-expressing neurons (n=10) in lower (for KCNJ3, p=0.012) or similar (KCNJ6, p=0.07) levels compared to human neurons. Furthermore, human and mouse Pvalb neurons exhibited divergent expression patterns for KCNJ4 (abundant in human, absent in mouse, encoding Kir2.3, p=0.018) and KCNJ9 (abundant in mouse, low in human, encoding Kir3.3, p=0.03). (One-way MANOVA with the post hoc Bonferroni test). The results of the mRNA levels in patch-sequenced human and mouse neurons are illustrated in Figure 11A. We analysed the mean transcriptomic profiles of Kir channel genes (KCNJ1-16, except KCNJ7) collected by the Allen Brain Institute in the human middle temporal gyrus (Bakken et al., 2021; Hodge et al., 2019). The aim was to compare how L2/3 Pvalb neurons differ between humans and mice. The database of averaged transcript levels (average of TMP) encompassing the various human and mouse Pvalb neuron subtypes, as determined by their gene expression patterns, revealed elevated mRNA levels of Kir3.1 and Kir 3.2 in both species (Fig. 11B), consistent with the mRNA analysis of our patch-sequenced neuron dataset (Fig. 11A). In human, the levels were higher for both genes ($p<0.001$ and $p<0.001$). In accordance with the patch-sequenced data, mRNA levels for KCNJ9 were found to be robust in mouse cells, while no expression was observed in human cells ($p<0.001$). Conversely, expression of KCNJ4 was observed in mouse cells but not in human cells ($p<0.001$). There was a significant disparity in TMP levels for KCNJ11-12 with higher levels detected in mouse cells ($p<0.001$). This finding was supported by a one-way MANOVA with a post hoc Bonferroni test, which revealed a difference between species in the patch-sequenced dataset (Fig. 11A). Both human and mouse Pvalb neurons exhibit the highest level of mRNA for Kir3.1 and Kir3.2 channel type genes, with these genes demonstrating stronger expression in human cells compared to mouse cells. However, mouse Pvalb neurons also express genes for additional Kir channel types. The total mRNA expression level (TPM for all Kir-type mRNAs summed up in a cell) in a neuron was not associated with the strength of the hyperpolarization-associated input

resistance drop (shown as rRin) (Fig. 11C) (human r:-0.346, p=0.147, n=19; mouse r=0.0714, p=0.906, n=7. Spearman correlation test). The total amount of KCNJ mRNAs (summed TPM) was not associated with cell absolute Rin (measured at –70 mV) (human r:-0.384, p=0.105, n=19; mouse r:-0.178, p=0.713, n=7).

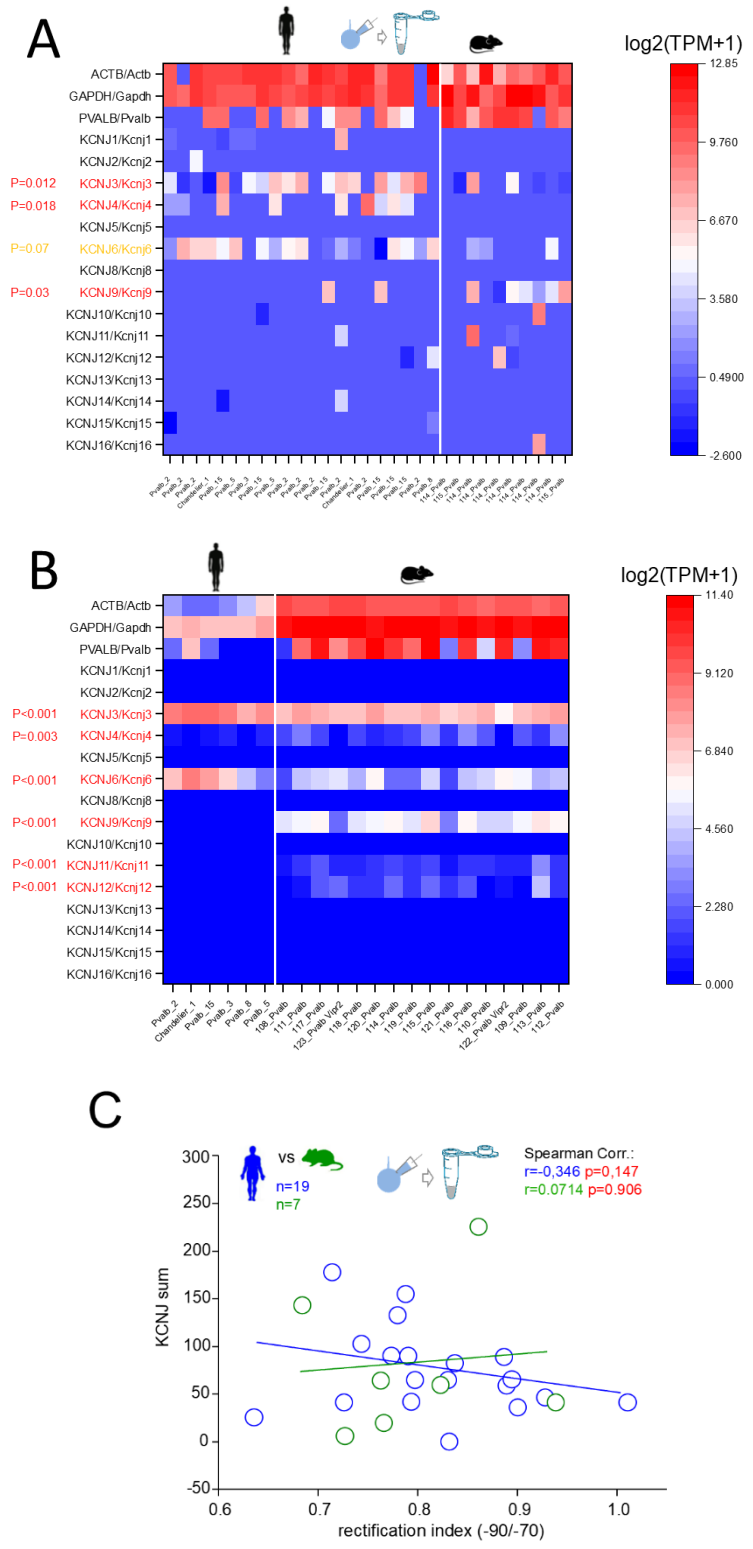

Figure 11. Human and mouse Pvalb neurons express high levels of Kir3.1 and Kir3.2 channel mRNA. (A) mRNA analysis of patch-sequenced human and mouse Pvalb neurons. Heatmap presents the mRNA levels (Transcript per million, TPM) in individual human (n = 21) and mouse (n = 10) neurons for genes KCNJ1-16 encoding (except

KCNJ7) Kir family channels, as well as housekeeping genes GAPDH/Gapdh and ACTB/Actb. Abscissa shows PVALB/Pvalb neurons with their subtype identity defined by neuron's gene expression pattern with Allen Institute neocortical neuron type identification system (PVALB/Pvalb neuron type identity codes shown in abscissa). Human and mouse cells show high mRNA levels for KCNJ3/Kcnj3 (Kir3.1) and KCNJ6/Kcnj6 (Kir3.2) mRNA with quantitatively higher levels in human. The human and mouse cells also differ in the expression levels of KCNJ4/Kcnj4 (Kir.3.2) and KCNJ9/Kcnj9 (Kir3.3). (B) Heatmap shows the Allen Institute data for KCNJ gene mRNA level (TPM) averages in the different PVALB/Pvalb neuron subtypes in human and mouse. mRNA levels are high in human and mouse cell types for KCNJ3/Kcnj3 and KCNJ6/Kcnj6. Mouse cells have higher expression for KCNJ4/Kcnj4, KCNJ9/Kcnj9, KCNJ11/Kcnj11, and KCNJ12/Kcnj12. (C) Plot shows lack of association between Kir channel gene mRNA level (TPM, summed for all KNCJ types) against rRin. rRin = 1 indicates lack of Kir channel effect.

The Kir3.1 and Kir3.2 proteins are expressed in human and mouse neurons

We studied the expression of the two most abundant Kir channels, Kir3.1 and Kir3.2 by using immunohistochemistry. The double immunofluorescence analysis for Pvalb with either Kir3.1 or Kir3.2, in parallel with confocal and STORM super-resolution fluorescence microscopy (Szegedi et al., 2023), revealed the localisation of Kir3.1 and Kir3.2 channel protein in the cells. Then, a quantitative analysis of Kir3.1 and Kir3.2 with Pvalb immunoreactivity (or TdTomato fluorescence in mouse) was performed using confocal images of human and mouse cells. This analysis was based on radial immunofluorescence intensity profiles (Fig. 12A–D). Each profile measured the emission intensity of Pvalb (or TdTomato in mice) alongside Kir3.1 or Kir3.2, spanning a distance of 5 μm from the center of the cell soma outward to 3 μm into the extracellular space (Fig. 12A1). In total, 24 radial lines per sample were analyzed for both human and mouse Pvalb-expressing cells. Human neurons exhibited Pvalb immunofluorescence within the soma, while mouse cells demonstrated intense somatic emission of tdTomato, the transgenic fluorophore driven by the Pvalb promoter. In the line analysis, the plasma membrane area manifested as a narrow zone where the Pvalb (or tdTomato) fluorescence signal rapidly decreased, as was the case in the line analysis in the previous project. Subsequent measurement and quantification of the immunofluorescence intensities of the labeled Kir3.1 and Kir3.2 channels were then conducted along the line with the Pvalb signal (Fig. 12A-D). The membrane localisation is clear in the line analysis of both human and mouse cells, with Kir3.1 fluorescence intensity exhibiting a peak at the site of immunofluorescence for Pvalb, as illustrated in Figures 12A2 and 12B2. Similar measurements for Kir3.2 immunofluorescence demonstrate its presence in the cell cytoplasm, as well as at the cell exterior. Furthermore, Kir3.2 immunofluorescence peak in line analyses was also

observed at the site where immunofluorescence of Pvalb rapidly disappears (Fig. 12C2 and 12D2). Line analysis of the immunofluorescence signal for Kir3.1 and Kir3.2 indicates the presence of these channel proteins within the Pvalb neuron soma membrane in both human and mouse. As illustrated in Figure 12E1-2, dSTORM immunofluorescence images are shown for Kir3.1 or Kir3.2 channel proteins in selected Pvalb neurons. The images demonstrate the localization of individual fluorophore molecule signals at the extracellular membrane.

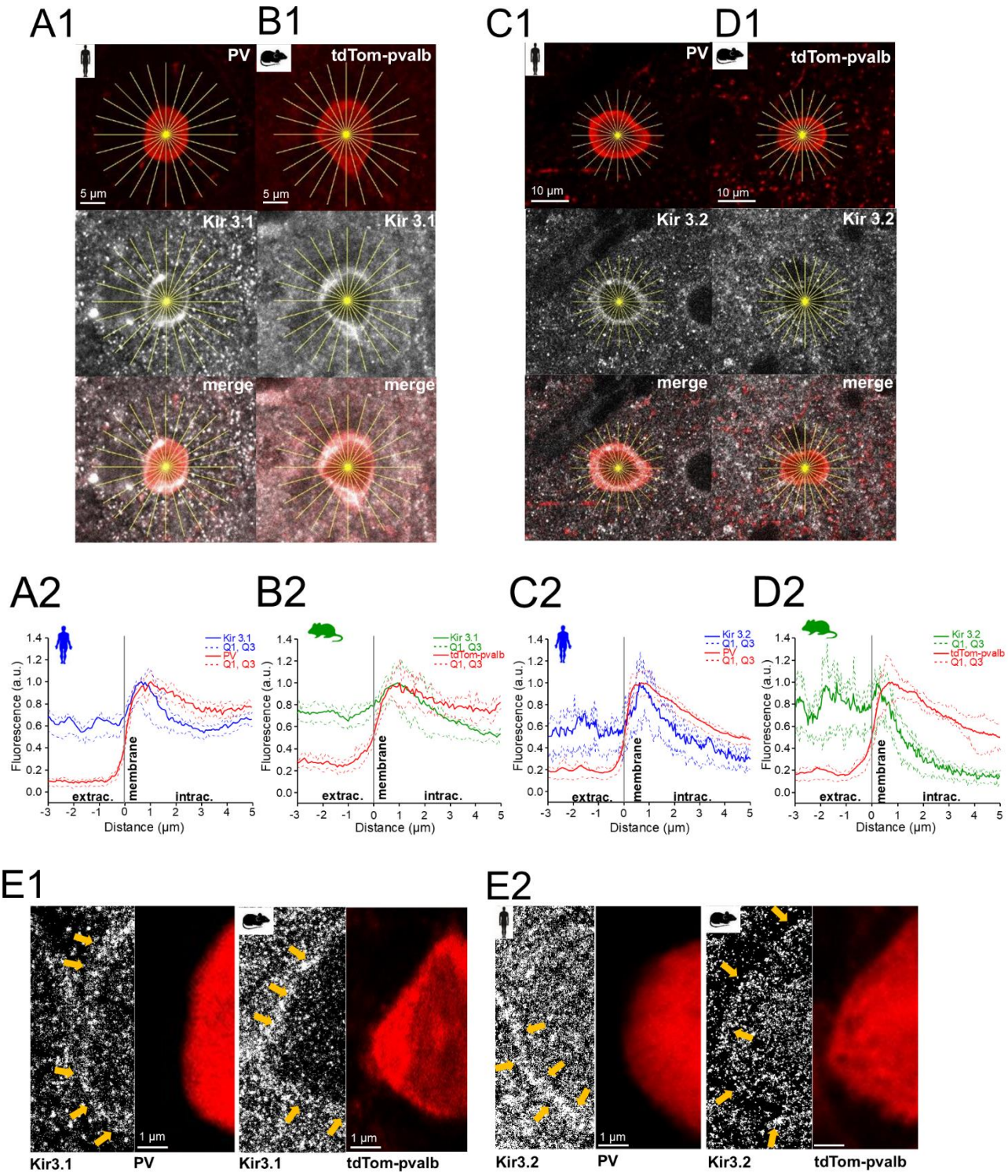

Figure 12. Kir3.1 and Kir3.2 channel proteins are present in the soma of human and mouse Pvalb neurons. (A1) Confocal microscope image of immunofluorescence reactions in Pvalb neuron (top) in human neocortex L2/3 for Kir3.1 (middle), and their merged images (bottom). Immunofluorescence intensity for Pvalb as well as Kir3.1 was

measured in a radial pattern of lines (shown in yellow in the images) that diverge from the center of the cell soma and project into the extracellular space. Immunofluorescence intensity was measured along 24 radial lines. (A2) Immunofluorescence intensity (ordinate, arbitrary units) for both Pvalb (red line) and Kir3.1 (blue line) measured along lines from extracellular space (negative values) to inside the cell soma (positive values) crossing the extracellular membrane (0-point). The extracellular membrane (0-point) in the lines is determined by the appearance of the Pvalb immunofluorescence signal. Solid lines show median and dashed lines show the quartiles (Q1 and Q3) of intensity values in 24 pooled lines. The blue line shows the peak intensity at the extracellular membrane region. (B1) Confocal fluorescence image of tdTomato (top) in Pvalb neuron in a mouse neocortex L2/3 with immunoreactivity for Kir3.1 (middle) and the merged image (bottom). (B2) Pooled data from 24 line analyses of tdTomato (red) and Kir3.1 fluorescence (green) in the mouse cell (median and interquartile range). The Kir3.1 intensity peak is located at the extracellular membrane. (C1) Pvalb and Kir3.2 immunoreaction line analysis in human neurons, and pooled data from 24-line analysis of the fluorescence intensity (C2). Human cell shows Kir3.2 immunofluorescence peak at extracellular membrane. (D1) TdTomato and Kir3.2 confocal images in mouse cells, and (D2) median and the quartiles of the 24-line analysis. Kir3.2 immunofluorescence is strongest at the extracellular membrane in the mouse Pvalb neuron. (E) Black and white micrographs show STORM super resolution images of the immunofluorescence reaction (at cy5) for Kir 3.1 (E1) and Ki3.2 (E2) with confocal microscope image of Pvalb (cy3, human) and TdTomato (mouse). Arrow lines in the Storm images indicate Kir3.1 or Kir3.2 antibody locations on the extracellular membrane (compare image for cytoplasmic parvalbumin immunofluorescence).

A computational single-cell model illustrates how somatic Kir conductance suppresses excitability

A computational single-cell model was employed to replicate the electrical features of Pvalb neurons observed in whole-cell recordings. For the purpose of the simulations, a neuron with intrinsic electrical properties that overlap recorded values in both human and mouse neurons was selected (neuron H4) when applying input currents in the soma. The model Pvalb neuron was characterised by a soma with passive leak membrane conductance, HCN-type current, Kv7- and Kv1-type potassium current in soma and dendrites, and Hodgkin-Huxley action potential current in axons (Szegedi et al., 2024). The input resistance and capacitance of the model cell were found to be analogous to those of the actual neuron, and the Vm changes produced by input currents in the model cell (from -300 pA to +200 pA square pulse in 250 ms steps) were found to be analogous to those of the real Pvalb neuron (Fig. 13A-C). In order to determine the actual Kir current conductance required for the Rin rectification ratio observed in whole-cell recordings from real neurons with a wide range of resting Rin, we simulated the model cell with varying 'resting' membrane ion permeability by varying the passive leak conductance in the soma between 1 nS and

11 nS. Furthermore, we simulated a cell with a variable Kir channel conductance (ranging from 0 nS to 20 nS maximal conductance, with approximately 10% and 90% active at -70 mV and -90 mV Vm values, respectively) localized in the membrane of the model cell's soma (Fig. 13D1-2). The range of resting Rin values in the simulation covered values measured in real human and mouse Pvalb neurons during whole-cell recordings. Furthermore, the Kir channel conductance range was adjusted so that Rin rectification ratios corresponded to those measured in real-life Pvalb neurons in human and mouse. The voltage dependence of the intrinsic excitability of the model Pvalb neuron under these conditions is shown in the heat map in Fig. 13D1, and the color coding indicates the Rin ratio rRin (Rin at -90 mV / Rin at -70 mV). The heatmap demonstrates that the rRin in neurons with reduced passive leak conductance requires less Kir channel conductance in the soma to generate the rRin, which is analogous to that observed in cells with elevated passive leak conductance. Fig. 13D2 demonstrates the dependence of Kir-current conductance on Vm in the simulations, alongside the passive ion leak conductance (Gleak) and Ih-current conductance (Szegedi et al., 2023).

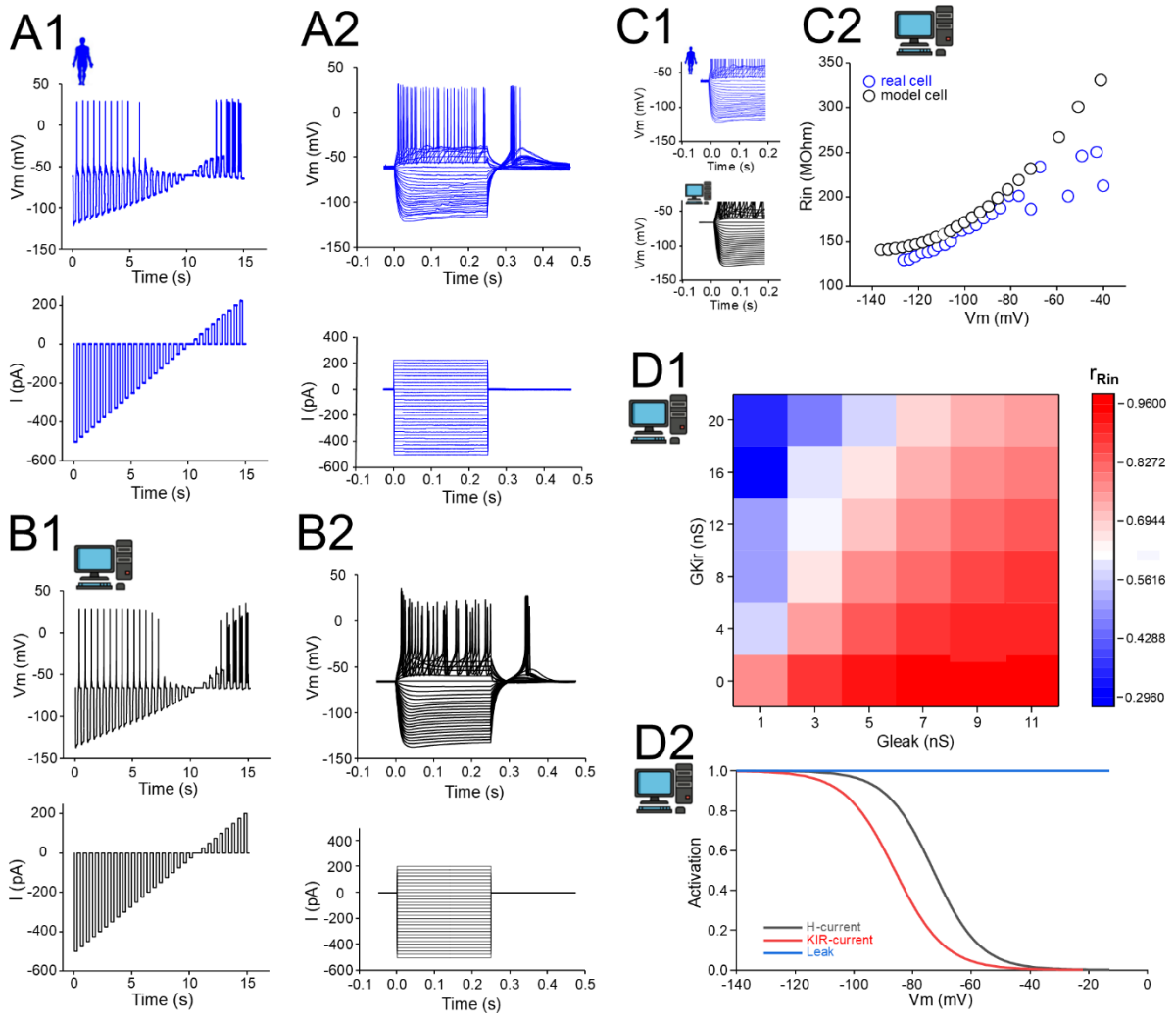

Figure 13. Computational model simulation modelling the regulation of input excitability by Kir channel activity in Pvalb neurons with different passive leak conductances. (A1) The I-V step protocol to study Rin at different Vm. (A2) Superimposed Vm-step traces (top) and the current steps (bottom). (B1) The I-V step protocol shows Rin at different Vm. (B2) Superimposed Vm-step traces (top) by current steps (bottom). (C1) Superimposed Vm traces in the real Pvalb neuron (blue) and the model cell (black). (C2) The plot shows the input resistance (Rin) at different membrane potentials (Vm) in the real cell (blue) and in the model (black). (D1) The heat map shows the rRin in the model cell in different configurations when the passive leak conductance (Gleak) in soma varies from 1 nS to 11 nS and the Kir conductance varies from 0 nS to 20 nS. (D2) Note that because GKir depends on Vm, the simulated cell has an active GKir (red line) of 5% of the abscissa GKir at -60 mV and 60% of the abscissa GKir at -90 mV. Gleak (blue line) is independent of Vm. The model cell has 1 nS (maximum) gHCN (black line) with the voltage dependence shown in plot.

AIS Geometry and Kv1 Channels Shape AP Threshold (Research study III)

In humans, Pvalb fast-spiking interneurons have a lower action potential (AP) threshold compared to mice. This adaptation compensates for the slower membrane time constant of human neurons, ensuring a fast input-output function. From an evolutionary perspective, the lowered AP threshold in human Pvalb interneurons is also likely linked to increased energy efficiency. Human neurons have a longer axon initial segment (AIS) and contain fewer inhibitory Kv1.1 and Kv1.2 potassium channels than mouse neurons. AIS length is a major factor in determining the AP threshold and contributes to interspecies differences. Immunofluorescence analysis showed that Kv1.1 potassium channels are absent in human Pvalb neurons but present in mice.

Human Pvalb interneurons have a lowered action potential (AP) firing threshold

The AP firing threshold was measured in 80 Pvalb-expressing fast-spiking interneurons (Hu et al., 2014) in human neocortical tissue resected during deep brain surgery from 62 patients. We used whole-cell clamp technique in layer 2/3 in acute brain slices extracted from the frontal (n = 36), the temporal lobe (n = 20), and the parietal or other neocortical regions (n = 24) in male (n = 29) and female patients (n = 33) aged between 11 and 85 years. To identify the lowest threshold that triggered APs, positive Vm steps (square-pulse current steps of incremental amplitude, 500 ms at 1 Hz) were applied in cells current-clamped at −70 mV (Fig. 14A–B) (Li et al., 2014; Povysheva et al., 2008; René Wilbers et al., 2023). The AP firing threshold in human Pvalb cells (median, −39.0 mV, IQR = −44.8 to −34.7; n = 80 cells) was lower than that in mouse Pvalb neurons. The median AP firing threshold in mouse Pvalb neurons was found to be −33.4 mV (IQR= −35.9 to −28.4; n = 80 cells; $p < 0.001$, Student's t-test; Fig. 14C1–2). In human neurons, the AP firing threshold was found to be similar in the frontal cortex (mean = −39.45 mV, IQR = −42.58 to −32.86 mV; n = 36 cells) and the temporal cortex (mean = − 8.65 mV, IQR = −47.48 to −35.50 mV; n = 20 cells; $p = 0.179$, Student's t-test; Fig. 14D1). Furthermore, we calculated the average AP firing threshold per human subject, confirming that it was independent of demographic characteristics. The Pvalb cell firing threshold was similar in male subjects (mean = −39.00 mV, IQR = −44.53 to −32.87 mV; n = 29) and female patients (mean = −39.30 mV, IQR = −45.33 to −36.30 mV; n = 33;

p = 0.682, Mann–152 Whitney U-test; Fig. 14D2), and no dependence on age was observed (r = −0.159; n = 58 patients; p = 0.233, Spearman's test; Fig. 14D3). The results demonstrated that human Pvalb neurons exhibited a reduced AP firing threshold potential in response to excitation in the soma when compared to mouse Pvalb neurons.

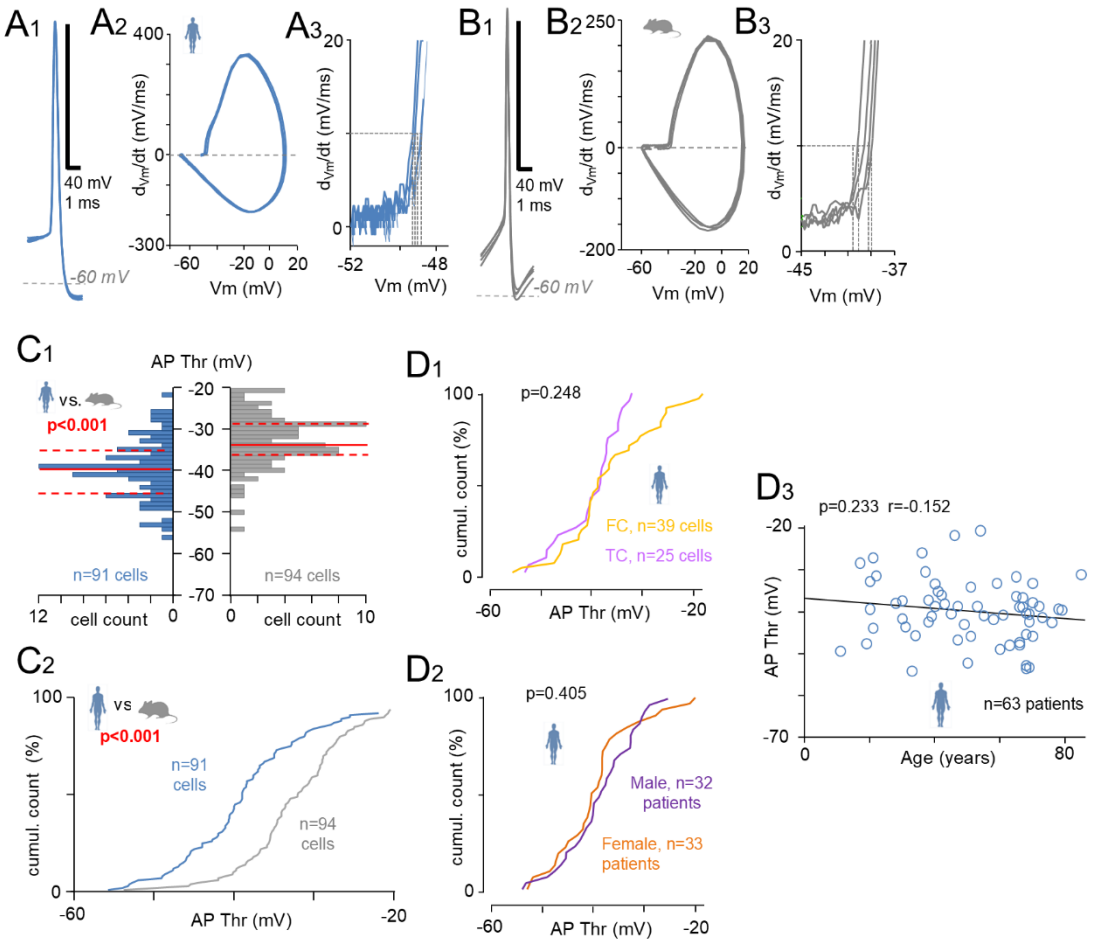

Figure 14. The firing threshold of APs in fast-spiking Pvalb interneurons differs between the human and the mouse. (A-B) The AP phase plot was used to define the firing threshold. (A1) Superimposition of APs (four) in human Pvalb cells. (A2) Phase plots of the APs exhibiting the first derivative (dV/dt) against Vm (four curves superimposed). (A3) Zoom-in to the AP phase plot curves presenting the initial rise speed of the AP. Dotted vertical lines denote the AP firing threshold, defined as the Vm at which the rise speed reaches 10 mV/ms (horizontal dotted line). (B1) Mouse Pvalb cell APs (four superimposed), their phase plots (B2), and the definition of the firing threshold (B3). (C) Pvalb neurons in humans exhibit a lower AP firing threshold than those in mice. (C1) Histograms of the AP firing threshold in humans (blue, 80 cells) and mice (gray, 80 cells), with 1 mV bin. The median and quartiles are indicated by solid and dotted red lines, respectively. (C2) The AP firing threshold in human (blue) and mouse (gray) Pvalb cells is presented with a cumulative histogram. (D) The AP firing threshold in human cells, presented as the average AP per

patient, is not dependent on (D1) the neocortical region (n = 36 patients studied for the frontal cortex [FC]; n = 20 patients for the temporal cortex [TC]). (D2) The AP threshold (average per patient) did not differ between the sexes (33 females, 29 males). (D3) The AP threshold (average per patient) is not associated with patient age (n = 58). The line denotes the regression.

Lowered AP threshold compensates for slower membrane tau

Human Pvalb neurons have higher electrical resistance (i.e. input resistance, Rin) in the soma compared to mouse cells. However, no significant between-species difference in Pvalb cell capacitance (Cm) was detected. The Rin and Cm of neurons were measured in subthreshold voltage steps ranging from +5 to +10 mV (evoked by square pulse current injections from -70 mV), (Fig. 15A1). The median Rin value recorded was 187.86 MΩ (interquartile range (IQR) = 125.62–298.88), which was observed in human Pvalb neurons (n = 50). This was higher than a median Rin value of 129.98 MΩ (IQR = 96.48–163.44) in mouse neurons (n = 40; p = 0.001, Mann–Whitney U-test; Fig. 15A2). On the other hand, the median Cm recorded in the soma was 32.82 pF (IQR = 23.72–63.30) in humans (n = 50), in comparison to 31.39 pF (IQR = 167 23.25–41.85) in mice (n = 40; p = 0.620, Mann–Whitney U-test). As a result, the time course of Vm changes (tau), measured systematically from the ascending phase in mV steps of +10 mV, was slower in human Pvalb neurons than in mouse Pvalb neurons (Fig. 15B1). The median electrical tau of the Vm step was 6.65 ms (IQR = 4.09–8.15) in humans (n = 50), versus 4.01 ms (IQR = 3.15–5.81) in mice (n = 40; p < 0.001, Mann–Whitney U-test; Fig. 15B2). In mouse Pvalb neurons, a strong positive correlation was observed between membrane tau and cell Rin (r = 0.625, p < 0.001; n = 40; Fig. 15C1), but no such correlation was detected in human Pvalb neurons (r = 0.114, p = 0.428; n = 50): tau levels were found to be comparable in human Pvalb neurons exhibiting high and low Rin levels (Fig. 15C2). However, in both species, a low AP firing threshold was associated with slow membrane tau (mice: r = −0.490, p = 0.001; n = 40; Fig. 15D1; humans: r = −0.331, p = 0.024; n = 50; Fig. 15D2). The data from both species were pooled (Fig. 15D3) and a strong association between a low AP threshold and slow tau was detected (r = −0.575, p < 0.001, Spearman's correlation test; n = 90). These results show that Pvalb neurons with a slower tau have a lower AP firing threshold. This association was found to be particularly strong when the human and mouse data were pooled together.

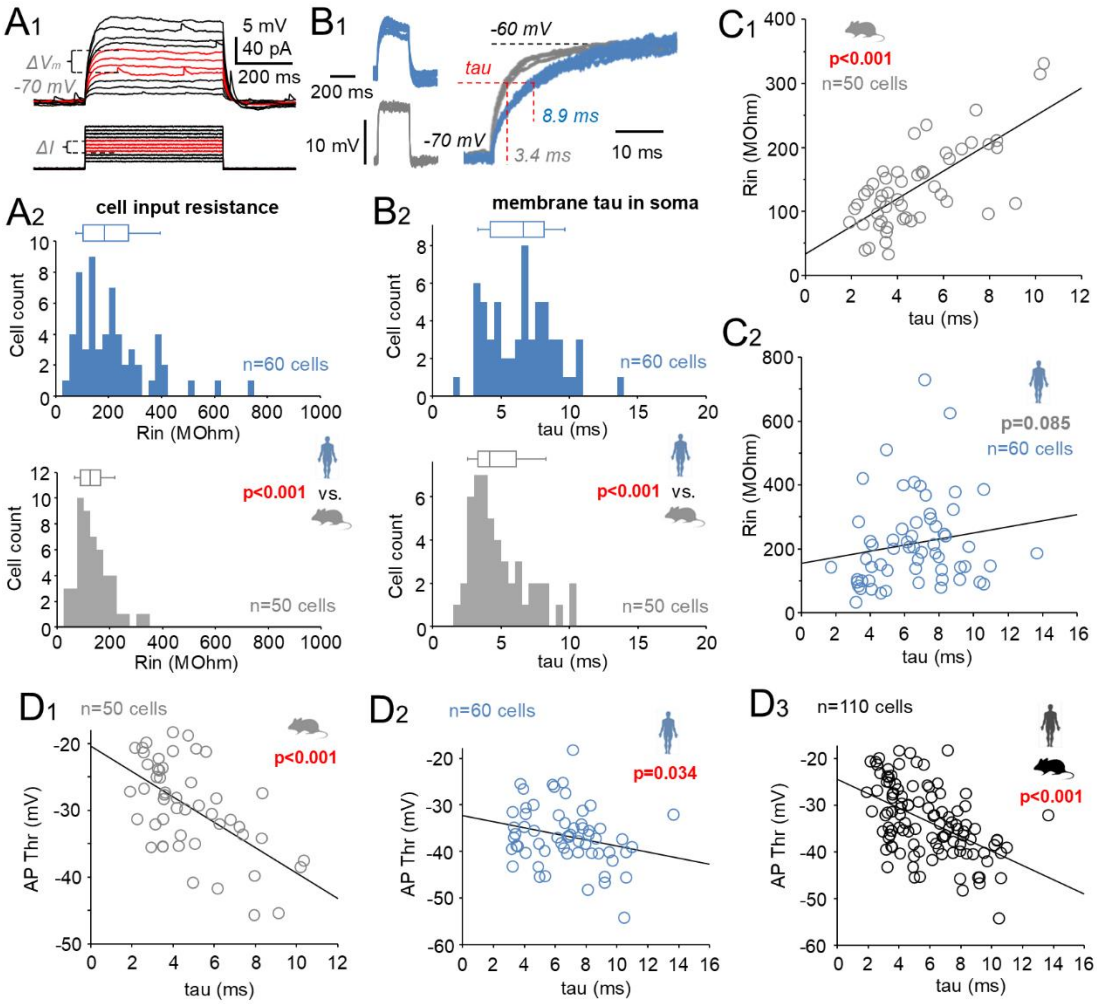

Figure 15. A low AP firing threshold in Pvalb interneurons is associated with an electrically slow soma. (A1) Cell Rin was systematically measured using positive current steps generating 5–10-mV subthreshold depolarizations. The voltage shifts (ΔVm) and current steps (ΔI) to define the average Rin in the cell are illustrated in red. (A2) Histograms and box plots present Rin in Pvalb neurons in humans (blue) and mice (gray). The bin is 25 MΩ, and box plots present the median, quartiles, and 5th and 95th percentiles. (B1) Tau was measured from the ascending phase in +10-mV steps delivered at −70 mV (human, blue; mouse, gray). Left: superimposed (four) +10-mV steps in human and mouse Pvalb cells. Right: Ascending phase of the voltage steps displays differences in tau (average: 8.9 ms in humans and 3.4 ms in mice). (B2) Histograms and box plots illustrate the difference in tau between human (blue) and mouse (gray) Pvalb neurons. Histogram bin, 0.5 ms. Membrane tau and Rin in the soma are tightly associated in mouse Pvalb neurons (C1) but not in human Pvalb neurons (C2). (D) A low AP firing threshold is associated with slow membrane tau in mouse (D1) and human Pvalb neurons (D2). (D3) Values from both species pooled together reveal a strong association between slow tau and a low AP firing threshold.

The AIS length and location affect the AP threshold in Pvalb neurons

This study aimed to visualise the AIS (AP initiation site) of Pvalb cells in the human and mouse neocortex. We focused on the association of the AIS length and position along the axon and the AP threshold (Yamada & Kuba, 2016). Immunohistochemistry was performed for beta-IV-spectrin, a cytoskeletal protein enriched in the AIS (Jones & Svitkina, 2016; Leterrier, 2018; Yang et al., 2007), and its immunofluorescence was analysed in three-dimensional confocal microscopic image stacks. The length of the AIS and its distance to the cell soma were digitally measured using a specially written script. All cells were analysed in layer 2/3 neocortical neurons, and their immunopositivity for Pvalb was confirmed (Fig. 16A1). It was observed that both human and mouse Pvalb neurons exhibited cell-to-cell variation in the AIS length and its positioning along the axon (Fig. 16A2). The median distance from the AIS initiation site to the soma did not differ between human and mouse neurons (4.12 μm, IQR = 2.95–5.28; n = 100 cells in 17 patients versus 3.77 μm, IQR = 2.69–4.68; n = 78 cells in 15 mice; $p = 0.265$). Nevertheless, the median AIS length was found to be more pronounced in human cells (16.68 μm, IQR = 14.08–19.78) in comparison to mouse cells (13.99 μm, IQR = 11.15–16.55; $p < 0.001$). Therefore, the AIS termination site was more distant from the soma in humans (21.01 μm, IQR = 17.60–24.66; 100 cells from 17 samples) than in mice (17.47 μm, IQR = 14.41–20.66 μm; 78 cells from 15 mice; $p < 0.001$, Mann–Whitney U-test; Fig. 16A2–3).

In the subsequent study, we tested the hypothesis as to whether these AIS properties could provide a rational explanation for the AP threshold difference observed between the two species. Electrophysiologically investigated and biocytin-filled neurons were visualised with streptavidin–fluorophore and confirmed to be immunopositive for Pvalb. The AIS was then visualised based on its positivity for beta-IV-spectrin, and the AIS length and its distance from the soma along the axon were measured. The values were then compared against the AP firing threshold. From a total of 28 human and 22 mouse cells that were recorded in the whole-cell clamp, the intact soma and full-length AIS were successfully recovered (as demonstrated by beta-IV-spectrin immunofluorescence) in 13 human and 14 mouse neurons. Particular attention was paid to only include neurons that showed a biocytin-filled axon continuing beyond the distal end of the beta-IV-spectrin–visualized AIS to ensure that the AIS was entirely captured for measurement (Fig. 16B1). The distance from the initial part of the AIS to the soma in human Pvalb neurons was 6.10

μm (IQR = 2.55–8.50; n = 13), versus 4.85 μm (IQR = 217 3.80–6.03; n = 14) in mouse neurons (p = 0.437; Fig. 16B2). The AIS was found to be significantly longer in human cells (17.60 μm, IQR = 14.65–20.20 μm) compared to mouse cells (14.0 μm, IQR = 12.10–15.33; p = 0.004). The distance from the AIS terminal site to the soma was found to be longer in human neurons (23.60 μm, IQR = 20.85–25.75 than in mouse neurons (18.55 μm, IQR = 17.68–20.38; p < 0.001; Mann–Whitney U-test). The AIS properties are shown in Fig. 16B2. Neither of the AIS parameters was correlated with the AP firing threshold in human or mouse Pvalb neurons. The correlation between the AIS proximal site distance and the AP firing threshold was 0.536 (p = 0.054) in human cells (n = 13) and −0.297 (p = 0.93) in mouse cells (n = 14). The AIS length and AP threshold demonstrated no significant correlation in human cells (r = 0.203, p = 0.493) or mouse cells (r = 0.079, p = 0.773). The distance from the AIS termination site to the soma was also not correlated with the AP threshold in human (r = −0.239, p = 0.414) or mouse cells (r = 0.024, p = 0.988, Spearman's correlation test). Conversely, when AIS data from Pvalb cells from both species were aggregated and evaluated, a correlation was observed between the AP threshold and the distance from the AIS initiation site to the soma (r = −0.478, p = 0.012; Fig. 16C1) and the distance from the termination site to the soma (r = −0.383, p = 0.0485). However, no correlation was observed between AIS length and AP threshold (r = −0.1340, p = 0.516; Spearman's correlation test; Fig. 16C2–3). The results demonstrated that the AIS length and its location along the axon vary between humans and mice, and that distal positioning of the AIS from soma is associated with lowered AP threshold.

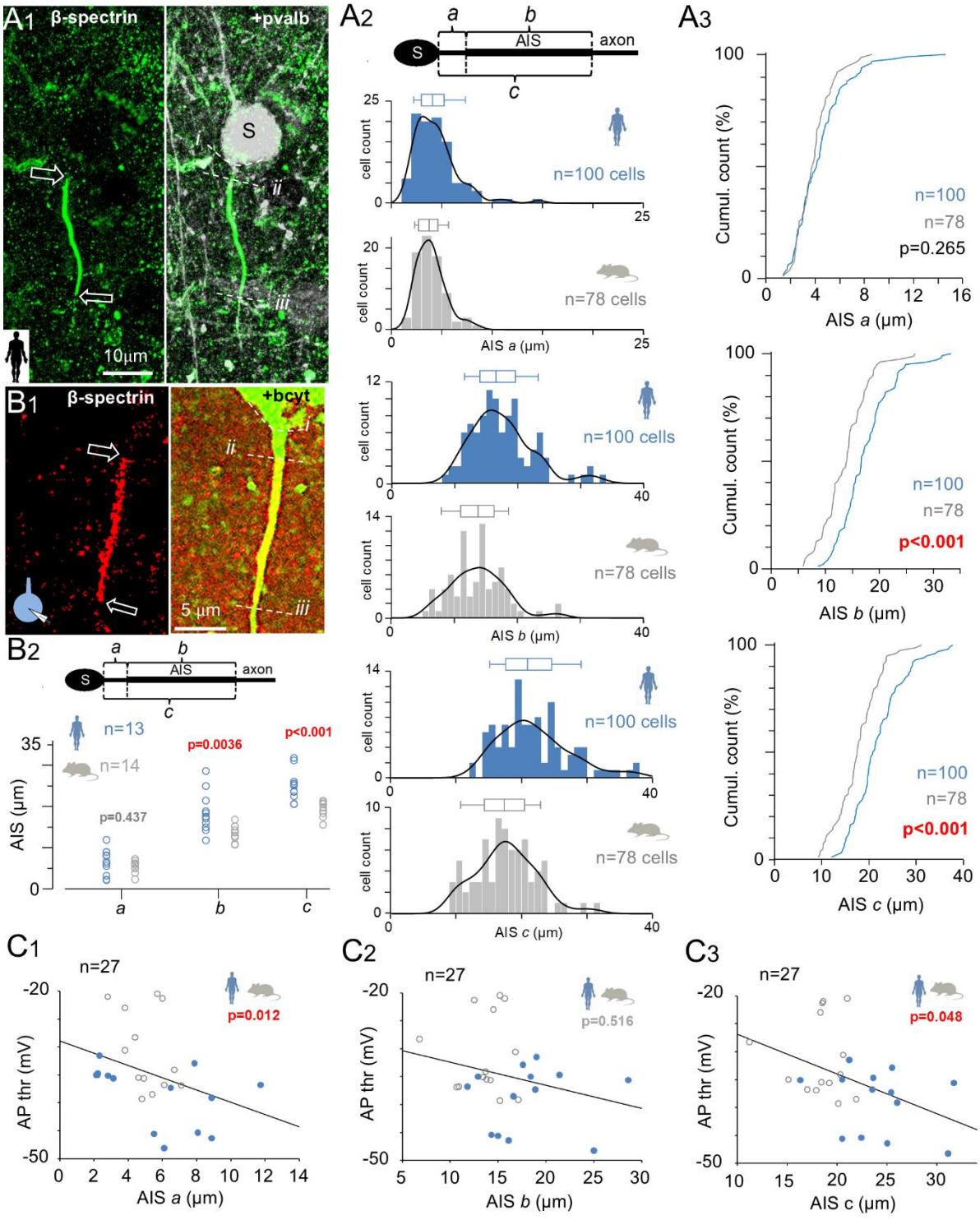

Figure 16. The AIS is found to be elongated in human Pvalb neurons in comparison to its location in mouse neurons. The location of the AIS along the axon was associated with the AP threshold. (A1) The AIS was measured in three-dimensional fluorescence confocal microscopic images of human and mouse Pvalb immunopositive neurons in layer 2/3. Left: The AIS was visualized via immunofluorescence for beta-IV-spectrin. Arrows indicate the initiation and

termination sites of the AIS (Alexa 488) in a collapsed z-stack image of a human Pvalb neuron. The merged image of beta-IV-spectrin and Pvalb (Cy5) immunoreactions is shown on the right. Horizontal dotted curves represent the axon from the soma (s) and the proximal (ii) and (iii) distal ends of the AIS. (A2) Histograms and box plots summarize three AIS parameters as outlined in the upper schematic: a = distance from the soma to the AIS initiation site, b = AIS length, and c = distance from the soma to the AIS termination site. The upper image demonstrates that the distance from the soma to the AIS initiation site is comparable across species. The middle image indicates that the AIS is more pronounced in human neurons compared to mouse neurons. The AIS termination site is more distant in human neurons than in mouse neurons. The histogram bin is 1 μm with kernel density. Box plots present the median, quartiles, and 5th and 95th percentiles. (A3) The AIS data in cumulative histograms show p-values. (B1) Illustrates the AIS visualised via immunopositivity for beta-IV-spectrin (Cy3) in human and mouse Pvalb cells recorded in whole-cell configuration and filled with biocytin (bcyt), as well as visualised with streptavidin–Alexa 488. (B2) Electrophysiologically studied Pvalb neurons display with three measured parameters (a,b,c). The combined AP threshold data from human (blue symbols) and mouse (grey) Pvalb neurons reveal an association with the AIS initiation site distance (C1), no association with AIS length (C2), and an association with (C3) the distance from the AIS termination site to the soma.

Axon diameter does not explain AP firing threshold difference between species

The axon caliber can regulate axon excitability (Goethals & Brette, 2020), thus we measured the axon diameter in biocytin-filled Pvalb interneurons to study whether it is correlated with the AP firing threshold. Diameter measurement was conducted utilising high-magnification fluorescence confocal microscopic images of biocytin-filled, visualised neurons at five locations along the axon, including two measurement points before the AIS (pre-AIS) and three sites within the AIS, as illustrated in Fig. 17A1–3. The values thus represent the average per cell for the pre-AIS segment of the axon and the part of the axon within the AIS. No statistically significant difference in axon diameter was detected between human (n = 12) and mouse (n = 14) Pvalb neurons in either the pre-AIS (1.07 μm IQR = 0.82–1.19 vs. 0.88 μm IQR = 0.71–1.14 ; p = 0.939) or AIS (0.83 μm IQR = 0.70–0.96 vs. 0.69 μm IQR = 0.64– 0.74; p = 0.260; one-way ANOVA on ranks; Fig. 17B). Furthermore, the axon diameter in the pre-AIS and AIS was not correlated with the AP threshold in human (pre-AIS: r = 0.245, p = 0.429; AIS: r = 0.392, p = 0. 197; n = 12) or mouse neurons (pre-AIS: r = 0.091, p = 0.766; AIS: r = 0.056, p = 0.852; n = 12). When considering all cells from both species, no association was identified between axon width and AP threshold in either the pre-AIS (r = 0.137, p = 0.518; Fig. 17C1) or AIS (r = −0.036, p = 0.866; Spearman's correlation test; Fig. 17C2). These results indicate that axon diameter is unlikely to account for interspecies differences in AP threshold in Pvalb neurons.

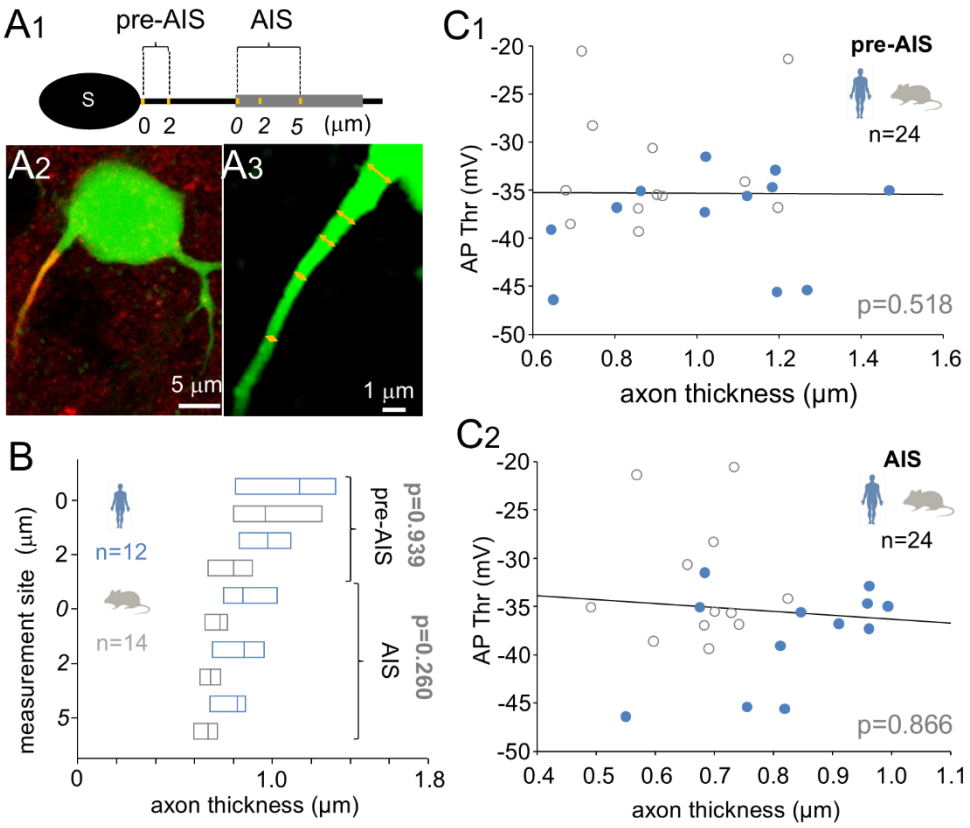

Figure 17. The axon diameter fails to account for interspecies differences in the AP firing threshold in Pvalb interneurons. The schematic presentation (A1) illustrates the axon maximum width at five distinct locations along the axon. (A2) Fluorescence confocal microscopic image (collapsed from the z-stack) presenting biocytin-filled Pvalb neurons (Alexa 488) in humans with the AIS visualized by immunoreaction for beta-IV-spectrin (Cy3). (A3) A magnified image of the axon with five measurement sites. (B) The thickness of the axon did not vary between human (blue) and mouse (grey) Pvalb neurons. Horizontal bars denote the median and quartiles. (C) The axon diameter was not associated with the AP firing threshold in Pvalb neurons in the pre-AIS area (C1) or AIS (C2).

Nav1.6 channel distribution is uniform within the AIS of Pvalb neurons

The immunoreactivity of the low-voltage-gated sodium channel Nav1.6 in the AIS of Pvalb neurons was the next subject of our study (Fig. 18), since the density and spatial distribution of Nav1.6 channels in the AIS can regulate the threshold of AP generation (Kole & Stuart, 2012; Kuba & Ohmori, 2009). Nav1.6 channels have been shown to concentrate at the distal end of the AIS, reducing the AP firing threshold (Goethals & Brette, 2020; Kole & Stuart, 2012; Lorincz & Nusser, 2008; O'Brien & Meisler, 2013), or to be evenly distributed along the AIS. We studied the intensity

of Nav1.6 immunofluorescence in confocal microscopic three-dimensional image stacks along the axon (Fig. 18B1-2) in layer 2/3 of the human and mouse neocortex (Fig. 18A1-2) to investigate whether the distribution of Nav1.6 channels differed between species. We measured the immunofluorescence intensity for Nav1.6, Pvalb and beta-IV-spectrin in the same cells along the axon (annotating the axon in 3D stack of images) from the soma to beyond the AIS termination site (Fig. 18C1-2). The Nav1.6 immunofluorescence was similar in humans and mice, with weak F-Fex.c in the axon pre-AIS (human: 6.55, IQR = 4.03–20.69, n = 21; mouse: 6.25, IQR = -0.87–16.24, n = 26; p = 1.00) and in the post-AIS (human: 0.95, IQR = -3.41–7.56, n = 21; mouse: 4.59, IQR = -2.49–13.13, n = 26; p = 1.00). The Nav1.6 intensity was robust in the AIS and did not differ between humans (73.18, IQR = 49.32–94.05) and mice (48.40, IQR = 28.84–67.81) (p = 0.063) (Fig. 18C1-2 for details; PERMANOVA and Mann–Whitney U-test with Bonferroni Correction for pairwise comparisons). Additionally, the Nav1.6 immunofluorescence was uniformly distributed along the AIS in both species, showing no difference in immunoreaction intensity between the first and second halves (human: p = 0.182; mouse: p = 0.833; Mann–Whitney U test) (Fig. 18C1-2).

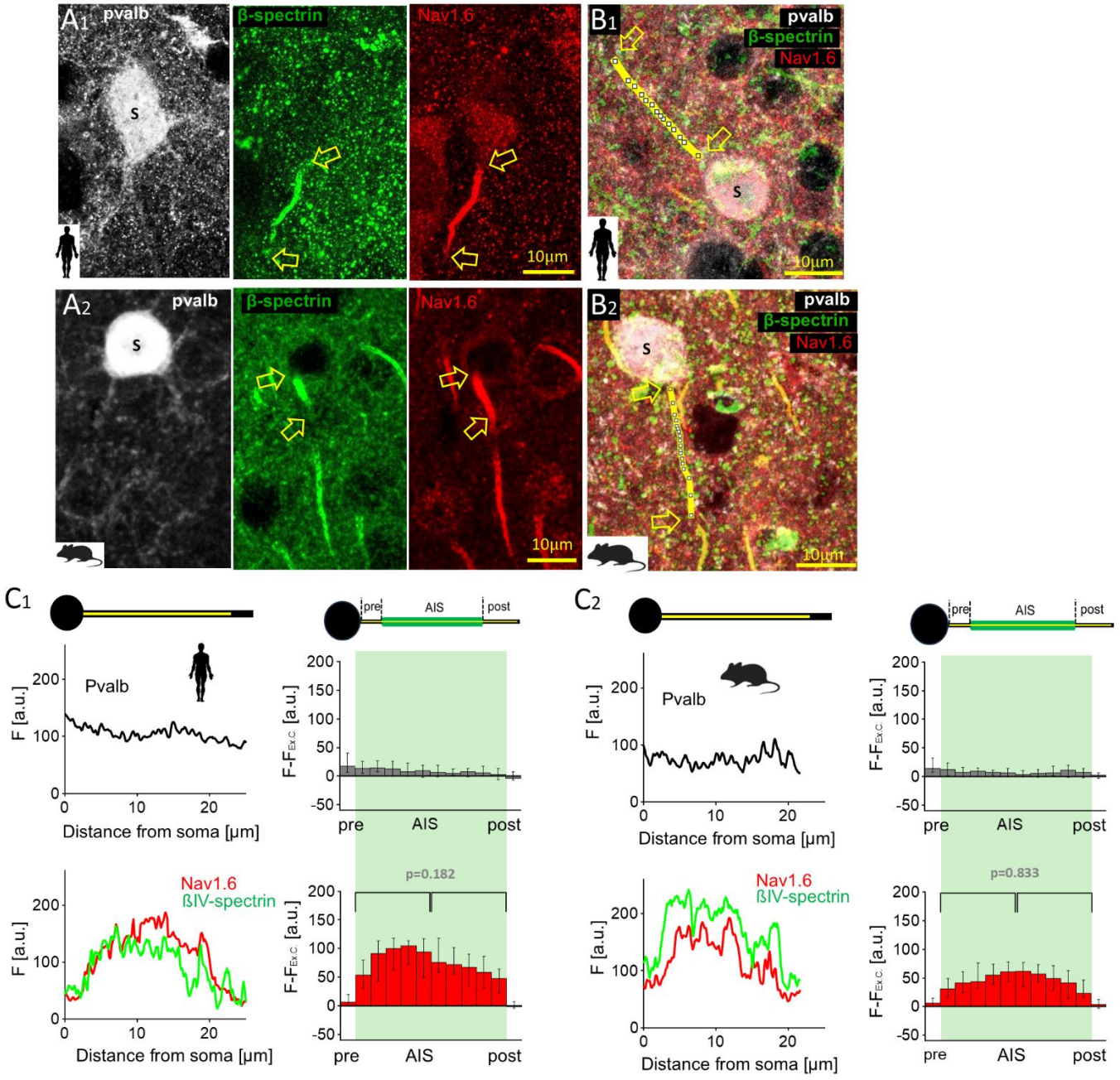

Figure 18. The AIS shows strong and uniform Nav1.6 sodium channel expression in both human and mouse Pvalb neurons. (A) Triple immunofluorescence labeling for Pvalb (Cy5), βIV-spectrin (Alexa 488), and Nav1.6 (Cy3) in human (A1) and mouse (A2) neocortex. Collapsed z-stack confocal images show AIS initiation and termination (arrows) and the Pvalb⁺ soma (s). (B) Axonal fluorescence intensity measurements along a line from the soma (s) through the AIS and into the distal axon, obtained from three-dimensional confocal image stacks in human (B1) and mouse (B2) neurons. The measurement path follows the βIV-spectrin-labeled AIS. (C) Line analyses of fluorescence intensity for Pvalb (black), βIV-spectrin (green), and Nav1.6 (red). (C1) Left: Intensity profile from a single human neuron (arbitrary units); 0 marks axon origin from the soma. The upper schematic illustrates the measurement line.

Right: Median (bars) and quartiles (whiskers) of referenced fluorescence (F–Fex.) for human cells. The AIS, defined by βIV-spectrin labeling, was divided into 10 bins (green shading) for quantitative analysis. (C2) Equivalent data for a mouse neuron (left) and summary of pooled measurements (right).

In addition, we studied the intensity of Nav1.6 immunofluorescence in confocal microscopic images of the soma (Fig. 19A1-2). In individual cells in human (n = 21 cells; Fig. 19B1) and mouse (n = 26 cells; Fig. 19B2) tissues, 24 radially placed lines were positioned to extend from the inside of the soma to the extracellular space in order to measure the immunofluorescence intensity of Nav1.6 (Cy3) and Pvalb (Cy5). As Pvalb is an intracellular marker, the onset of Pvalb immunofluorescence in the measurement lines was used to define the extracellular membrane site (Fig. 19B1–2). Corrected Nav1.6 immunofluorescence (F–Fex.c.; the average fluorescence intensity of the extracellular site subtracted from the a.u. values of the radial and axon line pixels) did not differ between species in the soma membrane (human: 7.06, IQR = 4.72–15.12, n = 21; mouse: 8.52, IQR = 3.30–12.50, n = 26; p = 1.00) or in the cytoplasm (human: 23.66, IQR = 16.37–31.64, n = 21; mouse: 12.39, IQR = 5.88–20.25, n = 26; p = 0.067). Figure 19C shows the Nav1.6 immunofluorescence F–Fex.c values for human, and Figure 19D shows the values for mouse. There is no difference between species (Fig. 19E).

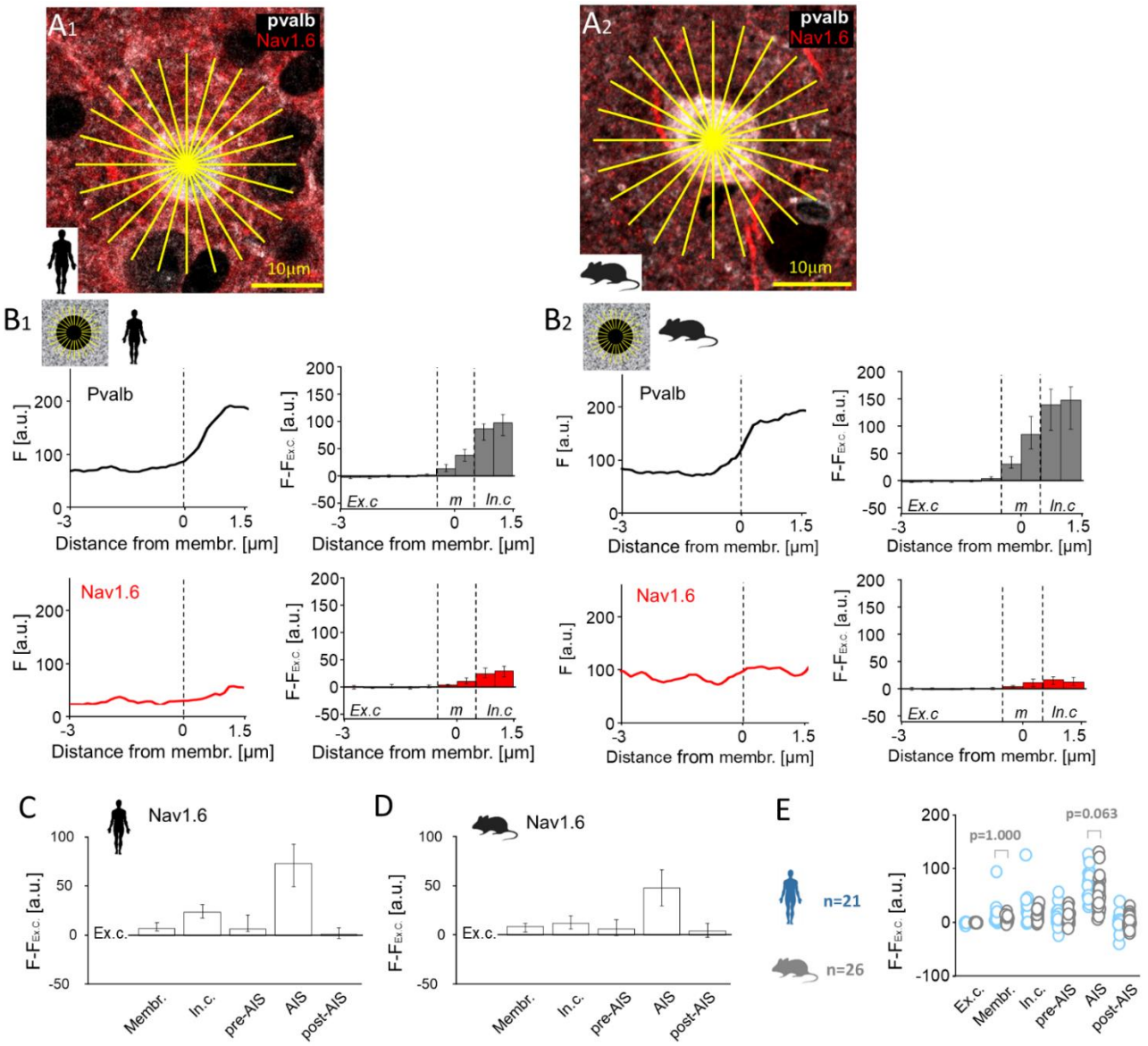

Figure 19. The Nav1.6 sodium channel expression is uniform in both human and mouse Pvalb neurons. (A) Nav1.6 immunofluorescence in relation to Pvalb labeling in the soma of human (A1) and mouse (A2) neurons. Fluorescence intensity was quantified using a 24-line radial sampling pattern (yellow lines). (B) Intensity profiles (in arbitrary units) for Pvalb (black) and Nav1.6 (red) measured along radial lines from the extracellular space (negative values) to the soma (positive values). The extracellular membrane region was defined as ±0.5 µm from the Pvalb signal onset (abscissa 0). (B1) Left: Mean fluorescence intensity (F, a.u.) from 24 pooled lines in a single human cell spanning −3 µm to +1.5 µm relative to the 0-point. Right: Median (bars) and quartiles (whiskers) of normalized fluorescence (F–Fex.c) for human cells. (B2) Equivalent measurements for mouse neurons (left) with group median and quartiles (right). Summary of normalized fluorescence intensity (F–Fex.c) across five cellular domains in human (C) and mouse (D) Pvalb neurons, showing strong Nav1.6 immunoreactivity in the AIS. (E) Comparison of F–Fex.c values between human (blue) and mouse (gray) neurons across cellular domains.

Human PVALB cells exhibit low expression of Kv1.1 and Kv1.2 in the AIS

The immunofluorescence of Kv1.1 and Kv1.2 potassium channels was studied, which are key inhibitory potassium channels controlling the AP threshold in the AIS in many neurons (Goldberg et al., 2008; Kole et al., 2007). Kv1.1 channels were found to be clustered in the AIS of rodent Pvalb neurons (Gu & Barry, 2011), where as low-threshold inhibitory channels, they elevate the AP firing threshold (D'Adamo et al., 2020; Goldberg et al., 2008). First, we compared the immunofluorescence signal for Kv1.1 channels in the AIS of human (Fig. 20A1) and mouse (Fig. 20A2) Pvalb neurons in triple immunoreaction studies. Figure 20B shows sample Pvalb neurons in humans and mice with Kv1.1 immunofluorescence analysis along the axon (Fig. 20B1-2). Analysis of mouse cell axons revealed a robust Kv1.1 signal (47.56, IQR = 13.98–74.95; n = 31) in the AIS, as previously reported (Goldberg et al., 2008). However, in human Pvalb cells, the Kv1.1 immunoreaction was weak or absent in the AIS, despite strong immunoreaction in Pvalb-immunonegative neurons within the same immunostained sections (Fig. 20A1). The F-Fex.c. for Kv1.1 in the AIS differed between species ($p = 0.001$) (Fig. 20C1-2). However, the F–Fex.c. for Kv1.1 in the pre-AIS (human: -1.06, IQR = -6.71–8.77; mouse: 9.56, IQR = -5.49–20.32; $p = 0.287$) and post-AIS (human: 2.55, IQR = -3.26–10.88; mouse: 4.58, IQR = -17.97–29.20; $p = 1.00$) did not differ between species (PERMANOVA and Mann–Whitney U-test with Bonferroni Correction). Kv1.1 immunofluorescence showed no difference between the first and second half of the AIS (human: $p = 0.318$; mouse: $p = 0.195$; Mann–Whitney U test) (Fig. 20C1–2).

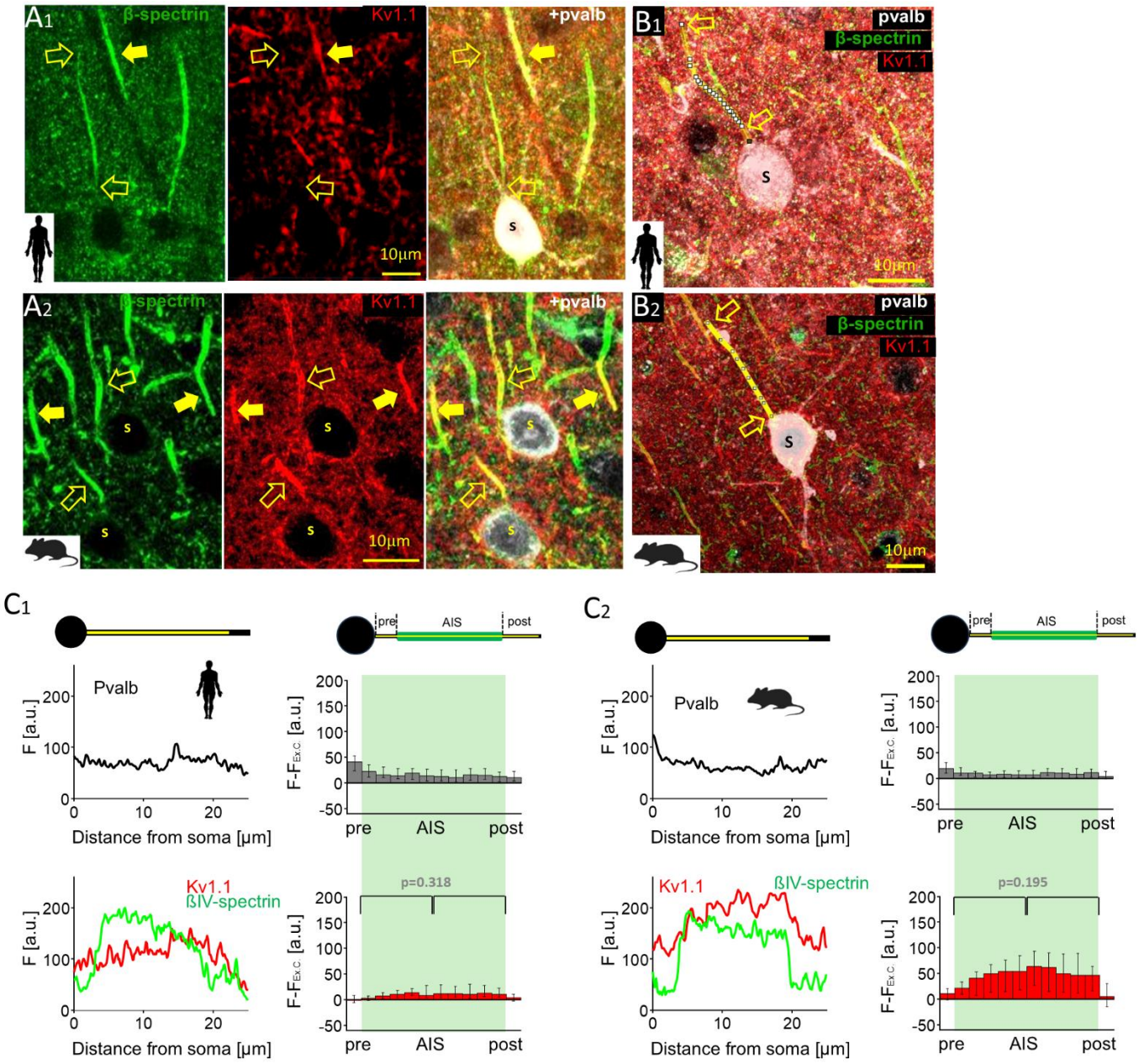

Figure 20. Kv1.1 potassium channels are largely absent from the axon initial segment (AIS) of human Pvalb neurons compared with mice. (A1) Triple immunofluorescence staining for βIV-spectrin (Alexa 488), Kv1.1 (Cy3), and parvalbumin (Cy5) in the human neocortex. Open arrows indicate AISs of Pvalb⁺ neurons identified by βIV-spectrin labeling, while the solid arrow marks the AIS of a Pvalb⁻ neuron (s = soma of a Pvalb⁺ cell). (A2) Equivalent triple staining in the mouse neocortex. Open and solid arrows mark the AISs of Pvalb⁺ and Pvalb⁻ neurons, respectively. (B) Immunofluorescence profiles along the axon (s = soma) in confocal z-stack projections from human (B1) and mouse (B2) neurons. Measurement paths are shown relative to the βIV-spectrin signal. (C) Line intensity profiles for Pvalb (black), βIV-spectrin (green), and Kv1.1 (red) along the axon. (C1) Left: Fluorescence profiles from one human neuron, with the 0-point marking axon origin. Right: Median (bars) and quartiles (whiskers) of normalized fluorescence (F–

Fex.) in human cells. AIS length (green shading) was divided into 10 bins for group analysis. (C2) Equivalent analysis for a mouse Pvalb neuron (left) with pooled data shown as median and quartiles (right).

Then, we compared the immunofluorescence signal for Kv1.1 channels in the soma of human (Fig. 21A1) and mouse (Fig. 21A2) Pvalb neurons in double immunoreaction studies. The F–Fex.c. immunoreaction showed an absence of Kv1.1 at the soma membrane in humans (-1.23, IQR = -4.77–5.25; n = 31), and a presence in mice (5.42, IQR = 0.62–10.58; n = 31) (p = 0.041). Kv1.1 immunofluorescence was lowest in the intracellular cytoplasmic site in both species, with no difference between species (p = 0.817) (Fig. 21B1-2). Figure 21C–D summarises the F-Fex.c. intensity values for Kv1.1 in the cellular domains of human and mouse Pvalb neurons, and Figure 21E compares these values between species.

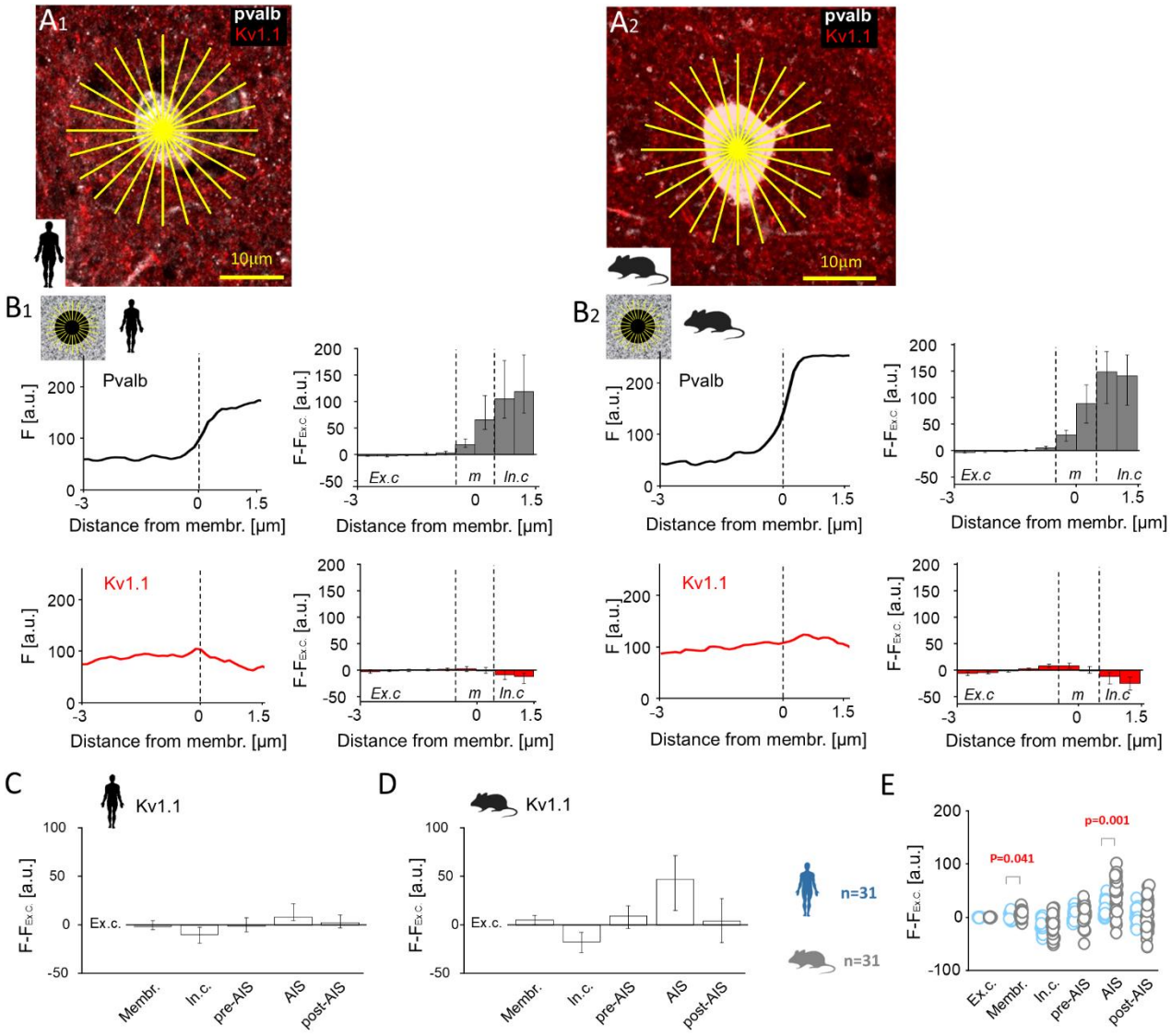

Figure 21. Kv1.1 potassium channels are largely absent in the human Pvalb neurons, but present in mice. (A) Kv1.1 and Pvalb immunofluorescence in human (A1) and mouse (A2) cells, showing intensity measurements obtained with a 24-line radial sampling pattern (yellow lines). (B) Radial intensity profiles for Pvalb (top, black) and Kv1.1 (bottom, red) across the soma membrane. The vertical dotted line (0-point) marks the onset of Pvalb signal. (B1) Left: Mean fluorescence intensity (F, a.u.) from 24 pooled radial lines in a single human cell, spanning −3 µm to +1.5 µm from the 0-point. Right: Median (bars) and quartiles (whiskers) of Pvalb (gray) and Kv1.1 (red) normalized fluorescence (F–Fex.c) in human cells. (B2) Corresponding analysis in a mouse cell (left) and summary of median and quartiles across mouse cells (right). (C) Summary of Kv1.1 fluorescence intensity (F–Fex.c) across cellular compartments in human and mouse Pvalb neurons. (D) Comparison of normalized Kv1.1 fluorescence (F–Fex.c) across neuronal domains in human (blue) and mouse (gray) cells. (E) Comparison of F–Fex.c values between human (blue) and mouse (gray) neurons across cellular domains.

We similarly studied the immunofluorescence of Kv1.2 potassium channels (Fig. 21A1-2) and in the AIS (Fig. 21B1-2) between human and mouse Pvalb neurons (Ogawa et al., 2008). There was no difference in F–Fex.c. between human (2.95, IQR = -3.23 to 9.05, n = 60) and mouse (17.04, IQR = -5.30 to 31.76, n = 30) AIS mouse cells ($p = 0.272$) (Fig. 21C1-2), pre-AIS cells ($p = 0.478$) or post-AIS cells ($p = 0.187$) (PERMANOVA and Mann–Whitney U-test with Bonferroni Correction). Kv1.2 immunofluorescence intensity did not differ between the first and second halves of the AIS (human: $p = 0.397$; mouse: $p = 0.984$; Mann–Whitney U-test) (Fig. 21C1–2).

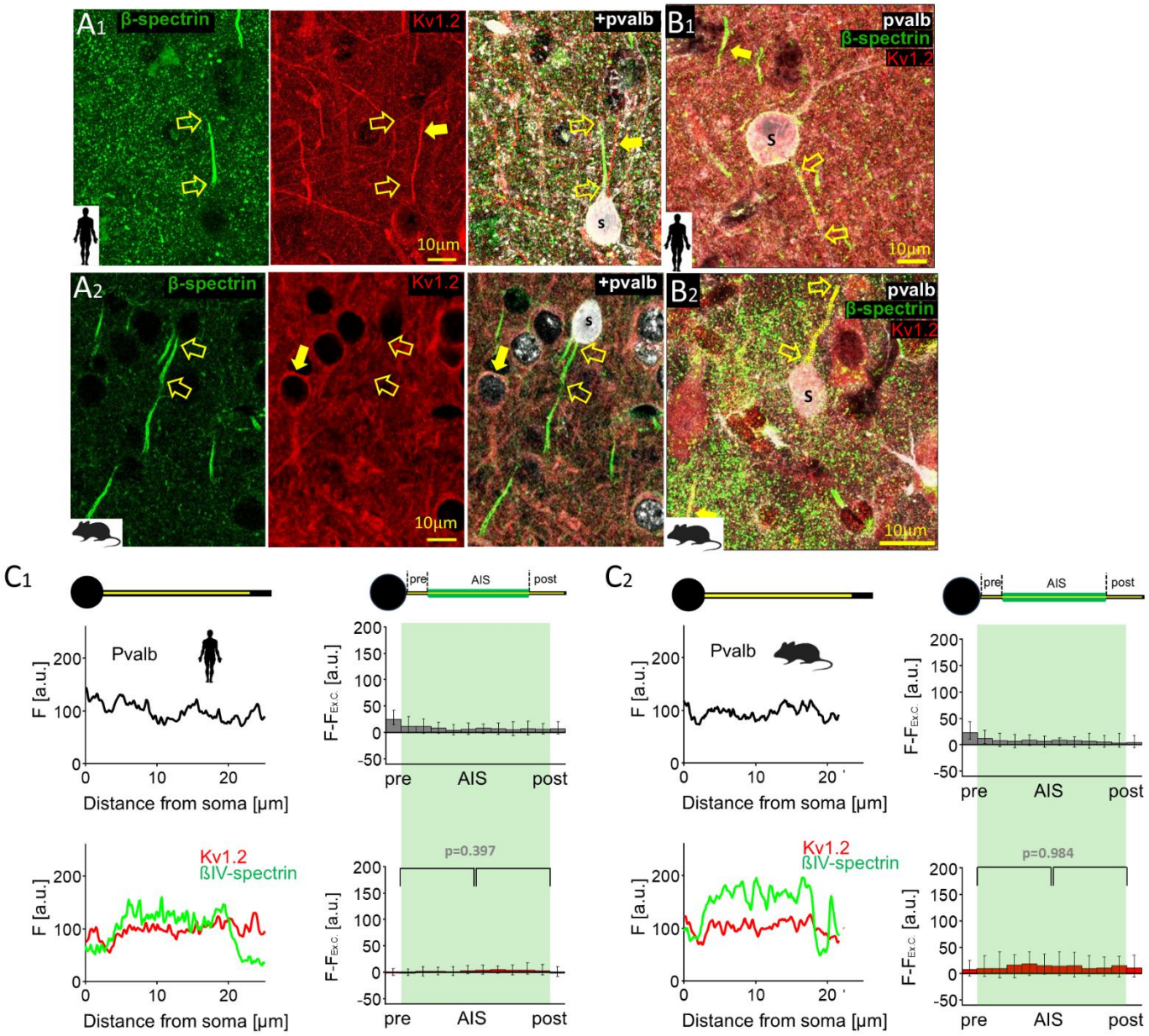

Figure 22. The AIS is similarly low in Kv1.2 potassium channels in humans and mice. (A) Immunofluorescence staining for Kv1.2 was equally weak in the AIS in human and mouse Pvalb neurons. Triple immunofluorescence reaction for beta-IV-spectrin (Alexa 488), Kv1.2 (Cy3), and Pvalb (Cy5) in human (A1) and in mouse (A2). Open arrows denote AISs visualized using beta-IV-spectrin in a Pvalb+ neuron with undetectable Kv1.2. Solid arrow points to a Kv1.2 immunopositive dendrite and soma membrane of another neuron (s = the Pvalb+ cell soma). (B) The immunofluorescence intensity measurement in the axon (s = soma) in human (B1) and in mouse (B2) (collapsed z-stack images). The measurement line is illustrated in the axon. (C) Line analysis along axons (Pvalb, black; beta-IV-spectrin, green; Kv1.2 red). (C1) Left: the line intensity values in one human cell (illustrated in schematics on the top) The '0' = the axon initiation point from the soma. Right: Bars (median) and whiskers (quartiles) of the F-Fex. values

in human cells. The AIS length (green background) was divided to 10 bins in individual cells for the bar plot of F-Fex. values. (C2) Measurement in a mouse Pvalb neuron (left). Right: The median (bars) and quartiles (whiskers) of mouse cells.

We compared the $F–F_{ex.c.}$ Kv1.2 immunofluorescence intensity values in soma (Fig. 23A1-2). A low but moderately higher immunofluorescence signal for the Kv1.2 channel was detected at the somatic extracellular membrane in humans (5.74, interquartile range (IQR) = 2.08–10.42, n = 60) than in mice (3.42, IQR = −2.66–5.30, n = 33) (p = 0.013; Fig. 23B1–B2). A low immunofluorescence signal was also detected in the cytoplasm (human: 4.47, IQR = −3.73–16.39; mouse: −6.59, IQR = −12.07–4.16) (p = 0.002). The Kv1.2 data are summarised in Figures 23C–E.

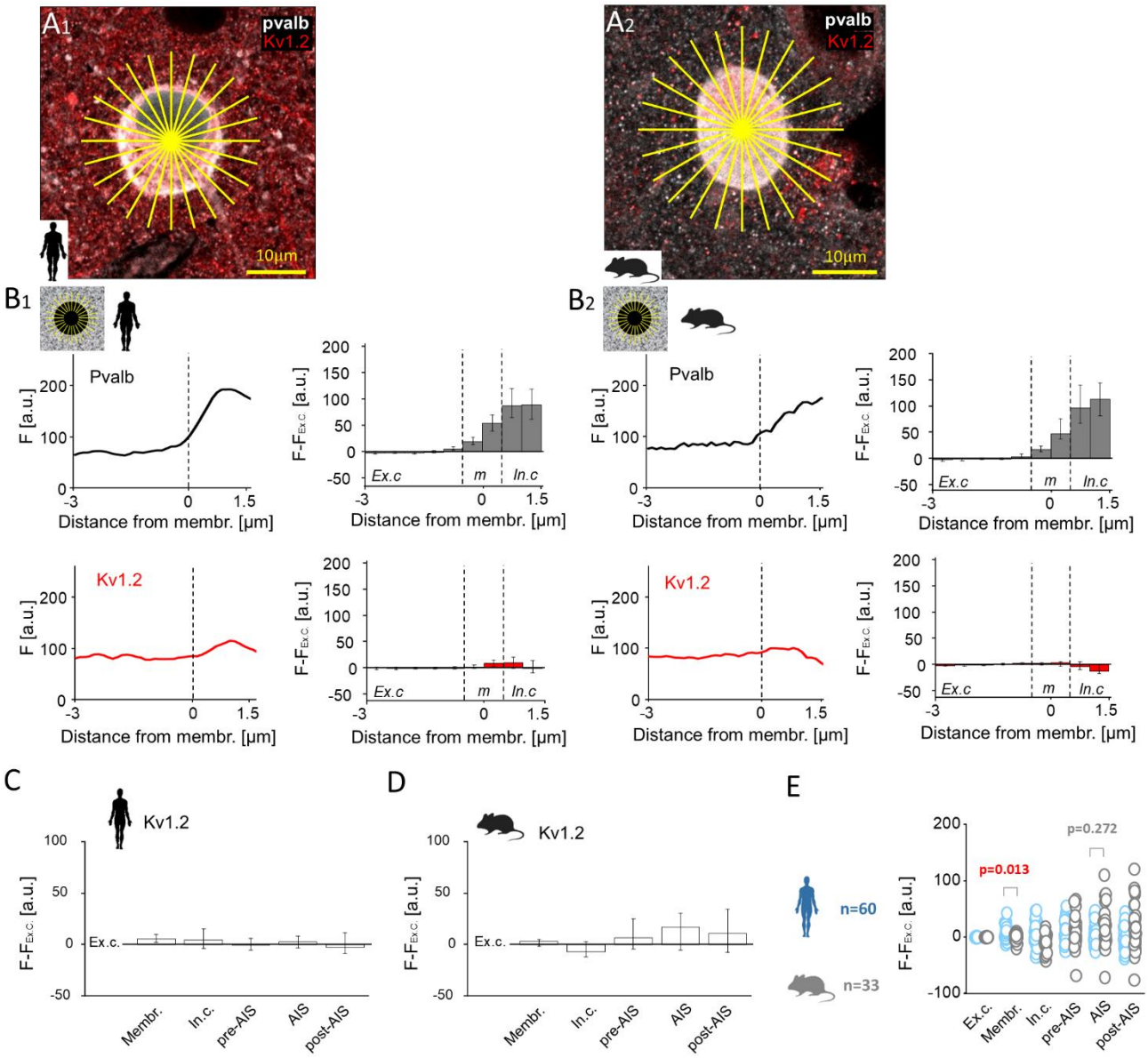

Figure 23. The soma is similarly low in Kv1.2 potassium channels in humans and mice. (A) Immunofluorescence analysis of Kv1.2 and Pvalb in cell soma in human (A1) and mouse (A2) cells. (The 24-line radial pattern is shown with yellow lines). (B) Pvalb (top, black line) and Kv1.2 (bottom, red line) signal along the radial lines in the cell soma. (B1) Left: The average fluorescence intensity values (F, in a.u.) in 24 pooled lines in a human cell (from -3 µm to +1.5 µm from the 0-point of the lines. Right: Bars (median) and whiskers (quartiles) of the Pvalb (grey) and Kv1.2. (red) F-Fex.c values in human cells. (B2) Left: Measurements in a mouse cell. Right: The median and quartiles in mouse cells. (C) The line analyses summary of human and mouse (D) Pvalb cells. Bars (median) and whiskers (quartiles) of F-Fex.c for Kv1.2 in the different cellular domains. (E) The F-Fex.c values in the human (blue) and the mouse (grey) Pvalb cells.

Human Pvalb neurons lack KCNA1 mRNA encoding Kv1.1 channels, and no difference in mRNA for KCNA2 encoding Kv1.2

We used patch-sequencing to measure the mRNA levels of key low-threshold ion channels responsible for modulating the AP firing threshold, including Kv1.1 and Kv1.2, in Pvalb neurons (Goldberg et al., 2008; Gu & Barry, 2011; Higgs & Spain, 2011; Kole et al., 2007; Li et al., 2014; Lorincz & Nusser, 2008). We performed whole-cell recordings, and cell nuclei were harvested for single-cell transcriptomic analysis (C. R. Cadwell, 2024; M. Shao, 2023). The mRNA quantification revealed mRNA for 6784 genes (IQR = 4872–7399) in humans (n = 21) and 3617 genes (IQR = 3173–4305) in mice (n = 16; Fig. 24A). The transcriptomic data of individual cells were uploaded to the Allen Institute neuron type identification server with an algorithm categorizing neocortex layer 2/3 neuron types by the genes expressed (https://knowledge.brain-map.org/mapmycells/process/). This enabled human and mouse Pvalb neuron identification also in cells with undetectable PVALB/Pvalb mRNA expression but positive expression for gene combinations indicating the Pvalb cell subtype. Utilising the identical criteria for Pvalb cell subtypes, we identified 21 and 16 Pvalb neurons in our human and mouse dataset, respectively. Further analysis of the cells was conducted for KCNA1, KCNA2, KCNC1, KCNC2, KCND1, KCNQ1, KCNQ2, KCNQ3, KCNQ4, KCNQ5, KCNK2, KCNK4 and KCK10 encoding major K channels in axon regulating AP firing threshold (Gu & Barry, 2011; Kole et al., 2007). In addition, mRNA levels for SCN8A/Scn8a expression, as well as the expression of housekeeping genes (ACTB/Actb, GAPDH/Gapdh, and SLC8A1/Slc8a1) were analyzed (Fig. 24A). The transcriptomic analysis demonstrated that human Pvalb neurons exhibited either an absence or undetectable mRNA expression for KCNA1 in all 21 cells, whereas Kcna1 was robustly expressed in 7 of 16 mouse Pvalb neurons. The mRNA level heatmap in Fig. 24A shows the gene expression (as transcripts per million [TPM]) for individual Pvalb neurons in humans and mice. PVALB/Pvalb mRNA expression was undetectable in 10 of 21 human neurons and 6 of 16 mouse neurons, which is consistent with the results from the Allen Institute's open access database for layer 2/3 Pvalb neurons. These findings suggest that PVALB mRNA expression is very low in certain Pvalb neurons. A comparison of KCNA1/Kcna1 mRNA expression between human (n = 21) and mouse cells (n = 16) revealed a significant difference ($p = 0.0016$, one-way MANOVA with the post hoc Bonferroni test). Furthermore, categorical comparisons (positive or negative mRNA expression)

demonstrated that KCNA1/Kcna1 expression in Pvalb neurons significantly differed between mice and humans ($p < 0.001$, chi-squared test following Benjamini–Hochberg adjustment at the 5% significance level; Fig. 24A). The mRNA expression levels of KCNA2/Kcna2 were found to be consistent across both species ($p = 0.970$). Additionally, the mRNA expression levels of KCNC1/Kcnc1 and KCNC2/Kcnc2 were found to be equally strong in both species ($p = 0.878$ and $p = 0.053$, respectively), with KCNC1/Kcnc1 encoding Kv.3.1 and Kv3.2 channels are characteristics of Pvalb interneurons (A. Chow, 1999; Hu et al., 2014), and they similarly exhibited low or absent expression of KCND1/Kcnd1 encoding Kv4.1 potassium channels (M. Martina, 1998) ($p = 0.541$). Human and mouse cells did not show difference in KCNK2/Kcnk2, KCNK4/Kcnk4 or KCNK10/Kcnk10 mRNA levels. In addition, while both species showed similar mRNA levels for KCNQ1/Kcnq1, KCNQ2/Kcnq2 and KCNQ4/Kcnq4 level, the human cells had higher levels of KCNQ3 ($p<0.001$) and KCNQ5 ($p<0.001$). Both human and mouse Pvalb cells strongly expressed mRNA for SCN8A/Scn8a encoding Nav1.6 sodium channels ($p = 0.086$). Moreover, all cells exhibited prominent mRNA levels for ACTB/Actb and GAPDH/Gapdh (Fig. 24A). Interestingly, the mRNA expression of SLC6A1/Slc6a1, encoding the gamma-aminobutyric acid (GABA) transporter 1, was lower in human neurons than in mouse neurons ($p = 0.002$). PVALB/Pvalb mRNA expression was undetectable in 10 of 21 human neurons and 6 of 16 mouse neurons, in line with the Allen Institute open access database results for layer 2/3 Pvalb neurons, demonstrating that PVALB mRNA expression is very low in certain Pvalb neuron subtypes in the human neocortex (Fig. 24B). The patch-sequencing results were in line with the averaged mRNA levels in Pvalb neuron types from the Allen Institute open access database (Fig. 24B). Results show absence of KCNA1/Kcna1 expression in human but not in mouse Pvalb neurons (human vs. mouse, $p<0.001$, and lower level of KCNA2/Kcna2 expression in human compared to mouse ($p=0.002$). Thus, both the patch-sequencing results as well as the Allen Institue open access data show that Kv1 channel genes are the only K-channel gene group in Pvalb neurons expressed at lower level in human compared to mouse neocortex. (One-way MANOVA with the post hoc Bonferroni test).

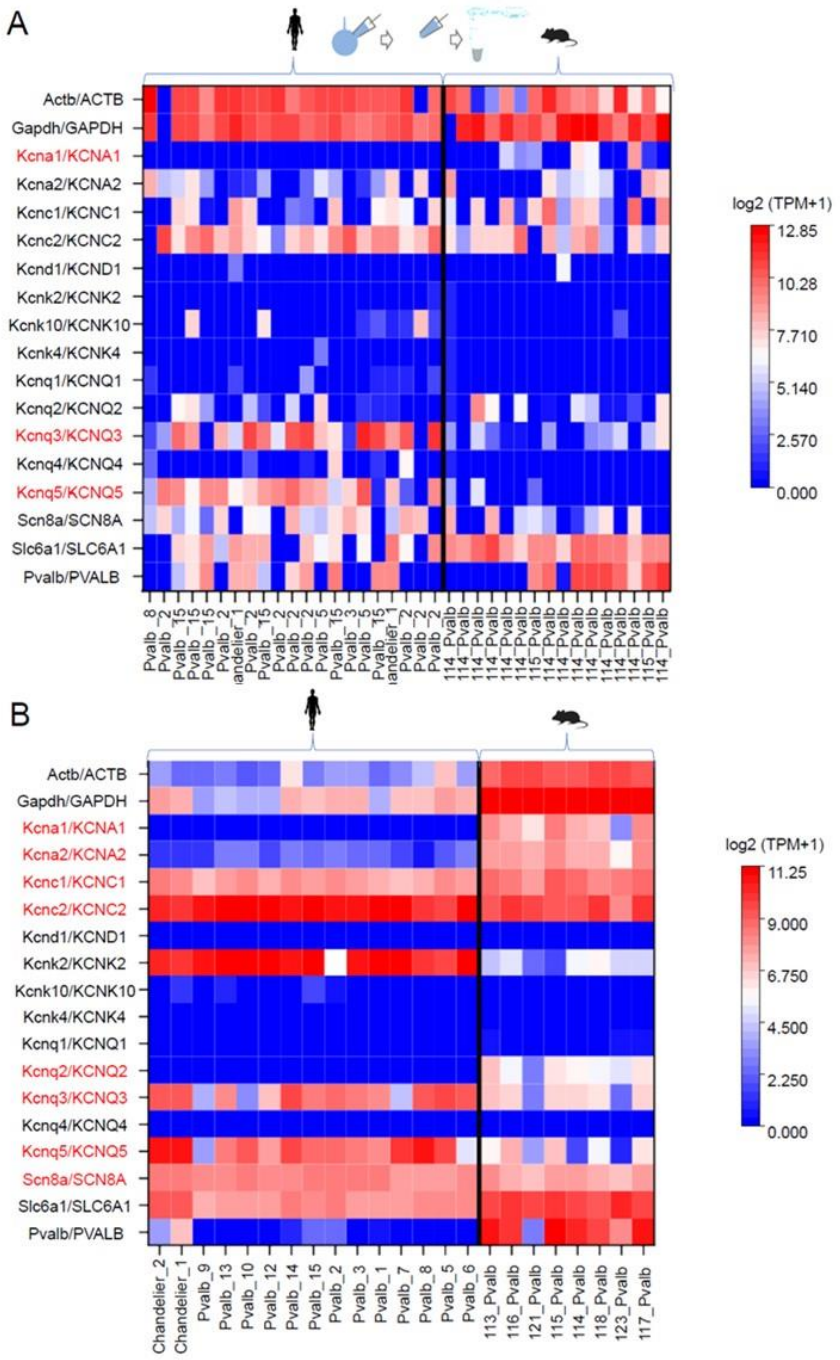

Figure 24. Human Pvalb neurons lack mRNA for KCNA1 encoding Kv1.1 channels, and express low level of Kv1.2 channel KCNA2 mRNA. (A) The heatmap presents the mRNA levels (TPM) in individual human (n = 21) and mouse (n = 16) PVALB/Pvalb neurons for genes encoding low-threshold channels in the AIS, as well as housekeeping genes GAPDH/Gapdh and ACTB/Actb. A quantitative and categorical analysis of the expression of KCNA1/Kcna1 in human and mouse cells shows that while there is a difference in TPM values, no such difference is observed in positive or negative gene expression for other ion channel genes. Similar KCNA2/Kcna2, KCNC1/Kcnc1, KCNC2/Kcnc2, KCNK2/Kcnk2, KCNK4/Kcnk4, KCNK10/Kcnk10 expression was observed in both species, and KCND1/Kcnd1 was

virtually not expressed in either human or mouse cells. Human cells expressed similar level of KCNQ1/Kcnq1, KCNQ2/Kcnq2, KCQN4/Kcnq4 but higher levels of KCNQ3/Kcnq3 and KCNQ5/Kcnq5 compared to mouse cells. Additionally, SCN8A/Scn8a, which encodes Nav1.6 channels, and SLC6A1/Slc6a1, which encodes GABA transporter type-1, were found to be abundant in both species. Human and mouse cells exhibited divergent mRNA expression of SCL6A1/Scl6a1, which encodes GABA transporter 1. Significant p-values comparing TPM values are presented in red (with genes, ordinate). (B) The Allen Institute database on Pvalb interneuron subtypes in the human neocortex layer 2/3 revealed a deficiency of KCNA1 mRNA in the human cells. The heatmap presents the TPM values (scaling on right) of the average values in 7 human and 8 mouse Pvalb neuron subtypes (abscissa) in layer 2/3 in the neocortex as identified by the dataset. Significant differences in KCNA1/Kcna1 TPM values were detected, and differences were noted when tested categorically.

Dendrotoxin, a Kv1 channel blocker, has a more pronounced effect on the AP firing threshold in mouse neurons than in human neurons

We investigated whether the blockade of Kv1 channels using dendrotoxin-K (DTXK) affects AP generation differently in human and mouse Pvalb neurons (Goldberg et al., 2008; Higgs & Spain, 2011). Following a 5-minute baseline whole-cell current–clamp recording period, the slices were exposed to 100nM DTXK for 10 minutes, after which the AP threshold was remeasured (Fig. 25A1-2). DTXK significantly altered the AP firing threshold in human neurons, shifting it from −41.5 mV (IQR = −44.0 to −39.0 mV) to −41.0 mV (IQR = −45.3 to −41.0 mV; n = 11 cells; p = 0.0459; mixed-design ANOVA and post hoc Wilcoxon test with Holm's correction). In mouse cells, the AP threshold was decreased from −32.0 mV (IQR = −35.5 to −28.5 mV) to −39.3 mV (IQR = −44.2 to −38.0 mV; n = 15 cells; p = 0.0007; mixed-design ANOVA and post hoc Wilcoxon test with Holm's correction). There was a significant difference in the change in AP threshold between baseline and in DTXK between human and mouse cells (p = 0.0009 for species interaction by mixed-design ANOVA) (Fig. 25B1-3). The AP threshold was more negative in humans than in mice at baseline (p = 0,0005), but there was no statistically significant difference between the species at DTXK (p = 0.0862) (mixed-design ANOVA and post hoc Mann–Whitney U tests between species at each time point, with Holm-adjusted p-values). Comparisons of the effect of DTXK across species revealed that, in addition to an AP threshold shift, the rheobase current was affected differently in mice than in humans (mixed-design ANOVA interaction, p = 0.0082). The rheobase current was reduced in mice (p = 0.0015), but not in humans (p = 0.4648; post hoc Wilcoxon tests with Holm's correction) (Fig. 25C1-3). Although the rest of the observed parameters failed to reveal a significant difference in the DTXK effect between humans and mice

(mixed-design ANOVA interaction, $p > 0.05$), Kv1 channel blockade was associated with a reduction in the amplitude of the action potential afterhyperpolarization (AP AHP) in mice, but not in human cells. This difference reflects the stronger somatic Kv1 channel contribution to AP AHP in mouse cells compared to human cells in control conditions. The AP half width was shorter in mice under baseline conditions but did not remain significantly shorter after the wash-in of DTXK, which reflects the blockade of K-current components of the AP in mice. Furthermore, DTXK was associated with a comparable decrease in the maximum positive peak value of the AP in both species. This suggests that the effect of DTXK on the AP occurs through a mechanism other than the direct current of the Kv1.1 channel. (A mixed-design ANOVA test with post hoc pairwise comparisons). In addition, DTXK was found to significantly increase input resistance in mouse cells, but not in human cells. Kv1.1 channels are activated in the cell soma by Vm depolarisation, which reduces Rin under baseline control conditions. Blocking these channels with DTXK increased the input resistance. Consistent with this finding, DTXK reduced species differences in membrane 'tau'. 'Tau' differed more between species under baseline control conditions than in the presence of DTXK. These results suggest that Kv1 channel activity is stronger in the AIS and soma of mouse neurons than in human Pvalb neurons.

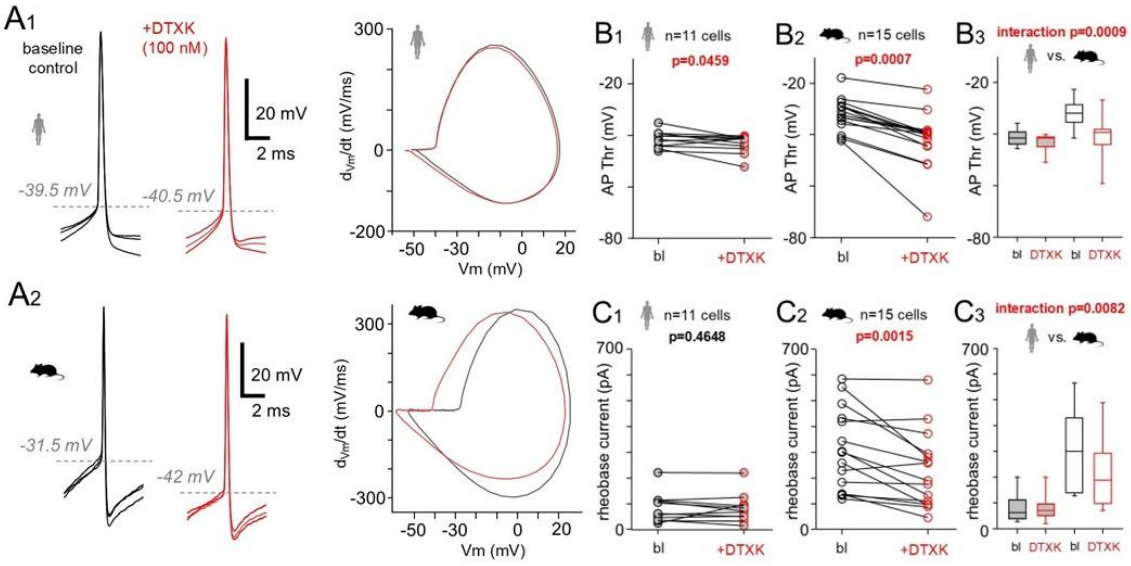

Figure 25. Kv1 channel blocker dendrotoxin lowers AP threshold in mouse but not in human Pvalb neurons. APs were recorded under baseline conditions (black traces) in current–clamp mode at −70 mV for 5 min, followed by application of 100 nM DTXK for 10 min, after which APs were evoked again (red traces). (A) APs and corresponding AP phase plots in baseline control and after DTXK application. (A1) Left: Three superimposed APs from a human

Pvalb cell. Right: Corresponding phase plots under control and DTXK conditions. (A2) Left: Superimposed APs recorded in a mouse Pvalb neuron. Right: Corresponding AP phase plots. (B) Effect of DTXK on the AP threshold in human (B1) and mouse (B2) neurons. (B3) Significant interaction between species and time on the measured values, meaning the DTXK treatment differs between human and mouse neurons. Box plots present the median, quartiles, and 5th and 95th percentiles. (C) Application of DTXK did not affect the rheobase current in human Pvalb neurons (C1), but it significantly reduced the current in mouse cells (C2). (C3) A significant interaction was found between species and time in the rheobase values, indicating that DTXK treatment differs between humans and mice.

Modeling shows the difference in action potential generation between human and mouse AIS

We created a computer model of a single cell that includes cable properties in the axon (and dendrites). This model copies the electrical properties of a human Pvalb cell that have been measured in real neurons. We then looked at how changes to the AIS length and AIS Kv1 channel content affect the AP firing threshold and the time it takes for an AP to be generated and for excitation to occur in the soma. We adjusted the electrical properties of the model cell to mimic the Vm waveforms and AP firing threshold of human Pvalb cells during the voltage steps, as shown in Fig.26A1–2. The model cell behaved like a whole human Pvalb cell (code h7), which has an AP with a voltage-sensitive axonal low-threshold Na current (mimicking Nav1.6 in the AIS), a high-threshold Na current (Nav1.2 at the soma and proximal dendrite), and a K current (mimicking Kv3.1 and Kv3.2 in the AIS, soma, and dendrite). It had three types of potassium current: one that was not affected by voltage, one that was M-type, and one that was Kir-type. These were found in the soma and dendrite (Szegedi et al., 2024). There was also a hyperpolarisation-activated non-specific cation current, Ih, in the soma and dendritic compartments. We also applied different levels of Kv1 activity in the AIS. In standard conditions, the model cell AIS length was 20 μm, and the initiation distance to the soma was 10 μm, and the AP firing threshold was −43 mV. First, we tested how much current was needed to trigger an AP firing threshold by changing the AIS lengths (10–30 μm), which is similar to the range found in the real-life investigation of Pvalb neurons. Increasing the AIS length linearly increased the Nav1.6 and Kv1 channel activity in the AIS (channel conductances gNav1.6 and gKv.1 were fixed at 20 nS/μm2 for both channels). The axons had a diameter of 0.8 μm and longitudinal resistance (Ra) of 0.9 MΩ·μm. When the AIS was made longer (10, 20 or 30 μm), the AP firing threshold (which is measured using a 250-ms square-pulse current in the soma at −70 mV) in the model cell went down from −36.8 mV to −42.3 and −45.2

mV (Fig.26B1–2). This shows that the Pvalb cell AIS length range seen in this study can have a big effect on the AP firing threshold. In the second simulation, we changed the activity of certain channels (Kv1) in a structure called the AIS while keeping the AIS length (20 μm) and location along the axon (10 μm from the cell body, Ra = 0.9 MΩ·μm) the same, as well as the gNav1.6 density (20 nS/μm^2). We simulated AP generation by depolarising the voltage steps in the cell to define the AP firing threshold as we had done before. When we increased the gKv1 from 0 nS/μm^2 to 5, 10, and 15 nS/μm^2 in the AIS (Fig.26C1–2), the AP firing threshold increased from −45.3 mV to −44.2, −42.4, and −41.6 mV, respectively (Fig. 26D). This simulation showed that increasing the activity of the Kv1 channel in the AIS (without changing the geometry of the AIS) increases the AP firing threshold. Finally, we used the model cell to understand how changes to the AP firing threshold, caused by alterations to the AIS length and Kv1 content, affect the time delay in Pvalb neurons when they are stimulated by the synapse in the soma. The aim of the simulation was to find out why human Pvalb neurons, compared with mouse Pvalb neurons, with a slower somatic membrane tau (Fig. 26E1) but lower AP firing threshold (Fig. 26E2), can fire APs with an equal or shorter time lag to the fixed-amplitude excitatory current in the soma (Fig. 26E3-4) (Szegedi et al., 2017). In the model neuron, we created an excitatory postsynaptic current (EPSC) in the soma at −70 mV and increased its peak amplitude bit by bit to make a gradually increasing excitatory postsynaptic potential (EPSP) that finally reached the AP firing threshold. The EPSC was generated with peak conductance from 6 to 11 nS with an incremental step of 0.25 nS, reaching the AP firing threshold with the human-type and mouse-type AIS with EPSC conductance values of 6.75 and 8.5 nS, respectively (Fig. 26F1–3). Shifting from the mouse-type AIS (Kv1 density 20 nS/μm^2, AIS length 10 μm) to the human-type AIS (Kv1 density 0 nS/μm^2, AIS length 30 μm) shortened the time taken for AP generation compared with the EPSP-AP time lag generated with a fixed EPSC strength (Fig. 26F2-3). The EPSP-AP time lag simulation with different AIS lengths and varying levels of Kv1 in the AIS is shown in the heatmap in Fig. 26G. The simulation showed the minimum and maximum time lags for AP generation to be 4.8 and 7.8 ms, respectively, for a fixed EPSC strength (8.5 nS, the AP firing threshold in the model cell) in the model cell.

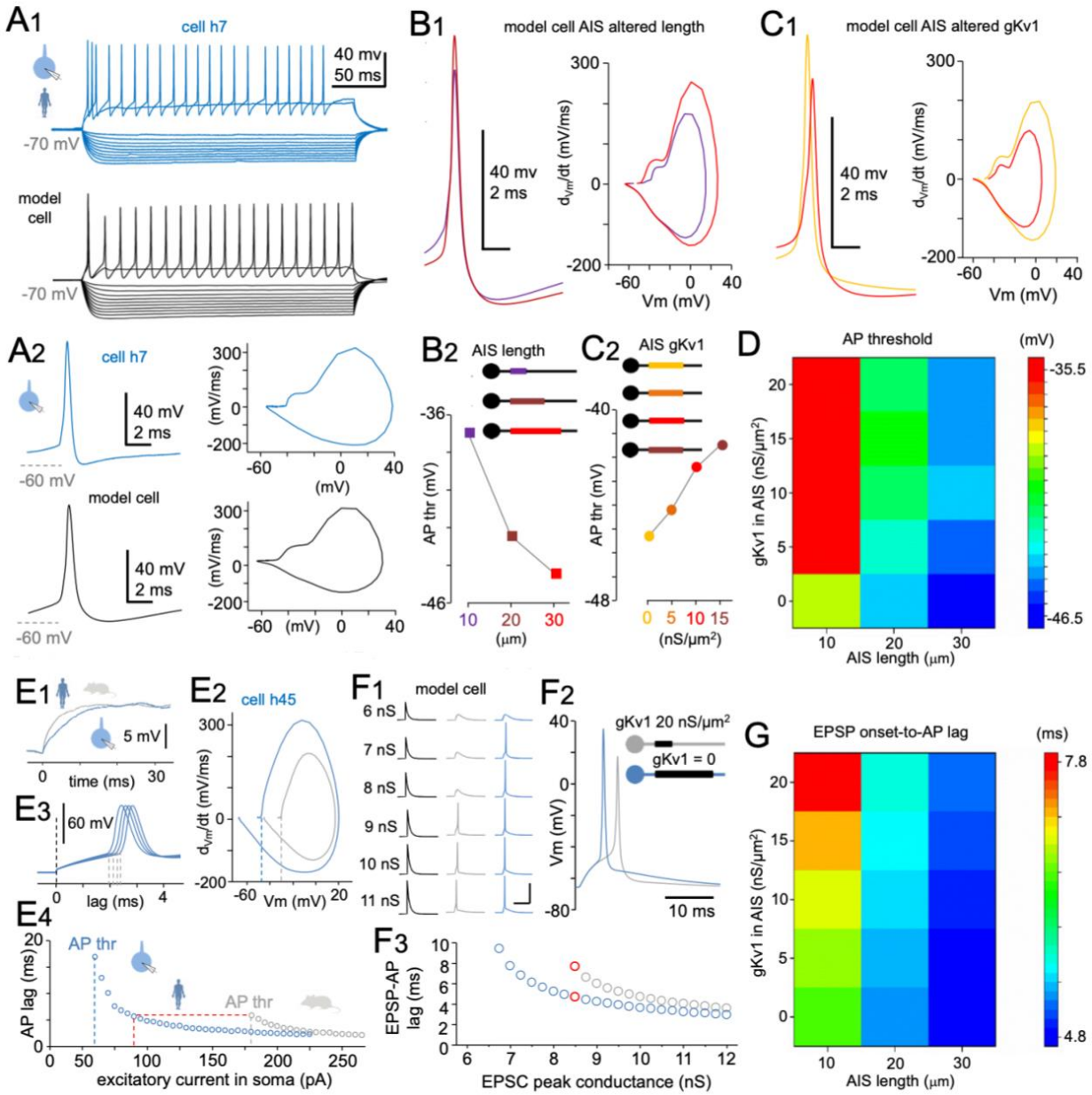

Figure 26. Computational modeling shows that a human-type AIS lowers the action potential threshold and reduces spike latency in fast-spiking neurons. (A1) Membrane potential (Vm) responses in a human Pvalb neuron (recorded, blue) and the corresponding model cell (gray) during current steps from −200 to +200 pA. (A2) Left: the first suprathreshold AP from the recorded (blue) and modeled (gray) cells. Right: phase plots of these APs. (B1) Model APs and phase plots with AIS lengths of 10 µm (purple) and 30 µm (red). (B2) AP thresholds simulated for AIS lengths of 10 µm (purple), 20 µm (brown), and 30 µm (red), as shown in the schematic. (C1) Effect of Kv1 conductance in the AIS on AP waveform and phase plot: gKv1 = 0 (yellow) and 15 nS/µm² (red). (C2) Simulated AP thresholds at different Kv1 densities (0–15 nS/µm²) with Nav1.6 = 20 nS/µm², AIS = 20 µm long, and 10 µm from soma. (D) Combined effect of AIS length and Kv1 activity on AP threshold. The heatmap shows threshold values (color scale at right); the total

simulated difference between minimum and maximum AP threshold was 11 mV. (E1–E2) Human Pvalb neurons (blue) show slower membrane depolarization but lower AP threshold compared with mouse neurons (gray). (E3) Four example traces illustrating AP generation lag between the depolarizing step onset (black dotted lines) and AP onset (gray dotted line; onset defined as 10 mV/ms rise). (E4) AP generation lag in human (blue) and mouse (gray) neurons plotted against depolarizing current amplitude. (F1) The human-type AIS lowers the AP threshold for EPSC-evoked firing in the model. Vm traces show EPSPs (6–11 nS peak conductance, black) and corresponding APs for human (blue) and mouse (gray) AISs. Scale: 40 ms, 50 mV. (F2) The human-type AIS shortens the EPSP-to-spike delay. Traces show EPSPs with equal EPSC strength (8.5 nS) in models with human (blue) and mouse (gray) AISs. (F3) Spike latency as a function of EPSC conductance in human-type (blue) and mouse-type (gray) AIS models; responses to 8.5 nS EPSC are highlighted (red). (G) Heatmap showing the combined effect of AIS length (x-axis) and Kv1 activity (y-axis) on spike latency in response to a fixed 8.5 nS EPSC. Color calibration (ms) is shown on the right.

Discussion

Research study I: Somatic HCN channels facilitate the input-output transformation in human fast-spiking interneurons

This study provides compelling evidence that human neocortical fast-spiking basket cells are characterized by a somatic leak current mediated by hyperpolarization-activated cyclic nucleotide-gated (HCN) channels, in contrast to their rodent counterparts. In human interneurons, the somatic membrane exhibits a marked voltage sag during hyperpolarizing current injection, a signature of active perisomatic HCN channels. This sag was abolished by the application of ZD7288, and accompanied by a hyperpolarization of the resting membrane potential. Complementary outside-out patch recordings (Szegedi et al., 2023) and high-resolution immunohistochemistry confirmed the membrane localization of HCN1 and HCN2 channel isoforms at the soma of human Pvalb neurons. These features were largely absent in rodent neurons, which lacked prominent sag potentials and displayed weaker or intracellular HCN labeling.

These findings indicate that somatic HCN channels play a critical physiological role in compensating for the relatively slow passive membrane kinetics of human fast-spiking neurons. Compared to rodents, human basket cells exhibit higher input resistance and reduced resting ion leak, which together prolong the membrane time constant. Without compensatory mechanisms, such electrical sluggishness would hinder the rapid transformation of synaptic input into action

potentials—an essential function for inhibitory interneurons. Our computational modeling supports this interpretation, demonstrating that somatic HCN conductance accelerates the kinetics of EPSP-spike coupling and enhances the responsiveness of human neurons to excitatory drive.

Furthermore, HCN channels in human neurons appear to be under neuromodulatory control, offering a dynamic mechanism to fine-tune excitability. Modulation of HCN activity through intracellular signaling pathways, including second messenger cascades, could enable rapid transitions between high and low excitability states in response to changing network demands. This modulatory flexibility adds to the functional advantages of somatic HCN channels in primate cortical interneurons.

Interestingly, similar features—such as high input resistance and large sag potentials—have been observed in macaque fast-spiking interneurons, suggesting that robust somatic HCN expression is a conserved adaptation among primates. The presence of such channels across developmental stages and cortical regions further supports their integral role in primate neuronal physiology.

The benefits of somatic HCN channels extend beyond individual neurons. By ensuring rapid EPSP-to-spike transformation, these channels contribute to the temporal precision of cortical inhibition, supporting the synchronization of network oscillations and the fidelity of information processing. Given the greater synaptic distances and circuit complexity in the primate cortex, even a modest acceleration in single-cell response time may exert significant effects at the network level. Thus, the evolutionary acquisition of somatic HCN channels in human interneurons can be viewed as a key adaptation to the demands of expanded and functionally diverse cortical circuits.

Research study II: Kir Channels similarly regulate intrinsic excitability in Human and Mouse Pvalb Neurons despite their different input resistances

In this study, we investigated the role of inward-rectifier potassium (Kir) channels in regulating the excitability of parvalbumin-expressing interneurons across various species. Despite the markedly higher baseline input resistance observed in human Pvalb neurons, both human and mouse cells exhibited similar relative reductions in input resistance in response to membrane

hyperpolarization. This voltage-dependent rectification, which was abolished by the Kir channel blocker barium, indicates a conserved inhibitory mechanism mediated by Kir channels.

Transcriptomic profiling confirmed strong expression of Kir3.1 and Kir3.2 subunits in both species. While the overall expression levels were higher in human neurons, mouse cells displayed greater diversity in Kir subunit expression, including Kir3.3 and several Kir2 family members. Immunohistochemistry and dSTORM imaging corroborated these findings, revealing somatic membrane localization of Kir3.1 and Kir3.2 in both human and mouse Pvalb neurons.

Our computational modeling revealed a key species-specific difference in the functional consequences of Kir channel activity: in human neurons, lower Kir conductance was sufficient to produce the same degree of resistance rectification as in mouse cells. This efficiency is attributable to the higher passive membrane resistance in human neurons and may represent a neuroeconomical strategy for conserving energy. Fast-spiking interneurons are among the most metabolically demanding cells in the brain, and minimizing ion flux through efficient inhibition mechanisms likely reduces ATP consumption associated with ion gradient maintenance.

Kir channels contribute to neuronal inhibition not only through membrane hyperpolarization but also via shunting inhibition. Their activation dampens EPSPs by increasing membrane conductance, thereby reducing the depolarizing effect of excitatory synaptic inputs. Importantly, these effects are modulated by neuromodulatory receptors, including opioid and GABA-B receptors. Activation of these receptors induces Kir-mediated hyperpolarization and shunting, highlighting a convergent mechanism for regulating interneuron excitability in response to external stimuli.

Interestingly, we observed substantial cell-to-cell variability in the strength of Kir-mediated inhibition, particularly among human neurons. This variability may reflect intrinsic differences in Kir expression or channel modulation, or it could arise from activity-dependent plasticity mechanisms. The potential for dynamic regulation of Kir channel activity offers an additional layer of flexibility for cortical inhibitory circuits.

Altogether, our findings suggest that Kir-mediated control of excitability is a conserved and integral feature of Pvalb interneurons. However, interspecies differences in conductance

requirements and subunit expression point to evolutionary refinements in how this inhibitory mechanism is deployed.

Research study III: AIS adaptations set a lower AP threshold in human Pvalb neurons

One of the most striking findings of this study is the lower action potential (AP) threshold observed in human Pvalb interneurons compared to their rodent counterparts. This difference is particularly significant given the slower membrane time constants and higher input resistance in human cells, which would otherwise counteract rapid spike generation. The lower AP threshold thus appears to be a compensatory mechanism that ensures fast and reliable firing in the context of electrically sluggish somatic properties.

We identified two key structural and molecular adaptations that underlie this shift in excitability: an elongated axon initial segment (AIS) and reduced expression of Kv1-type potassium channels. Immunohistochemical analysis revealed that the AIS in human Pvalb neurons is significantly longer than in mouse neurons, extending further from the soma. This elongation increases the surface area available for voltage-gated sodium channel clustering, enhancing the likelihood of AP initiation.

At the same time, human AISs lack Kv1.1 channels and show minimal Kv1.2 expression, as demonstrated by both immunolabeling and transcriptomic data. These channels are known to raise the threshold for AP generation by stabilizing the membrane potential. Their absence in human AISs removes a major inhibitory influence on spike initiation. Computational modeling confirmed that the combination of AIS elongation and reduced Kv1 conductance significantly lowers AP threshold.

Although the origin point of the AIS relative to the soma did not differ between species, the extended AIS length in human neurons was sufficient to produce a pronounced shift in excitability. Importantly, our data suggest that axon diameter does not account for the observed interspecies differences, as similar diameters were found across species. Moreover, larger axon diameters tend to decrease axial resistance but can counteract the excitability gains from increased ion channel density.

In addition to structural features, plasticity of the AIS may contribute to cell-to-cell variability in AP thresholds. The AIS is a dynamic compartment whose length and channel composition can be modulated by activity and developmental cues. While such plasticity has been well characterized in rodent models, further research is needed to determine whether similar mechanisms operate in the human cortex.

Taken together, these findings suggest that human Pvalb neurons have evolved a suite of adaptations to maintain fast-spiking behavior despite intrinsic electrical constraints. By lowering the AP threshold through AIS elongation and reduced potassium channel expression, these neurons preserve the speed and precision required for effective cortical inhibition.

Limitations and Future Directions

This study was limited by the inherent heterogeneity of human tissue samples, which were derived from patients with varying ages, sexes, and clinical backgrounds. Such variability may introduce confounding factors that are difficult to control. Additionally, the lack of transgenic tools in human tissue constrains the ability to perform precise genetic manipulations, such as gene knockouts or overexpression studies.

Future work should aim to incorporate organotypic slice cultures of human cortex, which may allow for targeted viral gene delivery. This approach would enable visualization of specific cell types, functional modulation via optogenetics or chemogenetics, and gene editing techniques to dissect the roles of ion channels and structural features in human neurons. The ability to experimentally manipulate genes such as Kv1.1 or Kir3.1 in human tissue would significantly advance our understanding of their functional contributions.

As genetic and molecular tools become increasingly available for use in human-derived tissue, it will be possible to explore the plasticity of the AIS, ion channel dynamics, and cell-type–specific adaptations in greater detail. These advances will not only enhance our understanding of human brain function but also improve the translational relevance of preclinical models by highlighting where rodent systems may diverge from human neurobiology.

Although we are not certain why our dataset occasionally shows zero levels for some common genes, we would like to suggest three possible explanations. The first possibility is that the gene expression in mammalian cells is often bursty and stochastic rather than continuous, and

mRNA TPM levels can vary 100-fold between transcription bursts and silent periods (Robles-Rebollo et al., 2022; Tukacs et al., 2024). This natural fluctuation of individual gene expression rates can introduce noise into the overall dataset. Although the phenomenon is well recognized in fields such as cancer research and molecular biology, it is not emphasized in neuroscience. This feature may also partly explain the occasional weak quantitative correlation between mRNA and protein. The second possibility is that the mRNA level is too low for our method to detect it. However, we consider it unlikely that the mRNA would not be detected with 4 million reads. We emphasize that we only accept cells with a high number of active genes, which is a standard for high-quality patch sequencing. Furthermore, it is noteworthy that some cells with a very high number of active genes, e.g., 8,500, show a level of 0 for the GAT-1 or PVALB mRNA. The third possibility is that some mRNA has degraded, or the cDNA conversion was unsuccessful for that particular mRNA. This would mean that, for reasons unknown to us, our system might lose mRNA or fail to convert it to cDNA for some specific genes. However, we stress that we have no evidence supporting this possibility. It is possible that some mRNA degradation occurs in some samples, leading to the disappearance of mRNA from genes that are already naturally present in low amounts in the sample. We also mention the latter possibility in the manuscript.

In conclusion, this thesis underscores the importance of species-specific adaptations in the cellular physiology of neocortical interneurons. Differences in ion channel expression, membrane properties, and axonal architecture illustrate how homologous cell types can evolve distinct mechanisms to meet the computational demands of the brain. These findings have broad implications for understanding the evolution of cortical circuits and for designing therapeutics that are effective in the human context.

Summary

Significant species-specific differences in the properties of mammalian neurons have been well documented over the years. However, much of our understanding of cortical circuit function and information processing in the human brain still depends on data from rodents and other experimental animals. This knowledge gap is especially notable for the neocortex—the brain region that supports the most complex cognitive functions and exhibits the greatest evolutionary divergence. Microanatomical and molecular differences among homologous neuron types (cells sharing similar developmental origins and cortical locations across species) are particularly prominent in the neocortical mantle. Yet, the functional importance of these differences remains poorly understood.

In this thesis, we examined the electrophysiological properties of human and mouse fast-spiking GABAergic basket cells, which are among the most prominent types of inhibitory interneurons in the cortex. Through detailed analysis of membrane potential responses to current injections, pharmacological blockade, and immunohistochemical staining, we found substantial differences in ion channel composition at the soma. Notably, human neocortical basket cells exhibited high expression of HCN1 and HCN2 channel isoforms at the somatic membrane, while rodent basket cells showed only sparse somatic expression. Pharmacological experiments using ZD7288 confirmed that these HCN channels help maintain the resting membrane potential and modulate cell excitability. They also speed up membrane potential kinetics, reducing the delay between excitatory postsynaptic potentials and action potential generation. This is especially important because, without HCN channels, human fast-spiking neurons display low persistent ion leak and inherently slower membrane potential changes compared to mouse neurons. Computational modeling supported these findings, demonstrating that somatic HCN conductance alone is enough to enhance the speed of input–output transformation in human interneurons, making their temporal precision closer to that of rodent cells.

Overall, our findings show that human and mouse fast-spiking interneurons differ in their somatic ion channel makeup, which directly affects the speed and accuracy of synaptic integration and spike initiation. The presence of somatic HCN channels seems to be an adaptive feature that helps human fast-spiking neurons stay responsive quickly despite their different passive membrane

properties. We also looked at how inwardly rectifying potassium (Kir) channels regulate intrinsic excitability. Human neocortical interneurons have higher baseline input resistance compared to rodents, mainly because of less passive ion leak across the membrane, which makes voltage responses to synaptic input larger. Despite this, our whole-cell patch-clamp recordings showed that both human and mouse Pvalb neurons have similar proportional decreases in input resistance when the membrane hyperpolarizes, driven by Kir channel activation. This subthreshold regulation was blocked by barium, confirming Kir channels are involved in both species. Molecular analysis using patch-sequencing revealed strong expression of Kir3.1 and Kir3.2 subunits in Pvalb neurons from both humans and mice. Additionally, confocal and dSTORM super-resolution imaging confirmed these channels' presence on the membrane, reinforcing their conserved role in controlling subthreshold excitability. Though human neurons have higher overall input resistance, they need less Kir conductance to produce the same level of voltage-dependent rectification, indicating a more efficient inhibitory mechanism that might reflect evolutionary optimization for energy efficiency. Lastly, we explored the mechanisms behind differences in action potential thresholds between human and mouse fast-spiking interneurons. Whole-cell recordings showed that human Pvalb neurons fire at lower thresholds than mouse neurons, supporting their role as fast-in–fast-out units despite slower somatic membrane dynamics. Detailed analysis found that human neurons have a longer axon initial segment (AIS)—the region where action potentials start—and lack the low-voltage activated inhibitory Kv1.1 and Kv1.2 potassium channels that are prominently found in the AIS of mouse neurons. Computational models demonstrated that this human-specific AIS structure, along with the absence of Kv1 channels, lowers the AP threshold and decreases spike latency, compensating for slower membrane potential changes at the soma.

Taken together, these findings emphasize how structural and molecular adaptations allow human Pvalb-expressing interneurons to sustain rapid and accurate inhibitory signaling. By incorporating somatic HCN channels, an extended AIS, and specific ion channel expression, these neurons maintain high-speed information processing in the enlarged and metabolically demanding human neocortex.

Összefoglaló

Az emlős neuronok tulajdonságaikat tekintve jelentős faji különbségek figyelhetők meg, amit több adat is alátámaszt. Az emberi agy áramköri aktivitására és információfeldolgozására vonatkozó elméletek nagyrészt rágcsálókon és más kísérleti állatokon kapott eredményeken alapulnak. Ez az ismereti hiányosság különösen jelentős a neokortex, a legösszetettebb neuronális műveletekért felelős és a legnagyobb evolúciós eltérést mutató agyterület megértése szempontjából. A homológ neuronok (azaz a különböző emlősökben hasonló lokalizációjú és fejlődési eredetű neurontípusok) mikroanatómiai és molekuláris különbségei a legnyilvánvalóbbak a neokortikális kéregben. Ezeknek a különbségeknek az oka és következménye azonban továbbra is tisztázatlan.

Jelen tézisben az emberi és egér gyorsan tüzelő GABAerg kosársejtek elektrofiziológiai tulajdonságait vizsgáltuk, amelyek az agykéregben a legnagyobb számban előforduló gátló interneuronok közé tartoznak. Az áraminjekcióra adott membránpotenciál-válaszok, a farmakológiailag izolált szomatikus áramok és az immunhisztokémiai jelölés részletes elemzését végeztük el. Munkánk feltárta a hiperpolarizációval aktivált ciklikus nukleotid-aktivált kation (HCN) csatorna HCN1 és HCN2 izoformájának nagymértékű expresszióját a humán neokortikális kosársejtekben, ellenben a rágcsálók kosársejtjeinek szoma membránjában az expressziója nem jellemző. Az ioncsatorna antagonistájával (ZD7288) végzett kísérletek azt mutatták, hogy a HCN csatornák jelenléte az emberi neuronokban elősegíti a nyugalmi membránpotenciál fenntartását és a sejt szóma által mutatott gerjeszthetőségének intenzitását. Továbbá megfigyeltük, hogy ezek a csatornák felgyorsítják a szomatikus membránpotenciál kinetikáját, és csökkentik a gerjesztő posztszinaptikus potenciálok megjelenése és az ezt követő akciós potenciálok generálása közötti időintervallumot. Ezek az eredmények azért fontosak, mert a HCN-csatornákat nem tartalmazó humán gyorsan tüzelő neuronok szomája kismértékű ionszivárgást és lassú membránpotenciál kinetikát mutat az egér gyorsan tüzelő neuronokhoz képest. A számítógépes modellezés alátámasztotta ezeket az eredményeket, bizonyítva, hogy a szomatikus HCN-expresszió önmagában elegendő az emberi interneuronok bemeneti-kimeneti átalakulásának sebességének növeléséhez, így azok időbeli pontossága közelebb kerül a rágcsáló sejtekéhez.

Összességében eredményeink azt mutatják, hogy az emberi és egér neokortikális gyorsan tüzelő interneuronok szomatikus ioncsatorna-összetétele eltérő, ami közvetlenül befolyásolja a szinaptikus integráció és a tüzelési mintázat kialakulásának sebességét és pontosságát. A szomatikus HCN-csatornák jelenléte úgy tűnik, hogy egy adaptív tulajdonság, amely segít az emberi gyorsan tüzelő interneuronoknak a különböző passzív membrán tulajdonságaik ellenére is gyorsan reagálni. Megvizsgáltuk azt is, hogy a befelé egyenirányítókálium (Kir) csatornák hogyan szabályozzák a belső gerjeszthetőséget. Az emberi neokortikális interneuronok bemeneti ellenállása nagyobb, mint a rágcsálóké, főként azért, mert a membránon keresztül a passzív ion szivárgás alacsonyabb, így a szinaptikus serkentésre nagyobb feszültségválasszal reagál. Ennek ellenére a patch-clamp méréseink azt mutatták, hogy mind az emberi, mind az egér Pvalb neuronokban a bemeneti ellenállás csökkenése hasonló membrán hiperpolarizálóra, amit a Kir csatorna aktiválása okoz. Ezt a küszöbérték alatti szabályozást a báriumion blokkolta, ami megerősítette, hogy a Kir csatornák mindkét fajban szerepet játszanak a bemeneti ellenállás szabályzásában. A patch-Seq molekuláris elemzés jelentős Kir3.1 és Kir3.2 expressziót mutatott ki mind az emberi, mind az egér Pvalb neuronokban. Ezenkívül a konfokális és dSTORM szuperfelbontású képalkotás megerősítette ezeknek a csatornáknak a jelenlétét a szomatikus membránban, alátámasztva szerepüket a küszöbérték alatti gerjeszthetőség szabályozásában. Bár az emberi idegsejtek összességében nagyobb bemeneti ellenállással rendelkeznek, ugyanolyan szintű feszültségfüggő rektifikációhoz kisebb mértékű Kir-csatorna aktiválódára van szükségük, ami hatékonyabb gátló mechanizmust jelent. Végül megvizsgáltuk az emberi és egér gyors tüzelésű interneuronok akciós potenciál küszöbértékének különbségei mögött álló mechanizmusokat. A egészsejtes elvezetések felvételei azt mutatták, hogy az emberi Pvalb neuronok alacsonyabb küszöbértéknél tüzelnek, mint az egér neuronok, ami elősegíti a gyors be- és kimeneti gátló áramkörök működését, annak ellenére, hogy szomatikus membrán dinamikájuk lassabb. A részletes elemzés kimutatta, hogy az emberi neuronok hosszabb axon kezdeti szegmenssel (AIS) rendelkeznek – ez az a régió, ahol az akciós potenciálok létrejönnek – és hiányoznak belőlük az alacsony feszültségnél aktiválódó Kv1.1 és Kv1.2 káliumcsatornák, amelyek az egér neuronok AIS-ében jelentős számban megtalálhatóak. Számítógépes modelezéssel kimutattuk, hogy ez az emberre jellemző AIS-szerkezet, valamint a Kv1-csatornák hiánya csökkenti az AP küszöbértékét és az akciós potenciál késleltetését, kompenzálva a szomatikus membrán lassabb potenciálváltozásait.

Összességében ezek az eredmények azt bizonyítják, hogy a szerkezeti és molekuláris adaptációk hogyan teszik lehetővé az emberi Pvalb-t expresszáló interneuronok számára a gyors és pontos gátló jelátvitel fenntartását. A szomatikus HCN-csatornák, a kiterjesztett AIS és a specifikus ioncsatorna-expresszió hozzájárul, hogy ezek a neuronok fenntartsák a nagy sebességű információfeldolgozást a nagyobb és metabolikusan intenzívebb emberi neokortexben.

Acknowledgements

I am grateful to Dr. Karri Lamsa for allowing me to join his research group. He also contributed to and enthusiastically supported my PhD research. I would like to thank Dr. Viktor Szegedi for his guidance as my supervisor, for his help over the years, and for always being available to answer my questions.

I am grateful to the former and current members of the research group who participated in the experiments that formed the basis of my dissertation: Dr. Ádám Tiszlavicz, Dr. Szabina Horváth-Furdan, Dr. Abdennour Doiuda, Dr. Attila Szűcs, Orsolya Bérczi, Milán Marencsik, Krisztián Péli, and Dr. Melinda Paizs. I would also like to thank Dr. Pál Barzó and Dr. Gábor Hutóczki for providing human brain tissue samples, as well as Prof. Gábor Tamás's research group for their cooperation and assistance. I am grateful to Dr. Miklós Erdélyi and Dr. Bálint Kovács for their joint work and cooperation. In addition, I would like to thank the current and former staff of the laboratory and the Department of Physiology, Anatomy and Neuroscience, as well as the Hungarian Centre of Excellence for Molecular Medicine, for their friendly atmosphere.

I would like to thank my parents for their indispensable support during my studies, and my siblings and friends for standing by me and helping me with my work.

References

A. Chow, A. E., C. Farb, M. S. Nadal, A. Ozaita, D. Lau, E. Welker, B. Rudy. (1999). K(+) channel expression distinguishes subpopulations of parvalbumin- and somatostatin-containing neocortical interneurons. *J Neurosci*, *19*, 9332-9345.

Albertson, A. J., Bohannon, A. S., & Hablitz, J. J. (2017). HCN Channel Modulation of Synaptic Integration in GABAergic Interneurons in Malformed Rat Neocortex. *Front Cell Neurosci*, *11*, 109. https://doi.org/10.3389/fncel.2017.00109

Anderson, E. M., Demis, S., D'Acquisto, H., Engelhardt, A., & Hearing, M. (2021). The Role of Parvalbumin Interneuron GIRK Signaling in the Regulation of Affect and Cognition in Male and Female Mice. *Front Behav Neurosci*, *15*, 621751. https://doi.org/10.3389/fnbeh.2021.621751

Bakken, T. E., Jorstad, N. L., Hu, Q., Lake, B. B., Tian, W., Kalmbach, B. E., Crow, M., Hodge, R. D., Krienen, F. M., Sorensen, S. A., Eggermont, J., Yao, Z., Aevermann, B. D., Aldridge, A. I., Bartlett, A., Bertagnolli, D., Casper, T., Castanon, R. G., Crichton, K., . . . Lein, E. S. (2021). Comparative cellular analysis of motor cortex in human, marmoset and mouse. *Nature*, *598*(7879), 111-119. https://doi.org/10.1038/s41586-021-03465-8

Bakos, E., Tiszlavicz, A., Szegedi, V., Douida, A., Furdan, S., Welter, D. K., Landry, J. M., Bende, B., Hutoczki, G., Barzo, P., Tamas, G., Benes, V., Szucs, A., & Lamsa, K. (2025). Specialized axon initial segment enables low firing threshold and rapid action potential output in fast-spiking interneurons of the human neocortex. *bioRxiv*. https://doi.org/10.1101/2024.10.28.620622

Barton, R. A. (2007). Evolutionary specialization in mammalian cortical structure. *J Evol Biol*, *20*(4), 1504-1511. https://doi.org/10.1111/j.1420-9101.2007.01330.x

C. R. Cadwell, A. S. T. (2024). Patch-seq: Multimodal Profiling of Single-Cell Morphology, Electrophysiology, and Gene Expression. *Methods Mol Biol*, *2752*, 227-243.

Campagnola, L., Seeman, S. C., Chartrand, T., Kim, L., Hoggarth, A., Gamlin, C., Ito, S., Trinh, J., Davoudian, P., Radaelli, C., Kim, M. H., Hage, T., Braun, T., Alfiler, L., Andrade, J., Bohn, P., Dalley, R., Henry, A., Kebede, S., . . . Jarsky, T. (2022). Local connectivity and synaptic dynamics in mouse and human neocortex. *Science*, *375*(6585), eabj5861. https://doi.org/10.1126/science.abj5861

Castillo-Morales, A., Monzon-Sandoval, J., de Sousa, A. A., Urrutia, A. O., & Gutierrez, H. (2016). Neocortex expansion is linked to size variations in gene families with chemotaxis, cell-cell signalling and immune response functions in mammals. *Open Biol*, *6*(10). https://doi.org/10.1098/rsob.160132

Chen W, Z. J., Hu GY, Wu CP. (1996). Electrophysiological and morphological properties of pyramidal and nonpyramidal neurons in the cat motor cortex in vitro. *Neuroscience*, *73*(1), 39–55. https://doi.org/10.1016/0306-4522(96)00009-7

D'Adamo, M. C., Liantonio, A., Rolland, J. F., Pessia, M., & Imbrici, P. (2020). Kv1.1 Channelopathies: Pathophysiological Mechanisms and Therapeutic Approaches. *Int J Mol Sci*, *21*(8). https://doi.org/10.3390/ijms21082935

Defelipe, J. (2011). The evolution of the brain, the human nature of cortical circuits, and intellectual creativity. *Front Neuroanat*, *5*, 29. https://doi.org/10.3389/fnana.2011.00029

Dobin, A., Davis, C. A., Schlesinger, F., Drenkow, J., Zaleski, C., Jha, S., Batut, P., Chaisson, M., & Gingeras, T. R. (2013). STAR: ultrafast universal RNA-seq aligner. *Bioinformatics*, *29*(1), 15-21. https://doi.org/10.1093/bioinformatics/bts635

Eyal, G., Verhoog, M. B., Testa-Silva, G., Deitcher, Y., Lodder, J. C., Benavides-Piccione, R., Morales, J., DeFelipe, J., de Kock, C. P., Mansvelder, H. D., & Segev, I. (2016). Unique membrane properties and enhanced signal processing in human neocortical neurons. *Elife*, *5*. https://doi.org/10.7554/eLife.16553

Galakhova, A. A., Hunt, S., Wilbers, R., Heyer, D. B., de Kock, C. P. J., Mansvelder, H. D., & Goriounova, N. A. (2022). Evolution of cortical neurons supporting human cognition. *Trends Cogn Sci*, *26*(11), 909-922. https://doi.org/10.1016/j.tics.2022.08.012

Ghosh, L., & Jessberger, S. (2013). Supersize me-new insights into cortical expansion and gyration of the mammalian brain. *EMBO J*, *32*(13), 1793-1795. https://doi.org/10.1038/emboj.2013.128

Goethals, S., & Brette, R. (2020). Theoretical relation between axon initial segment geometry and excitability. *Elife*, *9*. https://doi.org/10.7554/eLife.53432

Goldberg, E. M., Clark, B. D., Zagha, E., Nahmani, M., Erisir, A., & Rudy, B. (2008). K+ channels at the axon initial segment dampen near-threshold excitability of neocortical fast-spiking GABAergic interneurons. *Neuron*, *58*(3), 387-400. https://doi.org/10.1016/j.neuron.2008.03.003

Goldberg, E. M., Jeong, H. Y., Kruglikov, I., Tremblay, R., Lazarenko, R. M., & Rudy, B. (2011). Rapid developmental maturation of neocortical FS cell intrinsic excitability. *Cereb Cortex*, *21*(3), 666-682. https://doi.org/10.1093/cercor/bhq138

Gu, C., & Barry, J. (2011). Function and mechanism of axonal targeting of voltage-sensitive potassium channels. *Prog Neurobiol*, *94*(2), 115-132. https://doi.org/10.1016/j.pneurobio.2011.04.009

Guet-McCreight, A., Chameh, H. M., Mahallati, S., Wishart, M., Tripathy, S. J., Valiante, T. A., & Hay, E. (2023). Age-dependent increased sag amplitude in human pyramidal neurons dampens baseline cortical activity. *Cereb Cortex*, *33*(8), 4360-4373. https://doi.org/10.1093/cercor/bhac348

Hammack, S. E., Mania, I., & Rainnie, D. G. (2007). Differential expression of intrinsic membrane currents in defined cell types of the anterolateral bed nucleus of the stria terminalis. *J Neurophysiol*, *98*(2), 638-656. https://doi.org/10.1152/jn.00382.2007

Hazra, R., Guo, J. D., Ryan, S. J., Jasnow, A. M., Dabrowska, J., & Rainnie, D. G. (2011). A transcriptomic analysis of type I-III neurons in the bed nucleus of the stria terminalis. *Mol Cell Neurosci*, *46*(4), 699-709. https://doi.org/10.1016/j.mcn.2011.01.011

Hennig, B. P., Velten, L., Racke, I., Tu, C. S., Thoms, M., Rybin, V., Besir, H., Remans, K., & Steinmetz, L. M. (2018). Large-Scale Low-Cost NGS Library Preparation Using a Robust Tn5 Purification and Tagmentation Protocol. *G3 Genes|Genomes|Genetics*, *8*(1), 79-89. https://doi.org/10.1534/g3.117.300257

Hernath, F., Schlett, K., & Szucs, A. (2019). Alternative classifications of neurons based on physiological properties and synaptic responses, a computational study. *Sci Rep*, *9*(1), 13096. https://doi.org/10.1038/s41598-019-49197-8

Hibino, H., Inanobe, A., Furutani, K., Murakami, S., Findlay, I., & Kurachi, Y. (2010). Inwardly rectifying potassium channels: their structure, function, and physiological roles. *Physiol Rev*, *90*(1), 291-366. https://doi.org/10.1152/physrev.00021.2009

Higgs, M. H., & Spain, W. J. (2011). Kv1 channels control spike threshold dynamics and spike timing in cortical pyramidal neurones. *J Physiol*, *589*(Pt 21), 5125-5142. https://doi.org/10.1113/jphysiol.2011.216721

Hodge, R. D., Bakken, T. E., Miller, J. A., Smith, K. A., Barkan, E. R., Graybuck, L. T., Close, J. L., Long, B., Johansen, N., Penn, O., Yao, Z., Eggermont, J., Hollt, T., Levi, B. P., Shehata, S. I., Aevermann, B., Beller, A., Bertagnolli, D., Brouner, K., . . . Lein, E. S. (2019). Conserved cell types with divergent features in human versus mouse cortex. *Nature*, *573*(7772), 61-68. https://doi.org/10.1038/s41586-019-1506-7

Hu, H., Gan, J., & Jonas, P. (2014). Interneurons. Fast-spiking, parvalbumin(+) GABAergic interneurons: from cellular design to microcircuit function. *Science*, *345*(6196), 1255263. https://doi.org/10.1126/science.1255263

Hu, X., Rocco, B. R., Fee, C., & Sibille, E. (2019). Cell Type-Specific Gene Expression of Alpha 5 Subunit-Containing Gamma-Aminobutyric Acid Subtype A Receptors in Human and Mouse Frontal Cortex. *Mol Neuropsychiatry*, *4*(4), 204-215. https://doi.org/10.1159/000495840

Innocenti, G. M., & Price, D. J. (2005). Exuberance in the development of cortical networks. *Nat Rev Neurosci*, *6*(12), 955-965. https://doi.org/10.1038/nrn1790

Jiang, M., Zhu, J., Liu, Y., Yang, M., Tian, C., Jiang, S., Wang, Y., Guo, H., Wang, K., & Shu, Y. (2012). Enhancement of asynchronous release from fast-spiking interneuron in human and rat epileptic neocortex. *PLoS Biol*, *10*(5), e1001324. https://doi.org/10.1371/journal.pbio.1001324

Jing Du, L. Z., Michael Weiser, Bernardo Rudy, chris J. McBain (1996). Developmentel Expression and Functional Characterization of the Potassium-Channel Subunit Kv3.1b in Parvalbumin-Containing Interneurons of the Rat Hippocampus *16*(2), 506–518. https://doi.org/10.1523/JNEUROSCI.16-

02-00506.1996

Jones, S. L., & Svitkina, T. M. (2016). Axon Initial Segment Cytoskeleton: Architecture, Development, and Role in Neuron Polarity. *Neural Plast*, *2016*, 6808293. https://doi.org/10.1155/2016/6808293

Kaas, J. H. (2013). The evolution of brains from early mammals to humans. *Wiley Interdiscip Rev Cogn Sci*, *4*(1), 33-45. https://doi.org/10.1002/wcs.1206

Kaas, J. H., Gharbawie, O. A., & Stepniewska, I. (2013). Cortical networks for ethologically relevant behaviors in primates. *Am J Primatol*, *75*(5), 407-414. https://doi.org/10.1002/ajp.22065

Kalmbach, B. E., Buchin, A., Long, B., Close, J., Nandi, A., Miller, J. A., Bakken, T. E., Hodge, R. D., Chong, P., de Frates, R., Dai, K., Maltzer, Z., Nicovich, P. R., Keene, C. D., Silbergeld, D. L., Gwinn, R. P., Cobbs, C., Ko, A. L., Ojemann, J. G., . . . Ting, J. T. (2018). h-Channels Contribute to Divergent Intrinsic Membrane

Properties of Supragranular Pyramidal Neurons in Human versus Mouse Cerebral Cortex. *Neuron*, *100*(5), 1194-1208 e1195. https://doi.org/10.1016/j.neuron.2018.10.012

Kole, M. H., Letzkus, J. J., & Stuart, G. J. (2007). Axon initial segment Kv1 channels control axonal action potential waveform and synaptic efficacy. *Neuron*, *55*(4), 633-647. https://doi.org/10.1016/j.neuron.2007.07.031

Kole, M. H., & Stuart, G. J. (2012). Signal processing in the axon initial segment. *Neuron*, *73*(2), 235-247. https://doi.org/10.1016/j.neuron.2012.01.007

Krienen, F. M., Goldman, M., Zhang, Q., R, C. H. D. R., Florio, M., Machold, R., Saunders, A., Levandowski, K., Zaniewski, H., Schuman, B., Wu, C., Lutservitz, A., Mullally, C. D., Reed, N., Bien, E., Bortolin, L., Fernandez-Otero, M., Lin, J. D., Wysoker, A., . . . McCarroll, S. A. (2020). Innovations present in the primate interneuron repertoire. *Nature*, *586*(7828), 262-269. https://doi.org/10.1038/s41586-020-2781-z

Kuba, H., & Ohmori, H. (2009). Roles of axonal sodium channels in precise auditory time coding at nucleus magnocellularis of the chick. *J Physiol*, *587*(1), 87-100. https://doi.org/10.1113/jphysiol.2008.162651

Leterrier, C. (2018). The Axon Initial Segment: An Updated Viewpoint. *J Neurosci*, *38*(9), 2135-2145. https://doi.org/10.1523/JNEUROSCI.1922-17.2018

Lewitus, E., Kelava, I., & Huttner, W. B. (2013). Conical expansion of the outer subventricular zone and the role of neocortical folding in evolution and development. *Front Hum Neurosci*, *7*, 424. https://doi.org/10.3389/fnhum.2013.00424

Li, T., Tian, C., Scalmani, P., Frassoni, C., Mantegazza, M., Wang, Y., Yang, M., Wu, S., & Shu, Y. (2014). Action potential initiation in neocortical inhibitory interneurons. *PLoS Biol*, *12*(9), e1001944. https://doi.org/10.1371/journal.pbio.1001944

Lorincz, A., & Nusser, Z. (2008). Cell-type-dependent molecular composition of the axon initial segment. *J Neurosci*, *28*(53), 14329-14340. https://doi.org/10.1523/JNEUROSCI.4833-08.2008

Lourenco, J., & Bacci, A. (2017). Human-Specific Cortical Synaptic Connections and Their Plasticity: Is That What Makes Us Human? *PLoS Biol*, *15*(1), e2001378. https://doi.org/10.1371/journal.pbio.2001378

M. C. Inda, J. DeFelipe, & Muñoz, A. (2006). Voltage-gated ion channels in the axon initial

segment of human cortical pyramidal cells and

their relationship with chandelier cells. *PNAS*, *103*, 2920-2925.

M. Martina, J. H. S., H. Ehmke, H. Monyer, P. Jonas. (1998). Functional and molecular differences between voltage-gated K+ channels of fast-spiking interneurons and pyramidal neurons of rat hippocampus. *J Neurosci*, *18*, 8111-8125.

M. Shao, W. Z., Y. Li, L. Tang, Z. Z. Hao, S. Liu. (2023). Patch-seq: Advances and Biological Applications. *Cell Mol Neurobiol*, *44*, 8.

Markram, H., Toledo-Rodriguez, M., Wang, Y., Gupta, A., Silberberg, G., & Wu, C. (2004). Interneurons of the neocortical inhibitory system. *Nat Rev Neurosci*, *5*(10), 793-807. https://doi.org/10.1038/nrn1519

Miller, I. F., Barton, R. A., & Nunn, C. L. (2019). Quantitative uniqueness of human brain evolution revealed through phylogenetic comparative analysis. *Elife*, *8*. https://doi.org/10.7554/eLife.41250

Molnar, G., Olah, S., Komlosi, G., Fule, M., Szabadics, J., Varga, C., Barzo, P., & Tamas, G. (2008). Complex events initiated by individual spikes in the human cerebral cortex. *PLoS Biol*, *6*(9), e222. https://doi.org/10.1371/journal.pbio.0060222

Molnar, G., Rozsa, M., Baka, J., Holderith, N., Barzo, P., Nusser, Z., & Tamas, G. (2016). Human pyramidal to interneuron synapses are mediated by multi-vesicular release and multiple docked vesicles. *Elife*, *5*. https://doi.org/10.7554/eLife.18167

Nusser, Z. (2009). Variability in the subcellular distribution of ion channels increases neuronal diversity. *Trends Neurosci*, *32*(5), 267-274. https://doi.org/10.1016/j.tins.2009.01.003

O'Brien, J. E., & Meisler, M. H. (2013). Sodium channel SCN8A (Nav1.6): properties and de novo mutations in epileptic encephalopathy and intellectual disability. *Front Genet*, *4*, 213. https://doi.org/10.3389/fgene.2013.00213

Ogawa, Y., Horresh, I., Trimmer, J. S., Bredt, D. S., Peles, E., & Rasband, M. N. (2008). Postsynaptic density-93 clusters Kv1 channels at axon initial segments independently of Caspr2. *J Neurosci*, *28*(22), 5731-5739. https://doi.org/10.1523/JNEUROSCI.4431-07.2008

Ollion, J., Cochennec, J., Loll, F., Escude, C., & Boudier, T. (2013). TANGO: a generic tool for high-throughput 3D image analysis for studying nuclear organization. *Bioinformatics*, *29*(14), 1840-1841. https://doi.org/10.1093/bioinformatics/btt276

Onodera, W., Asahi, T., & Sawamura, N. (2021). Rapid evolution of mammalian APLP1 as a synaptic adhesion molecule. *Sci Rep*, *11*(1), 11305. https://doi.org/10.1038/s41598-021-90737-y

Picelli, S., Faridani, O. R., Bjorklund, A. K., Winberg, G., Sagasser, S., & Sandberg, R. (2014). Full-length RNA-seq from single cells using Smart-seq2. *Nat Protoc*, *9*(1), 171-181. https://doi.org/10.1038/nprot.2014.006

Platkiewicz, J., & Brette, R. (2010). A threshold equation for action potential initiation. *PLoS Comput Biol*, *6*(7), e1000850. https://doi.org/10.1371/journal.pcbi.1000850

Poorthuis, R. B., Muhammad, K., Wang, M., Verhoog, M. B., Junek, S., Wrana, A., Mansvelder, H. D., & Letzkus, J. J. (2018). Rapid Neuromodulation of Layer 1 Interneurons in Human Neocortex. *Cell Rep*, *23*(4), 951-958. https://doi.org/10.1016/j.celrep.2018.03.111

Povysheva, N. V., Zaitsev, A. V., Rotaru, D. C., Gonzalez-Burgos, G., Lewis, D. A., & Krimer, L. S. (2008). Parvalbumin-positive basket interneurons in monkey and rat prefrontal cortex. *J Neurophysiol*, *100*(4), 2348-2360. https://doi.org/10.1152/jn.90396.2008

Radonjic, N. V., Ayoub, A. E., Memi, F., Yu, X., Maroof, A., Jakovcevski, I., Anderson, S. A., Rakic, P., & Zecevic, N. (2014). Diversity of cortical interneurons in primates: the role of the dorsal proliferative niche. *Cell Rep*, *9*(6), 2139-2151. https://doi.org/10.1016/j.celrep.2014.11.026

Raju, C. S., Spatazza, J., Stanco, A., Larimer, P., Sorrells, S. F., Kelley, K. W., Nicholas, C. R., Paredes, M. F., Lui, J. H., Hasenstaub, A. R., Kriegstein, A. R., Alvarez-Buylla, A., Rubenstein, J. L., & Oldham, M. C. (2018). Secretagogin is Expressed by Developing Neocortical GABAergic Neurons in Humans but not Mice and Increases Neurite Arbor Size and Complexity. *Cereb Cortex*, *28*(6), 1946-1958. https://doi.org/10.1093/cercor/bhx101

Rakic, P. (2009). Evolution of the neocortex: a perspective from developmental biology. *Nat Rev Neurosci*, *10*(10), 724-735. https://doi.org/10.1038/nrn2719

Ratkai, A., Tarnok, K., Aouad, H. E., Micska, B., Schlett, K., & Szucs, A. (2021). Homeostatic plasticity and burst activity are mediated by hyperpolarization-activated cation currents and T-type calcium channels in neuronal cultures. *Sci Rep*, *11*(1), 3236. https://doi.org/10.1038/s41598-021-82775-3

René Wilbers, A. A. G., Stan L.W. Driessens, Tim S. Heistek, Verjinia D. Metodieva, Jim Hagemann, Djai B. Heyer, Eline J. Mertens, Suixin Deng,, Sander Idema, P. C. d. W. H., David P. Noske, Paul van Schie, Ivar Kommers,, Guoming Luan, T. L., Yousheng Shu, Christiaan P.J. de Kock, Huibert D. Mansvelder,, & Goriounova1, N. A. (2023). Structural and functional specializations of human fastspiking

neurons support fast cortical signaling. https://doi.org/10.1126/sciadv.adf0708

Rich, S., Moradi Chameh, H., Sekulic, V., Valiante, T. A., & Skinner, F. K. (2021). Modeling Reveals Human-Rodent Differences in H-Current Kinetics Influencing Resonance in Cortical Layer 5 Neurons. *Cereb Cortex*, *31*(2), 845-872. https://doi.org/10.1093/cercor/bhaa261

Robles-Rebollo, I., Cuartero, S., Canellas-Socias, A., Wells, S., Karimi, M. M., Mereu, E., Chivu, A. G., Heyn, H., Whilding, C., Dormann, D., Marguerat, S., Rioja, I., Prinjha, R. K., Stumpf, M. P. H., Fisher, A. G., & Merkenschlager, M. (2022). Cohesin couples transcriptional bursting probabilities of inducible enhancers and promoters. *Nat Commun*, *13*(1), 4342. https://doi.org/10.1038/s41467-022-31192-9

Rogers, J., Kochunov, P., Zilles, K., Shelledy, W., Lancaster, J., Thompson, P., Duggirala, R., Blangero, J., Fox, P. T., & Glahn, D. C. (2010). On the genetic architecture of cortical folding and brain volume in primates. *Neuroimage*, *53*(3), 1103-1108. https://doi.org/10.1016/j.neuroimage.2010.02.020

Roth, F. C., & Hu, H. (2020). An axon-specific expression of HCN channels catalyzes fast action potential signaling in GABAergic interneurons. *Nat Commun*, *11*(1), 2248. https://doi.org/10.1038/s41467-020-15791-y

Rudy, B., Fishell, G., Lee, S., & Hjerling-Leffler, J. (2011). Three groups of interneurons account for nearly 100% of neocortical GABAergic neurons. *Dev Neurobiol*, *71*(1), 45-61. https://doi.org/10.1002/dneu.20853

Shah, M. M. (2014). Cortical HCN channels: function, trafficking and plasticity. *J Physiol*, *592*(13), 2711-2719. https://doi.org/10.1113/jphysiol.2013.270058

Sun, W., Wagnon, J. L., Mahaffey, C. L., Briese, M., Ule, J., & Frankel, W. N. (2013). Aberrant sodium channel activity in the complex seizure disorder of Celf4 mutant mice. *J Physiol*, *591*(1), 241-255. https://doi.org/10.1113/jphysiol.2012.240168

Szabo, A., Schlett, K., & Szucs, A. (2021). Conventional measures of intrinsic excitability are poor estimators of neuronal activity under realistic synaptic inputs. *PLoS Comput Biol*, *17*(9), e1009378. https://doi.org/10.1371/journal.pcbi.1009378

Szegedi, V., Bakos, E., Furdan, S., Kovacs, B. H., Varga, D., Erdelyi, M., Barzo, P., Szucs, A., Tamas, G., & Lamsa, K. (2023). HCN channels at the cell soma ensure the rapid electrical reactivity of fast-spiking interneurons in human neocortex. *PLoS Biol*, *21*(2), e3002001. https://doi.org/10.1371/journal.pbio.3002001

Szegedi, V., Molnár, G., Paizs, M., Csakvari, E., Barzó, P., Tamás, G., & Lamsa, K. (2017). High-Precision Fast-Spiking Basket Cell Discharges during Complex Events in the Human Neocortex. *eneuro*, *4*(5). https://doi.org/10.1523/eneuro.0260-17.2017

Szegedi, V., Paizs, M., Baka, J., Barzo, P., Molnar, G., Tamas, G., & Lamsa, K. (2020). Robust perisomatic GABAergic self-innervation inhibits basket cells in the human and mouse supragranular neocortex. *Elife*, *9*. https://doi.org/10.7554/eLife.51691

Szegedi, V., Paizs, M., Csakvari, E., Molnar, G., Barzo, P., Tamas, G., & Lamsa, K. (2016). Plasticity in Single Axon Glutamatergic Connection to GABAergic Interneurons Regulates Complex Events in the Human Neocortex. *PLoS Biol*, *14*(11), e2000237. https://doi.org/10.1371/journal.pbio.2000237

Szegedi, V., Tiszlavicz, A., Furdan, S., Douida, A., Bakos, E., Barzo, P., Tamas, G., Szucs, A., & Lamsa, K. (2024). Aging-associated weakening of the action potential in fast-spiking interneurons in the human neocortex. *J Biotechnol*, *389*, 1-12. https://doi.org/10.1016/j.jbiotec.2024.04.020

Szucs, A., Ratkai, A., Schlett, K., & Huerta, R. (2017). Frequency-dependent regulation of intrinsic excitability by voltage-activated membrane conductances, computational modeling and dynamic clamp. *Eur J Neurosci*, *46*(9), 2429-2444. https://doi.org/10.1111/ejn.13708

T.F. Freund, G. B. (1996). Interneurons of the Hippocampus. *6*(4), 347–470. https://doi.org/10.1002/(SICI)1098-1063(1996)6:4<347::AID-HIPO1>3.0.CO;2-I

Tremblay, R., Lee, S., & Rudy, B. (2016). GABAergic Interneurons in the Neocortex: From Cellular Properties to Circuits. *Neuron*, *91*(2), 260-292. https://doi.org/10.1016/j.neuron.2016.06.033

Tukacs, V., Fladhus, E. K., Mittli, D., Lőrincz, M. L., Eberwine, J., Kékesi, K. A., & Juhász, G. (2024). Neuronal phenotype defined by transcriptome-wide bursting kinetics in pyramidal and

fast-spiking cells. https://doi.org/10.1101/2024.05.16.594495

Varga, V., Hangya, B., Kranitz, K., Ludanyi, A., Zemankovics, R., Katona, I., Shigemoto, R., Freund, T. F., & Borhegyi, Z. (2008). The presence of pacemaker HCN channels identifies theta rhythmic GABAergic neurons in the medial septum. *J Physiol*, *586*(16), 3893-3915. https://doi.org/10.1113/jphysiol.2008.155242

Wang, B., Ke, W., Guang, J., Chen, G., Yin, L., Deng, S., He, Q., Liu, Y., He, T., Zheng, R., Jiang, Y., Zhang, X., Li, T., Luan, G., Lu, H. D., Zhang, M., Zhang, X., & Shu, Y. (2016). Firing Frequency Maxima of Fast-Spiking Neurons in Human, Monkey, and Mouse Neocortex. *Front Cell Neurosci*, *10*, 239. https://doi.org/10.3389/fncel.2016.00239

Wang, S., Ding, P., Yuan, J., Wang, H., Zhang, X., Chen, D., Ma, D., Zhang, X., & Wang, F. (2022). Integrative cross-species analysis of GABAergic neuron cell types and their functions in Alzheimer's disease. *Sci Rep*, *12*(1), 19358. https://doi.org/10.1038/s41598-022-21496-7

Winckler, B., P. Forscher, and I. Mellman. (1999). A diffusion barrier maintains distribution of membrane proteins in polarized neurons. *Nature*, *397*, 698–701. https://doi.org/10.1038/17806

Yamada, R., & Kuba, H. (2016). Structural and Functional Plasticity at the Axon Initial Segment. *Front Cell Neurosci*, *10*, 250. https://doi.org/10.3389/fncel.2016.00250

Yang, S. S., Li, Y. C., Coley, A. A., Chamberlin, L. A., Yu, P., & Gao, W. J. (2018). Cell-Type Specific Development of the Hyperpolarization-Activated Current, Ih, in Prefrontal Cortical Neurons. *Front Synaptic Neurosci*, *10*, 7. https://doi.org/10.3389/fnsyn.2018.00007

Yang, Y., Ogawa, Y., Hedstrom, K. L., & Rasband, M. N. (2007). betaIV spectrin is recruited to axon initial segments and nodes of Ranvier by ankyrinG. *J Cell Biol*, *176*(4), 509-519. https://doi.org/10.1083/jcb.200610128